Faculty of Natural Science and Technology
Department of Physics

NTNU
Innovation and Creativity

MASTER'S THESIS FOR

STUD. TECHN.
ELISABETH LINDBO HANSEN

Thesis started:	01.21.2008
Thesis submitted:	07.04.2008

DISCIPLINE: PHYSICS

English title: *"Colloidal Dispersions of Clay Nanoplatelets" –Optical birefringence and x-ray scattering studies of nematic phases.*

This work has been carried out at NTNU, Norway and at PLS, South Korea, under the supervision of Professor Jon Otto Fossum.

Trondheim, 07.04.08

Jon Otto Fossum

Responsible supervisor

Professor at Department of Physics

For my dad and grandfathers, whose
respective fascinations for science
found their way to me.

Abstract

This master's thesis concerns aqueous dispersions of synthetic fluorohectorite clay nanoplatelets containing charge stabilizing intercalated cations of respectively sodium (Na^+), lithium (Li^+), iron (Fe^{3+}) and nickel (Ni^{2+}), and a corresponding chloride salt. The monovalently intercalated fluorohectorite dispersions develop birefringent textures when initially isotropic suspensions are allowed to settle under the action of gravity. Furthermore, the monovalently intercalated clay dispersions display volume swelling and gelling; these characteristic behaviors are not observed in the di- and trivalently intercalated clays, which are neither seen to phase separate. Partially evaporated and gravitationally phase separated Na-fluorohectorite dispersions held in 1 mm and 2 mm in diameter cylindrical glass capillaries are investigated optically between crossed polarizers and by small- and intermediate-angle x-ray scattering. It is shown that evaporating and partially settled Na-fluorohectorite dispersions develop a new kind of nematic order not previously observed, where extended regions show a uniaxial configuration of face-down platelets where the nematic order parameter S_2 attains values of between 0.77 and 0.91, that are considerably and consistently higher than those previously found for Na-fluorohectorite dispersions. The order parameter is obtained by fitting the azimuthal intensity profiles of an evaporated sample with a Maier-Saupe type distribution. Peaks in the small-angle scattering from partially evaporated Na-fluorohectorite dispersions are found to correspond with scattering between platelet faces. The magnetic Fréedericksz transition is investigated in an aged Na-fluorohectorite capillary sample through birefringence observations and x-ray scattering. Evidence is presented based on the Frank-Oseen equation and observed experimental features, arguing that the initially standing Na-fluorohectorite platelets undergo a splay-and-bend distortion and reorient in selected sample regions to the face-down configuration. Previous results concerning the stacking polydispersity of Na-fluorohectorite platelets are revisited, presenting data opening for a possibly larger variance in particle sizes.

Contents

Preface

The work presented in this thesis sums up a semester that has for me been perhaps the most rewarding in my studies so far. Having written my 9th semester project within the field of heavy ion collisions and nuclear science, I started out on my master in the beginning of January 2008 with alot to learn. My motivation for studying clay-water dispersions lay primarily in the fact that I hoped this work would give me valuable experience with x-ray scattering techniques, which are to me interesting in particular due to their many and diverse areas of application within the structural sciences. Unfortunately, the SAXS equipment of our NTNU lab remained inoperational until the start of April, causing me to focus my efforts more towards the colloidal dispersions themselves. This turn of events has however truly opened up a new field of science to me, of which I previously had little to no knowledge. It is my hope that this thesis can provide a brief overview of the factors that are known to be determining for the behavior of aqueous fluorohectorite dispersions, thus facilitating the subsequent interpretation of the experimental results. To this end, I have in places included some rough estimates to parameters such as the fluorohectorite platelets' surface potentials or the Hamaker constant, in order to approximately assess the importance of different contributing factors presented in the equations of the theory section. It is important to keep in mind that these estimates are rough and can only be thought to reflect on a very broad basis the qualitative behavior of the dispersions discussed.

The results I have obtained experimentally over the course of my master semester are presented in the results and discussion chapter. In particular, it was an exhilarating experience to discover in my Mark tube samples extended regions exhibiting true uniaxial nematic ordering. I also hope that some of the more qualitative results presented with regards to the very differing behaviors observed in fluorohectorite dispersions containing intercalated cations other than Na^+ might serve to shed some light on the complex and in my opinion not yet fully understood characteristics of smectite clays in general.

A long line of some very talented, helpful and creative people have been essential to the results presented in this thesis. My thanks therefore to Professor Jon Otto Fossum for providing a free, creative and international

research environment for all his students; to Bård Martin Kjelling for generously sharing with me his technical expertise with regards to everything from synchrotron sample holder designs to the more challenging art of eating with chopsticks; to Zbigniew Rozynek, also known as Zbyzsek, who gave me the idea of investigating aqueous dispersions of Fe-fluorohectorite; to Knut Magnus for sharing with me a few mathematical oddities as well as many good internet game moments; and to Henrik Hemmen for good discussions and also for the use of his extensive, if borrowed, library. I also owe great thanks to Henrik and to Yvés Méheust who modified their order parameter scripts to suit my needs perfectly.

My thanks go also to our excellent and in South Korea much missed technician Ole Tore Buset, to post docs. Bau-xiang Wang and Min Zhou as well as to the staff and students working with us at the Pohang Light Source in Pohang, South Korea, among whom Kim Chan, Yavuz Östürk, Cho Inhwa, Shasidhara Marathe and Professor Do Young Noh deserve special thanks. With the first two, Bård Martin Kjelling and I shared many long nights sprinkled with an assortment of Korean dishes and synchrotron related frustrations and joys alike. My thanks also to Eduardo Azevedo who worked with me into the late hours of the night during our SAXS based studies in Norway, as well as to Romulo Tenorio and Davi de Miranda Fonseca. I also wish to thank Nils-Ivar Ringdal whose long awaited master thesis and excellent optical birefringence setup has provided much of the background for the current work.

Chapter 1

Introduction

The current report concerns aqueous dispersions of colloidal clay nanoplatelets. The investigated clay mineral species are different cation-intercalated fluorohectorites. Clay-water dispersions of the montmorillonite/smectite family such as bentonite [38, 24], nontronite [49], and more recently also synthetic fluorohectorite [12, 20, 18] and laponite [39, 24], have been studied for several years due to their range of practically useful and scientifically interesting characteristics, that range from the water-intercalating properties of smectite clays, to the anisotropic liquid crystalline states observed in dispersions of clay particles due to their anisotropic shapes. Still, the nano-scale structures and physical processes responsible for several characterizing properties of clay dispersions are not well understood. The structural configuration of the ubiquitous clay gels for instance, has to this date not been determined, despite of fairly extensive studies [23]. The current report is mainly concerned with features observed in an ordered phase of the investigated clay-water dispersions known as the nematic; it's presence is confirmed and explored through optical birefringence observations and anisotropic x-ray scattering images.

The use of clay-water mixtures by human beings date back many hundreds of years due to the ability of high clay content mixes to be easily shaped by hand yet subsequently hardened into ceramics during heat treatment and drying. Clays are geologically abundant, and play important roles in large scale natural phenomena like landslides and in the sedimentary build-up of estuary deposits [78]. When clay-carrying waterways are subject to changing salinity conditions, the initially dispersed clay particles present in for instance riverwater, will undergo flocculation and sediment as they encounter the salty waters of the sea. This behavior points towards two important characteristics of clay minerals, namely their small size, which allows them to stay dispersed in water, and their sensitivity to changing electrolyte conditions. Both features are determining for the behavior of colloidal clay dispersions. Landslides containing fine-sized particles like clays or silts are

generally termed earthflows, and the occurrence of such earthflows is caused by another important characteristic of certain clay minerals, namely their swelling capacity. A typical clay particle consists of atomic-scale unit layers carrying net negative surface charges, that are stacked through the sharing of intercalated positive ions. Due to their polar nature, water molecules can enter the interlayer space, leading to crystalline swelling of the clay stacks. Soils high in swelling clay content thus undergo volume changes in response to dry or wet weather, giving rise to common instabilities in clay-rich soils.

A fourth characterizing parameter of clays are their large surface-to-volume ratios, that allow for extensive adsorption of various chemical or ionic species. Within the context of physical colloidal science however, the perhaps most important characteristic of several clay minerals are their plate-like morphology, that opens for the possibility of colloidal clay dispersions undergoing phase transitions to ordered states in response to increases in the clay concentration. In 1938, Langmuir published a later much quoted paper [38], reporting observations of isotropic-nematic transitions in aqueous dispersions of bentonite clay – Langmuir himself did however note that he could not reproduce this clear phase separation due to gelling of the clay-water dispersions. More recently, the presence of nematic or nematic-like ordering in several clay systems have been reported [12, 39, 49, 24], co-existing with the gelled phase.

A large portion of the colloidal clay samples investigated in this project display interesting phase behaviors. When newly prepared Na-fluorohectorite dispersions are left to sediment in the earth's gravitational field, several strata of phases develop over the course of days, weeks and months. These phases are visible to the naked eye and some of them strongly birefringent when viewed between crossed polarizers. The characteristic optical behavior of these samples indicate their liquid crystalline character. Because liquid crystals have found widespread use in optical display technology and in other areas were controlled variability of optical properties is desirable, the liquid crystalline phase behavior of colloidal clay samples is an interesting research topic. Yet liquid crystals have properties that go beyond their optical birefringence. The science of self-organized structures is today a hot research topic promoted by the emerging field of nanoscience, and within this context, clays feature as environmentally friendly and inexpensive nanomaterials that are naturally abundant and widely available.

Chapter 2

Theory

2.1 Clay nanoplatelets

As already introduced in the previous chapter, clays[1] are layered minerals that exist either as stacked structures forming lamellar particles, or as single layers exfoliated in a solvent. The single unit clay layers are of either 1:1 or 2:1 type, consisting of respectively two or three structural sheets bound through the sharing of oxygen atoms [78]. There are two kinds of such sheets, called respectively tetrahedral or octahedral. The tetrahedral sheets are generally made of silicon (Si^{4+}) and aluminum (Al^{3+}) tetrahedrally coordinated by oxygen (O^{2-}), whereas the octahedral sheets typically consists of aluminum (Al^{3+}), lithium (Li^{+}), magnesium (Mg^{2+}) or iron (Fe^{3+}/Fe^{2+}) coordinated by oxygens (two in 1:1 and four in 2:1 clays) and hydroxyl groups (OH^{-}, four in 1:1 and two in 2:1 clays) [47], or in synthetic clays also by fluorine (F^{-}). 1:1 clays are made up of unit layers where one tetrahedral sheet is bound with its apical oxygens facing an octahedral sheet, whereas 2:1 clays are made up of an octahedral sheet sandwiched between two tetrahedral sheets whose apical oxygens point towards the sandwiched sheet [9].

A single unit clay layer consists of several atomic planes that, in contrast to the layers themselves, are strongly bound and do not separate. 1:1 clays have five ionic planes made up of respectively 1) the basal oxygens of the silicate sheet, 2) the tetrahedrally coordinated cations, 3) the apical oxygens of the silicate sheet, corresponding with one of the planes of oxygen and hydroxyl groups of the octahedral sheet, 4) the cations of the octahedral sheet and 5) the second plane of oxygens and hydroxyl groups of the octahedral sheet [47]. 2:1 clays have seven ionic planes. The first four, equal to the four

[1] The nineteenth century definition of clays was based on the at-the-time optical microscopy resolution limit, defining clays as consisting of grains less than 2 μm in diameter, with less regard to the then unknown chemical composition of the particles [77]. For a review of current opinions on what constitutes clays, clay minerals and clay rocks, see [3].

first ionic planes of a 1:1 clay, are followed by 5) the second plane of oxygens and hydroxyl groups of the octahedral sheet, corresponding with the plane of the apical oxygens of the second silicate sheet, 6) the tetrahedrally coordinated cations of the second silicate sheet and 7) the basal oxygens of the second silicate sheet [47]. Due to this regular structure, both along the stacking direction for a lamellar clay particle, and more noticeably within a single layer, clays are considered as partially crystalline and thus can be characterized by a unit cell. The unit cell of 1:1 clays contains four tetrahedral and six octahedral cation sites, whereas eight tetrahedral and again six octahedral cation sites are contained in the unit cell of a 2:1 clay [3].

Clays can be either dioctahedral or trioctahedral, depending respectively on whether only four or all six of the octahedral unit cell sites are occupied. The 2:1 octahedral sheets contain both cis- and trans-octahedra, where the cis-octahedra have their two hydroxyl groups on side linked corners whereas trans-octahedra have them on diagonally linked corners [3]. The free octahedral sheet side of a 1:1 unit layer has only hydroxyl groups. Substitution of tetravalent silicon with trivalent aluminum in the tetrahedral sheet or substitutions of tri- or divalent cations with di- or monovalent cations in the octahedral sheet cause a net negative unit layer charge for certain 2:1 clays. This negative charge is compensated for by cations intercalated between the unit layers of stacked 2:1 structures. In the dry state of a trioctahedral 2:1 clay, the interlayer cations are found situated in the hexagonal cavities of the silicate sheets that are also the locations of the non-bonded hydroxyl groups of the octahedral sheet. Individual clay layers of both the 1:1 or the 2:1 type can stack together to form lamellar clay particles, which may again form aggregated structures. The layer thickness of a 1:1 clay is typically around 0.7 nm [78], whereas for the 2:1 clays the periodicity along the stacking direction for a lamellar clay particle may be highly affected by intercalated species, and can vary from around 0.91 nm to more than 1.5 nm [3].

There are several classes of clays. A common 1:1 type dioctahedral clay is kaolinite. Kaolinite unit layers exist as roughly hexagonal platelets, and these can stack because hydrogen bonds form between the hydroxyl groups of the octahedral sheet belonging to one unit layer and the oxygens of a silicate sheet belonging to another unit layer [3]. Kaolinite is amongst other things used in porcelain and is added to magazine paper to make it glossy. Halloysite is a hydrated polymorph of kaolinite, meaning that it has the same chemical composition as the latter, but the individual halloysite clay particles are usually tubules [3] with an average diameter of 30 nm and lengths between 0.5 and 10 μm. Water intercalates between the unit layers of halloysite, in part causing the tubule structure, but only to a very moderate degree, or not at all, in between kaolinite layers.

A common and important class of clay minerals are the montmorillonite/smectites. These 2:1 clays are composed of an octahedral sheet sand-

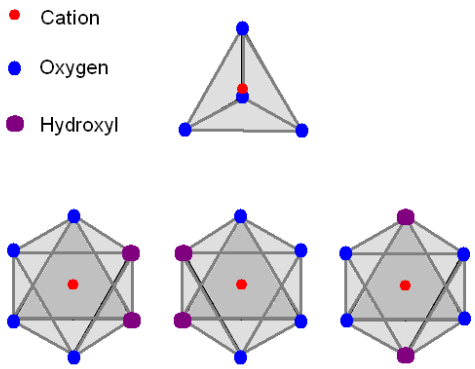

Figure 2.1: Typical clay coordination of oxygen and hydroxyl groups around central cations. The figure shows one tetrahedron (top) and three octahedra (bottom). The octahedra are of respectively cis-, cis- and trans-type (left to right).

wiched between two tetrahedral silicate sheets and because the montmorillonite/smectite unit layers carry a slight to moderate negative surface charge at the layer faces due to ionic substitutions or vacancies, these unit layers stack to form lamellar particles by sharing cations. Water and other polar molecules easily intercalate between the unit layers and cause the montmorillonite/smectites to display crystalline swelling [3]. Common applications of the montmorillonite/smectites span the area between drilling muds and cosmetic powders, and in 2003 an article in Science [29] presented data showing that montmorillonite could accelerate the spontaneous conversion of lipid micelles into vesicles[2]. Some clay particles would become trapped inside these vesicles and if the clay particles, known to catalyze the polymerization of RNA from activated ribonucleotides, carried RNA on their surfaces, these RNA strands would also become trapped inside the vesicles. These results were found to indicate that montmorillonite or other minerals with negative surface charges might have been crucial in the early stages of development of life on earth.

[2]Micelles and vesicles are formed by amphiphilic molecules consisting of polar, water-loving head groups and non-polar, water-hating fatty acid tails. When dispersions of amphiphilic molecules in water reach a certain concentration level, micelles can form. A micelle is typically a spherical aggregate of amphiphilic molecules with the water-loving head groups facing outwards, shielding the non-polar tails in the center of the micelle. Vesicles can be envisioned as double-layered micelles or shells where the water-loving head groups are on the inner as well as the outer shell surfaces. This double-layered organization of amphiphilic lipids is known as a lipid bilayer. Cell walls and the walls of entities inside cells are lipid bilayers, and hence vesicle formation and behavior are crucial investigation topics concerning the origin of life on earth.

2.1.1 Fluorohectorite

The clay investigated in the current report is a synthetically produced trioctahedral clay known as fluorohectorite, that has a half unit cell formula $X_{0.6/v}(Mg_{2.4}Li_{0.6})Si_4O_{10}F_2$ [17] and belongs to the montmorillonite/smectite group. The chemical formula informs that an average of 1.2 Mg^{2+} cations per unit cell in the octahedral sheet have been replaced by monovalent Li^+, leading to a positive charge deficiency of 1.2 unit charges per unit cell, that is compensated for by the interlayer cation species X^v. Here v is a positive real number representing the valency of the interlayer cation. The half unit cell formula also demonstrates that in fluorohectorite the usual hydroxyl groups of natural hectorites have been replaced by fluorine, making this clay somewhat heavier relative to natural hectorites.

Natural hectorites have a positive charge deficiency of 0.23 charges per unit cell, leading to a surface charge density of -0.076 C/m^2 [3]. Assuming synthetic fluorohectorite has a unit cell with surface dimensions comparable to those of natural hectorite, this would by comparison yield a fluorohectorite surface charge density of approximately -0.40 C/m^2. Slade [64] references [28] on the unit cell surface area of the exposed basal oxygen planes of smectites, citing a value of 48.5 Å^2. Dividing the fluorohectorite unit cell charge of $1.2e^-$ by this area again yields a surface charge density of -0.40 C/m^2 for fluorohectorite. In comparison, the surface charge density of montmorillonite and vermiculite with respectively $0.4e^-$ and $0.8e^-$ per unit cell is -0.14 C/m^2 and -0.26 C/m^2 [3]. The high surface charge density of fluorohectorite is caused by the extensive substitutions of Mg^{2+} with Li^+ in the octahedral sheet. In comparison with for example synthetic laponite, which has a surface charge density of $0.4e^-$ per unit cell and is known to exfoliate into single unit layers in aqueous suspensions, fluorohectorite has been reported from x-ray data to retain a stacked structure of lamellar particles composed of between 20 and 100 unit layers when dispersed in water [12]. Fluorohectorite, like other smectite clays, has the ability to intercalate a variable amount of water between the unit layers of the stacked structure, and for Na-fluorohectorite three stable hydration states with respectively zero, one or two intercalated water layers have been identified with repetition distances in the stacking direction of respectively 1.0 nm, 1.2 nm and 1.5 nm [9]. Because of the water content, the density of a smectite clay changes with the hydration state. Table 2.1 list the mass density of fluorohectorite as a function of intercalated water content.

Fluorohectorites in water suspensions

Aqueous suspensions of Na-intercalated fluorohectorites have been found to undergo transitions to orientationally anisotropic, or so-called liquid crystalline states upon setteling in the earth's gravitational field [12, 20]. The

Table 2.1: Mass densities ρ_m of Na-fluorohectorites with variable amounts of intercalated water. Data retrieved from [37]. The mass density of pure water is also included for reference.

Particle	ρ [g/cm^3]
H_2O	1.0
NaFht	2.80
NaFht $\times$ 1 wl H_2O	2.31
NaFht $\times$ 2 wl H_2O	2.02

formation of ordered phases in dispersions of anisotropic particles was theoretically explained by Onsager in the 1940s for hard, i.e. short range repulsive rods [55]. Onsager showed how the gain in translational entropy upon going from the isotropic to the nematic state outweighs the simultaneous loss of orientational entropy, thus making the transition thermodynamically favorable. More recent computer simulations have demonstrated the same phenomenon in suspensions of disc-like particles, where the platelets are however often modeled as thin or infinitely thin cylinders interacting through hard-core potentials [76, 15]. However, in clay dispersions observations of the isotropic-nematic Onsager transition frequently is hindered by gelation [75]. Synchrotron x-ray experiments [20] as well as optical investigations [59] have demonstrated the presence of anisotropic regions permeating both the presumed gel and sol regimes of gravitationally settled Na-fluorohectorite dispersions[3]. Recent magnetic resonance imaging (MRI) studies [10], also combined with synchrotron investigations [18, 31, 30], show that Na-fluorohectorite platelets adopt three main orientations in the anisotropic regions. Close to polar glass walls the platelets have been observed to align with their face normals perpendicular to the wall [10], i.e. in homeotropic anchoring. Homeotropic-like anchoring has also newly been observed at the interface between isotropic and ordered phases [31], where the clay platelets are seen to lie with their face normals perpendicular to the interface plane. In the main anisotropic region however, commonly referred to as the nematic phase but also designated as anti-nematic[4], the Na-

[3]The definition of a gelled phase in this context is a qualitative one, referring to the higher viscosity parts of an aqueous clay dispersion. The structure of clay gels has not yet been positively identified and, as briefly discussed in [18], regions of higher viscosity in aqueous clay dispersions may also be designated as glassy phases.

[4]It can be argued that the standing anisotropic phase of Na-fluorohectorite dispersions is not a conventional nematic, as the commonly adopted orientation of greatest order is perpendicular to the clay platelet faces. Some authors, notably Méheust et al. [48], have opted to address this phase as anti-nematic. In the current work, the conventional nematic

fluorohectorite platelets display a commonly preferred direction of greatest order that is perpendicular to the face normals and parallel with the gravitational force. Thus the particles in this oriented phase are effectively standing up. Results from MRI investigations [10] have indicated that the projections of the face normals in this standing phase onto the horizontal plane are randomly distributed on macroscopic scales ($\approx$ mm), except for close to polar container walls were homeotropic anchoring prevails even in strong magnetic fields [10] of around 2 T. The distributing effects of the walls are thought to be more determining in smaller sample containers [18], so that in such cases the randomness of the face normals in the standing nematic is lost[5]. When a magnetic field of 2 T was applied to the approximately 1 cm diameter tubes in the MRI experiment [10], the Na-fluorohectorite particles far enough from the walls were seen to align parallel with the field, resulting in an ordered state more correctly resembling that of a conventional nematic.

2.2 Colloidal dispersions

Suspensions of finely dispersed but insoluble particles in a solvent are called colloidal when the dispersed particles have at least one spatial dimension in the 1 nm to 1 μm range. Colloidal dispersions are abundant and make up natural substances such as milk or fog, and man-made systems like paints or ferrofluids. Clay particles in salt water form colloidal dispersions where the role of the ionic species is to shield the Coulombic repulsion between the negatively charges clay particles. The phase behavior of colloidal dispersions can be rich and is dependent on the shape of the dispersed particles. In particular, as discussed in the case of fluorohectorites in section 2.1.1, colloidal dispersions of anisotropic particles can form lyotropic liquid crystalline phases. A colloidal lyotropic liquid crystal is a dispersion whose phase behavior depends on the concentration of the colloidal species. The phases discussed in this context are defined by the presence within the dispersions of orientational and possible also translational order. Lyotropic liquid crystalline phase transitions in colloidal systems are promoted by changes in the concentration of the colloidal species. Such concentration changes are produced during evaporation of the solvent [24, 49] or when gravity or centrifugal forces induce a concentration gradient in the colloidal samples, often

designation is reserved for oriented domains where the average direction of the platelet normals coincide with the commonly preferred direction of greatest order, so that in the limiting case of perfect order, rotation about the director axis does not change the platelet orientation (assuming a disc-like morphology). The term standing nematic will be used for the commonly observed orientationally anisotropic phase seen in the Na-fluorohectorite dispersions, which by Méheust et al. is referred to as the anti-nematic.

[5]Some ambiguity seems to exist in the literature with regards to the orientation of the platelets' face normals in the standing nematic. Notably, Fonseca et al. [18] present a picture where the standing nematic is a conventional, homeotropically anchored nematic whose variations in the director are directly caused by the curvature of the capillary walls.

without evaporation occurring [74, 73, 12]. When phase changes are promoted by gravity, a single sample container can contain several strata of coexisting phases [17, 73]. The following section will take a closer look at the effects which gravity exerts on polydisperse colloidal suspensions.

2.2.1 Gravitational sedimentation in polydisperse suspensions

In order for gravity to affect a colloidal dispersion, causing sedimentation, the mass density of the colloidal species must exceed the mass density of the solvent. The forces due to buoyancy and gravity acting on an object of mass density $\rho_{m,o}$ and volume V_o submerged in an incompressible fluid of mass density $\rho_{m,s}$ at standard gravity g is given by:

$$F_b + F_g = g\rho_{m,s}V_o - g\rho_{m,o}V_o = gV_o\left(\rho_{m,s} - \rho_{m,o}\right) \tag{2.1}$$

Here the positive direction is defined to be upwards, i.e. in the direction opposite to the gravitational force. For a 80 nm thick clay-like disc with a diameter of 1 µm and a mass density of 2.02 g/cm^3 submerged in water with a mass density of 0.998 g/cm^3 at 20 °C, this force will be approximately −0.63 pN, meaning the particle will sink. However, a particle moving through a fluid will also experience a drag. This drag can be expressed through the Stokes friction force as $F_f = 6\pi\eta v R$ [69], where η is the dynamic viscosity coefficient of the solvent, v the particle velocity and R the Stokes equivalent spherical radius of the particle. When the net force $F = F_b + F_g + F_f$ due to buoyancy, gravity and drag equals zero, the sinking colloidal particle will reach a terminal velocity v_t which can be expressed as:

$$v_t = \frac{gV_o\left(\rho_{m,o} - \rho_{m,s}\right)}{6\pi\eta R} \tag{2.2}$$

The equivalent expression for a disc of radius R and height d setteling broadside on is given in [53] as:

$$v_t = \frac{g\pi Rd\left(\rho_{m,o} - \rho_{m,s}\right)}{12\eta} \tag{2.3}$$

According to this expression, valid when the ratio $d/R \ll 1$, the terminal velocity for the 80 nm thick disc described above would be of around 105 nm/s in water with a viscosity of $\eta = 1.002 \cdot 10^{-3}$ Ns/m^2 at 20 °C, equivalent to about 0.377 mm/h. It would thus take about 265 h for the particle to settle within a distance of 10 cm in water at standard gravity. This does however require a dilute suspension, so that inter-particle interactions are negligible compared with the effects of buoyancy, gravity and Stokes drag. Whalley and Mullins [81] present an expression for the terminal velocity of a clay particle modelled as an oblate ellipsoid of thickness d and radius R, deduced

from Galily and Cohen's treatise on aerosol particles [25];

$$v_t = \frac{\pi g R d \left(\rho_{m,o} - \rho_{m,s}\right)}{96\eta} \left(5 - \cos\left[2\theta\right]\right) \tag{2.4}$$

Here θ is the angle between the short ellipsoid axis and the direction of the gravitational force. For an ellipsoid with a thickness $d = 80$ nm and a radius $R = 0.5$ µm falling with its short axis parallel with the gravitational field, this expression yields a terminal velocity v_t of approximately 52 nm/s, whereas when the same ellipsoid falls with its short axis perpendicular to the gravitational field, v_t takes a value of approximately 79 nm/s. Because the terminal velocity is proportional to the gravitational acceleration g, sedimentation velocities can be dramatically increased if the colloidal dispersions are placed in a centrifuge. Polydisperse colloidal gibbsite suspensions centrifuged at $900g$ for approximately 24 h have been found to undergo phase transitions to a hexagonal columnar phase at the bottom of the containers[71], a phase which at standard gravity only developed on timescales of a year or more. The high centrifugal acceleration was found to cause size fractionation with the larger gibbsite platelets forming the bottom parts of the columnar structure. It is however important to note that when colloidal samples are size fractionated in a centrifuge as opposed to in the gravitational field, the acceleration is no longer uniform over the sample height [70].

A further point can be made based on the setteling velocity expression of Equation 2.4. Whalley and Mullins [81], starting out from the hypothesis that the maximum kinetic energy E_o available for orientation is given by the difference in kinetic energy between setteling perpendicular to or parallel with the short ellipsoid axis of the modelled clay, finds the following expression for E_o:

$$E_o = \frac{40\pi R^2 d \rho_{m,o}}{3} \left[\frac{\pi g R d \left(\rho_{m,o} - \rho_{m,s}\right)}{96\eta}\right]^2 \tag{2.5}$$

Further equating this with an energy term of $k_B T/2$ attributable to the orientational degree of freedom, according to Marshall [44] yields a transition point that in the present discussion is given by:

$$\frac{R^4 d^3 \rho_{m,o} \left(\rho_{m,o} - \rho_{m,s}\right)^2}{T} = 1.606 \cdot 10^{-30} \tag{2.6}$$

Random sedimentation is expected when the left side of Equation 2.6 is smaller than the right side. In the opposite case one expects oriented sedimentation, with the ellipsoids' short axis oriented parallel with the gravitational field. Again using the illustrative example of a 80 nm thick platelet with a diameter of 1 µm, sedimenting in water at a temperature of 20 °C,

it becomes apparent that sedimentation in this case would be decidedly random.

In the above discussion the possible Brownian motion of the colloidal particles has not been explicitly taken into account, but it is obvious that for small enough colloids this factor will be an important or even decisive factor in the overall behavior of the particle. The self-diffusivity coefficient D_s, specifying the mean squared displacement of a diffusing colloidal particle per unit time in a solvent at temperature T through the relation $\left\langle |\vec{r}|^2 (t) \right\rangle = 6D_s t$, is given as [69]:

$$D_s = \frac{k_B T}{6\pi\eta R} \tag{2.7}$$

For a particle with a Stokes equivalent radius of 0.5 μm in water at 20 °C, the self-diffusivity coefficient takes a value of 0.43 $\mu m^2/s$. Because the mean square displacement scales as $1/R$ whereas the terminal velocity for a Stokes equivalent sphere of radius R scales as $V/R \propto R^2$ according to Equation 2.2, or alternately as Rd for an ellipsoid or disc-like particle according to equations 2.3 and 2.4, it becomes apparent that the Brownian motion of a colloidal particle quickly becomes increasingly important as it's volume decreases. However, the real world behavior of sedimenting dispersions is expected to be complex and for less dilute suspensions also dependent upon the modes of interaction between the individual particles. The following section will address such interactions in dispersions of a certain electrolyte strength, deriving several key features that critically effect the stability against coagulation and aggregation and thus also the sedimentational behavior of colloidal suspensions. For a review of the more complex effects of gravity and Brownian motion coupled with inter-particle forces such as those discussed in the next section, see [14].

2.2.2 DLVO-theory

Insoluble particles in a solvent form colloidal dispersions when forces are present to prevent the aggregation and subsequent sedimentational fall-out of the colloidal species. According to the classical DLVO-theory simultaneously developed in the 1940s by Russian scientists Derjaguin and Landau [11] and Dutch scientists Verwey and Overbeek [79], colloidal stability is achieved when the colloidal species is trapped in a local minimum of the potential energy contributed to by respectively attractive van der Waals forces and repulsive double layer interactions, or when the repulsive interactions permanently prevent flocculation. Figure 2.2 illustrates the typical shape of the DLVO-potential, with the shallow secondary minimum separated from the much deeper primary minimum by a potential barrier. If the kinetic energy of the colloidal particles is comparatively low relative to the barrier height when it is approached from the right, the primary minimum is effectively rendered inaccessible and the colloidal particles will be trapped in a

state of kinetic stability against coagulation – at the secondary minimum if the energy is small compared with its depth. The primary minimum is of finite depth due to excluded volume interactions that arise because the electron orbitals of the atoms of the colloidal particles cannot overlap. This feature is not always included in the DLVO-potential itself, but should be kept in mind.

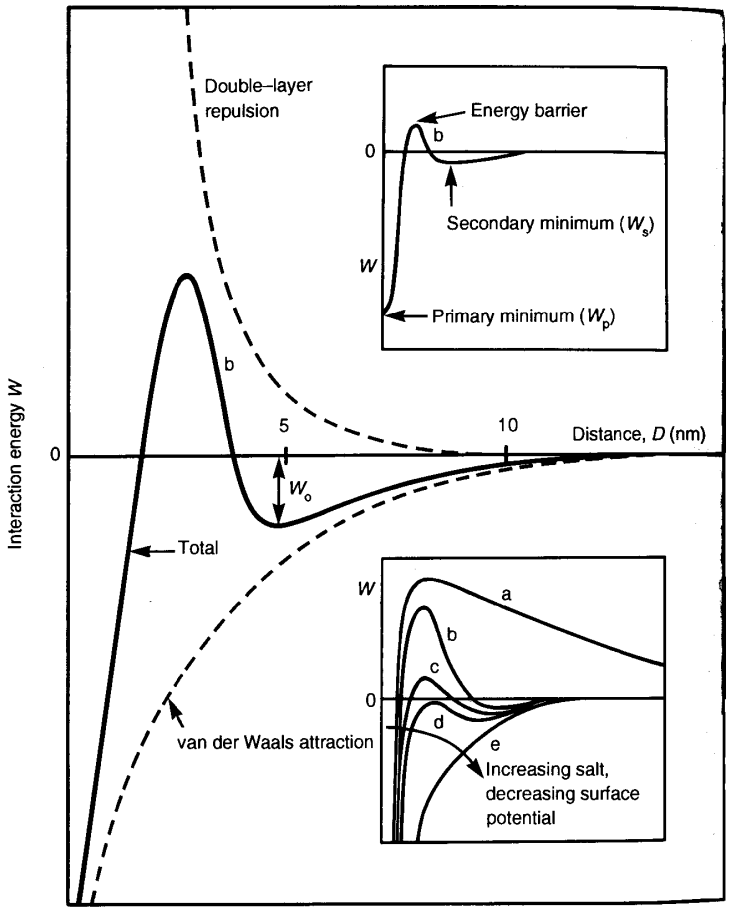

Figure 2.2: Classical illustration of the DLVO-potential, with the bottom inset showing the effect of an increasing electrolyte concentration. Retrieved from Israelachvili [33].

The traditional DLVO-potential takes into account two important modes of interaction between colloidal particles, namely van der Waals and double layer interactions. London-van der Waals interactions arise when fluctuations in the electron density of a particle induce a temporary state of polarization which interacts with the same time varying polarization states of other particles [58]. Other interactions, such as the attractive forces between

an ion or a permanent dipole and neutral particles are also attractive van der Waals forces. Double layer interactions in the present context arise when the surfaces of the colloidal particles carry permanent charges so that the ions present in the solvent experience a net electric potential giving rise to increased concentrations of one of the ionic species near the charged colloidal surfaces. Beyond a characteristic length scale known as the Debye length, these ions will effectively screen the repulsive electrostatic forces between the colloidal particles. The following section introduces the Debye screening length as a constant factor in the solution of a differential equation based on the Poisson equation, known from electrostatics, combined with a suitable Boltzmann distribution for the ionic concentration.

The Debye-Hückel screening length

A rigid body, such as a clay particle, with fixed surface charges in an ionic solvent will attract ions of the opposite charge to its surface so that a so-called double layer of charges is formed[6]. The surface charge density of the rigid body is σ_s, measured in charges per area, and the resulting electric potential in the solvent at the boundary with the charged surface is φ_s. Denoting the concentration of ions i of valency z_i at a position x in the solution as $c_{i,x}$, the total density of charges $\rho_{c,x}$ at this position can be written as:

$$\rho_{c,x} = e \sum_i z_i c_{i,x} \tag{2.8}$$

Here e is one elementary unit of positive electrical charge, or the charge of a positron. The charges of the double layer set up an electrical field $\vec{E}$ and a corresponding electric potential φ that according to electrostatical theory must obey Poisson's equation:

$$-\nabla \vec{E} = \nabla^2 \varphi = \frac{-\rho_{c,x}}{\epsilon_r \epsilon_0} = \frac{-e \sum_i z_i c_{i,x}}{\epsilon_r \epsilon_0} \tag{2.9}$$

Here ϵ_r is the dielectric constant of the solvent and ϵ_0 the vacuum electric constant. Equation 2.9 can be re-written using the following Boltzmann distribution, where $c_{i,\infty}$ is the concentration of ions of type i in regions where the electric potential $\varphi = 0$, taken to be the potential far from the charged surface (the notation stems from far away being taken as infinitely far away) [36]:

$$c_{i,x} = c_{i,\infty} \exp\left[-e z_i \varphi / k_B T\right] \tag{2.10}$$

Combining equations 2.9 and 2.10 results in the following Poisson-Boltzmann equation for the electric potential:

$$\nabla^2 \varphi = \frac{-e}{\epsilon_r \epsilon_0} \sum_i z_i c_{i,\infty} \exp\left[-e z_i \varphi / k_B T\right] \tag{2.11}$$

[6] More sophisticated models of the double layer and its internal structure are presented later on.

This differential equation must be supplemented with appropriate boundary conditions as well as a charge conservation law, and is in general difficult to solve. However, some simplifying conditions allow for analytical solutions. In the special case of a monovalent electrolyte so that $z_c = 1$, $z_a = -1$ and $c_{c,\infty} = c_{a,\infty} = c_\infty$, where c and a denotes properties of the cations and anions respectively, the Poisson-Boltzmann equation can be written in the following form:

$$\begin{aligned} \nabla^2\varphi &= \frac{-e}{\epsilon_r\epsilon_0}\sum_i z_i c_{i,\infty}\exp\left[-ez_i\varphi/k_BT\right] \\ &= \frac{-ec_\infty}{\epsilon_r\epsilon_0}\left(\exp\left[-e\varphi/k_BT\right] - \exp\left[e\varphi/k_BT\right]\right) \\ &= \frac{2ec_\infty}{\epsilon_r\epsilon_0}\sinh\left(\frac{e\varphi}{k_BT}\right) \end{aligned} \tag{2.12}$$

In the Debye-Hückel approximation, valid for strong electrolytes where $\varphi < k_BT/e$ so that $\sinh\left(e\varphi/k_BT\right) \approx e\varphi/k_BT$ and linearization is possible[7], Equation 2.12 can be further simplified:

$$\begin{aligned} \nabla^2\varphi &= \frac{2ec_\infty}{\epsilon_r\epsilon_0}\sinh\left(\frac{e\varphi}{k_BT}\right) \\ &\approx \frac{2ec_\infty}{\epsilon_r\epsilon_0}\left(\frac{e\varphi}{k_BT}\right) \\ &= \frac{\varphi}{\lambda_D^2} \end{aligned} \tag{2.13}$$

The electric potential is a function of position so that $\varphi = \varphi(\vec{r})$. With the simplifying assumption of a one-dimensional problem so that $\varphi = \varphi(x)$ with $x = 0$ at the surface of the rigid charged body, Equation 2.13 has the following simple solution:

$$\varphi(x) = A\exp\left[x/\lambda_D\right] + B\exp\left[-x/\lambda_D\right] \tag{2.14}$$

The electric potential goes to zero as x goes to infinity, so the constant A must equal zero. At the boundary with the charged surface where $x = 0$ the electric potential has a constant value φ_s. This means that the constant $B = \varphi_s$, yielding the final solution for the electric potential:

$$\varphi(x) = \varphi_s\exp\left[-x/\lambda_D\right] \tag{2.15}$$

λ_D is known as the Debye-Hückel screening length, or the Debye length, and can be expressed in the general case as [36]:

$$\lambda_D = \left[\frac{\epsilon_r\epsilon_0 k_BT}{e^2\sum_i c_{i,\infty}z_i^2}\right]^{1/2} \tag{2.16}$$

[7]The Debye-Hückel approximation becomes better the smaller φ is compared with k_BT/e, since the closer x is to zero, the more alike $\sinh(x)$ becomes to the linear function $f(x) = x$. At a temperature of 20 °C, the quantity $k_BT/e = 25$ mV.

The Debye length describes the length beyond which the electric potential has fallen by more than about 60 % relative to the potential at the charged surface. For the 1:1 electrolyte treated above, the quantity $\sum_i c_{i,\infty} z_i^2 = 2c_\infty$ so that in this case the Debye length is:

$$\lambda_D = \left[\frac{\epsilon_r \epsilon_0 k_B T}{2e^2 c_\infty} \right]^{1/2} \tag{2.17}$$

As en example, a 10^{-3} M solution of the 1:1 electrolyte NaCl in water at 20 °C = 293.15 K has a Debye length that can be calculated from Equation 2.17, yielding a value of 9.6 nm. It is worth noting that the Debye length is exclusively a property of the solvent and as such does not depend on the surface charge density nor any other property of the dispersed colloidal particles.

The double layer potential and its relation to the surface charge density

The above treatment of the Poisson-Boltzmann equation, Equation 2.11, in the Debye-Hückel regime assumed the surface charge σ_s of the rigid body was small compared with the electrolyte strength of the solvent so that linearization was possible. A more sophisticated treatment of Equation 2.11 yields the following expression for the electric potential [33, 36]:

$$\begin{aligned} \varphi(x) &= \frac{2k_B T}{e} \ln \left[\frac{1 + \tanh\left[e\varphi_s / 4k_B T\right] \exp\left[-x/\lambda_D\right]}{1 - \tanh\left[e\varphi_s / 4k_B T\right] \exp\left[-x/\lambda_D\right]} \right] \\ &\approx \frac{4k_B T}{e} \tanh\left[e\varphi_s / 4k_B T\right] \exp\left[-x/\lambda_D\right] \end{aligned} \tag{2.18}$$

The approximation is valid when $\tanh\left[e\varphi_s / 4k_B T\right] \exp\left[-x/\lambda_D\right] \ll 1$[8]. The linear Debye-Hückel regime is retrieved when $e\varphi_s / 4k_B T \ll 1$ so that $\tanh\left[e\varphi_s / 4k_B T\right] \approx e\varphi_s / 4k_B T$. In the Gouy-Chapman regime on the other hand, where the surface potential is high relative to the electrolyte strength so that $e\varphi_s / 4k_B T \gg 1$ and $\tanh\left[e\varphi_s / 4k_B T\right] \approx 1$[9], Equation 2.18 can be written as:

$$\varphi(x) \approx \frac{4k_B T}{e} \exp\left[-x/\lambda_D\right] \tag{2.19}$$

It is apparent that the potential φ_s at the boundary between the solvent and the rigid body, which is dependent both on the surface density of charges σ_s and the electrolyte strength, is an important quantity that amongst other things determines the type of approximations that can be

[8] The approximation of Equation 2.18 is based on the fact that for $y \ll 1$ the expression $\ln\left[(1+y)/(1-y)\right] \approx 2y$.

[9] The approximation that $\tanh\left[e\varphi_s / 4k_B T\right] \approx 1$ is fairly good already at $e\varphi_s / 4k_B T = 3$ where $\tanh\left[e\varphi_s / 4k_B T\right] = 0.995$.

made to the Poisson-Boltzmann equation. Starting from the ion concentration at the boundary, the relation between surface charge density and surface potential can be deduced. The concentration of ions $c_{i,s}$ at the boundary between the charged surface and the solvent is described by the previously defined Boltzmann distribution of Equation 2.10. This equation can be derivated with respect to x to yield the following:

$$\frac{dc_{i,x}}{dx} = c_{i,\infty}\frac{-ez_i}{k_BT}\exp\left[-ez_i\varphi/k_BT\right]\frac{d\varphi}{dx} \tag{2.20}$$

Summing over all ion species i and comparing the result with the Poisson-Boltzmann equation, Equation 2.11, further results in:

$$\begin{aligned}\sum_i \frac{dc_{i,x}}{dx} &= \sum_i c_{i,\infty}\frac{-ez_i}{k_BT}\exp\left[-ez_i\varphi/k_BT\right]\frac{d\varphi}{dx} \\ &= \frac{\epsilon_r\epsilon_0}{k_BT}\left(\frac{d^2\varphi}{dx^2}\right)\frac{d\varphi}{dx} \\ &= \frac{\epsilon_r\epsilon_0}{2k_BT}\frac{d}{dx}\left(\frac{d\varphi}{dx}\right)^2\end{aligned} \tag{2.21}$$

This equation can now be integrated to yield an expression for the additional concentration of ions at position x relative to the bulk concentration:

$$\begin{aligned}\sum_i c_{i,x} - \sum_i c_{i,\infty} &= \int_\infty^x \sum_i dc_{i,x} \\ &= \int_\infty^x \frac{\epsilon_r\epsilon_0}{2k_BT} d\left(\frac{d\varphi}{dx}\right)^2 \\ &= \frac{\epsilon_r\epsilon_0}{2k_BT}\left(\frac{d\varphi}{dx}\right)_x^2 - \frac{\epsilon_r\epsilon_0}{2k_BT}\left(\frac{d\varphi}{dx}\right)_\infty^2 \\ &= \frac{\epsilon_r\epsilon_0}{2k_BT}\left(\frac{d\varphi}{dx}\right)^2\end{aligned} \tag{2.22}$$

Rearranging and setting $x = 0$ so that all properties are calculated at the boundary between the solvent and the charged surface, this further becomes:

$$\sum_i c_{i,s} = \sum_i c_{i,\infty} + \frac{\epsilon_r\epsilon_0}{2k_BT}\left(\frac{d\varphi_s}{dx}\right)^2 \tag{2.23}$$

The electrical field at the boundary has a magnitude $E_s = \sigma_s/\epsilon_r\epsilon_0$ [33], and in general $E = d\varphi/dx$, so Equation 2.23 can be written as:

$$\begin{aligned}\sum_i c_{i,s} &= \sum_i c_{i,\infty} + \frac{\epsilon_r\epsilon_0}{2k_BT}\left(\frac{\sigma_s}{\epsilon_r\epsilon_0}\right)^2 \\ &= \sum_i c_{i,\infty} + \frac{\sigma_s^2}{2\epsilon_r\epsilon_0 k_BT}\end{aligned} \tag{2.24}$$

This important result connects the concentration of ions at the boundary with the surface charge density σ_s. The surface potential φ_s can now be related to σ_s by rearranging Equation 2.24 and inserting the Boltzmann distribution for $c_{i,s}$:

$$\begin{aligned} \sigma_s^2 &= 2\epsilon_r\epsilon_0 k_B T \left(\sum_i c_{i,s} - \sum_i c_{i,\infty} \right) \\ &= 2\epsilon_r\epsilon_0 k_B T \sum_i c_{i,\infty} \left(\exp\left[-ez_i\varphi_s / k_B T \right] - 1 \right) \end{aligned} \tag{2.25}$$

For a 1:1 electrolyte where the anion concentration equals the cation concentration so that $c_{c,\infty} = c_{a,\infty} = c_\infty$, this becomes:

$$\begin{aligned} \sigma_s &= \left(2\epsilon_r\epsilon_0 k_B T c_\infty \left(\exp\left[-e\varphi / k_B T \right] + \exp\left[e\varphi / k_B T \right] - 2 \right) \right)^{1/2} \\ &= \left(4\epsilon_r\epsilon_0 k_B T c_\infty \left(\cosh\left[e\varphi_s / k_B T \right] - 1 \right) \right)^{1/2} \\ &= \left(8\epsilon_r\epsilon_0 k_B T c_\infty \right)^{1/2} \sinh\left[e\varphi_s / 2k_B T \right] \end{aligned} \tag{2.26}$$

The transition to the last line makes use of the fact that $1 = \cosh^2 y - \sinh^2 y$ and that $\cosh 2y = \cosh^2 y + \sinh^2 y$. The result of Equation 2.26 can be rearranged to yield the following expression for the boundary potential φ_s as a function of the surface charge density σ_s for a 1:1 electrolyte:

$$\varphi_s = \frac{2k_B T}{e} \sinh^{-1}\left[\sigma_s / \left(8\epsilon_r\epsilon_0 k_B T c_\infty \right)^{1/2} \right] \tag{2.27}$$

For electrolytes with other compositions the boundary potential has to be deduced directly from Equation 2.25. Table 2.2 list the surface potential as a function of electrolyte strength for particles with a given surface charge density of -0.40 C/m, corresponding with the presumed surface charge density of fluorohectorite platelets as discussed in section 2.1.1. Values of the Debye length for 1:1, 2:1 and 3:1 electrolytes at different salt concentrations are also included.

Double layer interactions between two charged colloidal platelets

According to [33], the repulsive pressure $P(x')$ between two planar surfaces of equal charge densities separated by a variable distance x' in an ionic solvent can be written as:

$$P\left(x'\right) = k_B T \left(\sum_i c_{i,D}\left(x'\right) - \sum_i c_{i,\infty} \right) \tag{2.28}$$

Here $c_{i,D}$ denotes the concentration of ions i at the midplane D between the two platelets as a function of their separation x'. The previously defined quantity $c_{i,\infty}$ corresponds with the bulk ionic concentration. In general,

Table 2.2: Overview of the effects of salt concentration, in number of formula units per volume unit, on the Debye length and surface potential for colloidal solutions of platelets with a fixed surface charge density of -0.40 C/m in water at 20 °C. The Debye length was calculated according to equations 2.16 and 2.17, and the surface potential according to Equation 2.27 for the 1:1 electrolyte solutions.

Salt type z_c:z_a	Bulk salt concentration c_∞ [M]	Debye length λ_D [nm]	Surface potential φ_s [mV]
1:1	$1.0 \cdot 10^{-4}$	30.4	330
1:1	$1.0 \cdot 10^{-3}$	9.64	271
1:1	$3.0 \cdot 10^{-3}$	5.56	244
1:1	$6.0 \cdot 10^{-3}$	3.93	226
2:1	$1.0 \cdot 10^{-5}$	55.6	–
2:1	$1.0 \cdot 10^{-4}$	17.6	–
2:1	$1.0 \cdot 10^{-3}$	5.56	–
3:1	$1.0 \cdot 10^{-5}$	39.3	–
3:1	$1.0 \cdot 10^{-4}$	12.4	–
3:1	$1.0 \cdot 10^{-3}$	3.93	–

the ion concentrations at the midplane can be written in the form of the Boltzmann distribution presented in Equation 2.10, where φ_D is the total electric potential at the midplane:

$$c_{i,D} = c_{i,\infty} \exp\left[-ez_i\varphi_D/k_BT\right] \tag{2.29}$$

Under the assumption of a 1:1 monovalent electrolyte, equations 2.28 and 2.29 can now be combined to yield the following expression for the pressure:

$$\begin{aligned} P\left(x'\right) &= c_\infty k_B T \sum_i \left(\exp\left[-ez_i\varphi_D/k_BT\right] - 1\right) \\ &= c_\infty k_B T \left(\exp\left[-e\varphi_D/k_BT\right] + \exp\left[e\varphi_D/k_BT\right] - 2\right) \\ &\approx \frac{c_\infty e^2 \varphi_D^2}{k_B T} \end{aligned} \tag{2.30}$$

The approximation in the last line arises through a series expansion of the exponential terms[10], and is valid when the midplane potential φ_D is small.

[10]The approximation in Equation 2.30 was made using the following series expansion of $\exp[x]$, valid when $x^2 < \infty$:

$$\exp[x] = \sum_0^\infty \frac{x^n}{n!}$$

Assuming the midplane potential can be taken as the sum of the previously defined potentials $\varphi(x)$ from the two respective double layers at the midplane where $x = x'/2$ [33], the pressure between the two platelets can be expressed as:

$$P(x') \approx \frac{c_\infty e^2 \varphi_D^2}{k_B T} \approx \frac{4 c_\infty e^2 \varphi^2 (x'/2)}{k_B T} \tag{2.31}$$

Based on this result, the interaction free energy or what will be referred to as the double layer potential energy between the two platelets, can be found through integrating Equation 2.31, bringing the platelets in from infinity to a separation x':

$$\begin{aligned} V_{dl} &= -\int_\infty^{x'} P(x') dx' \\ &= -\frac{4 c_\infty e^2}{k_B T} \int_\infty^{x'} \varphi^2 \left(x'/2\right) dx' \end{aligned} \tag{2.32}$$

Inserting the expression for the electric potential derived in Equation 2.18, this becomes:

$$\begin{aligned} V_{dl} &= -\frac{4 c_\infty e^2}{k_B T} \int_\infty^{x'} \frac{16 (k_B T)^2}{e^2} \tanh^2 \left[e\varphi_s / 4 k_B T\right] \exp\left[-x'/\lambda_D\right] dx' \\ &= 64 c_\infty k_B T \tanh^2 \left[e\varphi_s / 4 k_B T\right] \lambda_D \exp\left[-x'/\lambda_D\right] \end{aligned} \tag{2.33}$$

In the linear Debye-Hückel regime, where the electric potential of one platelet in a strong electrolyte is given by Equation 2.15 under the approximation that $\tanh\left[e\varphi_s/4k_BT\right] \approx e\varphi_s/4k_BT$, the double layer potential between the two platelets becomes:

$$V_{dl} = \frac{4 c_\infty e^2 \varphi_s^2 \lambda_D}{k_B T} \exp[-x'/\lambda_D] \tag{2.34}$$

When the surface charge of the platelets is high relative to the electrolyte strength so that the electric potential of one platelet is described through Equation 2.19 with the approximation that $\tanh\left[e\varphi_s/4k_BT\right] \approx 1$, the double layer potential between the two platelets can be expressed as:

$$V_{dl} = 64 c_\infty k_B T \lambda_D \exp\left[-x'/\lambda_D\right] \tag{2.35}$$

Neglecting terms of order $(\pm e\varphi_D/k_BT)^4$ or higher and noting that the odd powers of $(\pm e\varphi_D/k_BT)$ cancel each other out, this results in:

$$P\left(x'\right) \approx c_\infty k_B T \left(1 + \frac{\left(-e\varphi_D/k_BT\right)^2}{2!} + 1 + \frac{\left(e\varphi_D/k_BT\right)^2}{2!} - 2\right) = \frac{c_\infty e^2 \varphi_D^2}{k_B T}$$

This approximation is valid when $\frac{(\pm e\varphi_D/k_BT)^4}{4!} \ll \frac{(\pm e\varphi_D/k_BT)^2}{2!}$. At a midplane potential of 25 mV, $\frac{(\pm e\varphi_D/k_BT)^4}{4!} / \frac{(\pm e\varphi_D/k_BT)^2}{2!} \approx 0.083$.

The van der Waals potential between two colloidal platelets

The van der Waals potential V_{vdW} between two colloidal particles with mass densities $\rho_{m,1}$ and $\rho_{m,2}$ occupying volumes V_1 and V_2 can be written as follows, assuming that individual interactions between temporary dipoles at $\vec{r}_1$ and $\vec{r}_2$ can be added pairwise and that the subsequent summation can be replaced with an integration [36]:

$$V_{vdW} = -\int_{V_1} dV_1 \int_{V_2} dV_2 \frac{C_{12}\rho_{m,1}\rho_{m,2}}{|\vec{r}_1 - \vec{r}_2|^6} \tag{2.36}$$

The replacing of the summation with integration is justified if the two colloidal particles have constant densities with an average number of constituent atomic species per volume unit. The constant C_{12}, determining the strength of the interactions, is chosen to be geometry independent, so that it can be moved outside the integral along with $\rho_{m,1}$ and $\rho_{m,2}$:

$$\begin{aligned} V_{vdW} &= -C_{12}\rho_{m,1}\rho_{m,2} \int_{V_1} dV_1 \int_{V_2} dV_2 \frac{1}{|\vec{r}_1 - \vec{r}_2|^6} \\ &= \frac{-A_{12}}{\pi^2} \int_{V_1} dV_1 \int_{V_2} dV_2 \frac{1}{|\vec{r}_1 - \vec{r}_2|^6} \end{aligned} \tag{2.37}$$

$A_{12} = \pi^2 C_{12}\rho_{m,1}\rho_{m,2}$ is called the Hamaker constant and is measured in units of energy. The above expression does not take into account the finite speed of electromagnetic waves nor possible distortions to the pairwise interactions that might arise from the presence of nearby atoms and molecules. When the colloidal particles of equations 2.36 and 2.37 are two equal platelets of thickness d and mass density ρ_m separated by a distance $x' \gg d$, the van der Waals potential between them can be written as follows [36]:

$$V_{vdW} = \frac{-\pi C d^2 \rho_m^2}{2x'^4} = \frac{-A_{12}d^2}{2\pi x'^4} \tag{2.38}$$

In the opposite case where $x' < d$, the expression reads [36]:

$$V_{vdW} = \frac{-\pi C \rho_m^2}{2x'^2} = \frac{-A_{12}}{2\pi x'^2} \tag{2.39}$$

The full DLVO-potential

The combined DLVO-potential as a function of the separation distance between two charged colloidal platelets can now be written through the expressions derived in equations 2.33, 2.34, 2.35, 2.38 and 2.39. For a 1:1 electrolyte the combination of the full double layer interaction potential with the van

der Waals contribution yields:

$$V_{DLVO}\left(x' \gg d\right) = 64c_\infty k_B T \tanh^2\left[e\varphi_s/4k_BT\right]\lambda_D \exp\left[-x'/\lambda_D\right] - \frac{A_{12}d^2}{2\pi x'^4} \quad (2.40)$$

$$V_{DLVO}\left(x' < d\right) = 64c_\infty k_B T \tanh^2\left[e\varphi_s/4k_BT\right]\lambda_D \exp\left[-x'/\lambda_D\right] - \frac{A_{12}}{2\pi x'^2} \quad (2.41)$$

The following section will address the subject of colloidal stability in the specific case where the colloidal particles are fluorohectorite platelets.

Colloidal stability of fluorohectorite dispersions in the DLVO-regime

It section 2.1.1, it was determined that fluorohectorite clay platelets have a surface charge density of approximately -0.40 C/m. Consider an example where such platelets are dispersed in a 10^{-3} M 1:1 electrolyte like NaCl at a temperature of 20 °C = 293.15 K. This is an approximation to the typical water-salt solutions utilized in this project for dispersing Na- or Li-fluorohectorite platelets. At this temperature, a 10^{-3} M 1:1 electrolyte has a Debye length of 9.6 nm according to Equation 2.17, and if one assumes the platelets are clay particles, the Hamaker constant will have a value of around 10^{-19} J [33]. From the relationship between the surface charge density and surface potential found in Equation 2.27, the surface potential for the platelets in this system will be 271 mV, which is about ten times higher than the low potential limit of 25 mV. This means that the expression of Equation 2.35 should be used to describe the double layer potential energy between the two platelets. Alternately, one can also use the non-approximated expression of Equation 2.33.

Previous studies [12] have indicated that fluorohectorite particles in water exist as stacked structures comprised of between 20 and 100 unit layers. Since the 2wl repetition along the stacking direction for Na-fluorohectorite is 1.5 nm, this corresponds with particle thicknesses ranging between 30 nm and 150 nm. In this thickness regime, the expression of Equation 2.39 can be used for the van der Waals contribution to the DLVO-potential, which hence becomes independent of particle thickness. The results of combining Equation 2.33 with Equation 2.39 to form the full DLVO-potential for fluorohectorite platelets in aqueous solutions of electrolyte strengths of $1 \cdot 10^{-3}$ M and $3 \cdot 10^{-3}$ M, respectively, are shown in Figure 2.3. The potentials obtained by considering single unit layer platelets are also included, where the platelet thicknesses have been set to a value of $d = 1$ nm. From the inset of Figure 2.3, potential minima are visible at platelet separations of 36 nm and 73 nm for respectively the $3 \cdot 10^{-3}$ M and $1 \cdot 10^{-3}$ M solutions – the graphs are valid when the platelet thicknesses are larger than the involved inter-platelet separations. For the thin platelets the DLVO-potentials featuring

the given parameters are well approximated as being overall repulsive for all separations beyond the primary minimum.

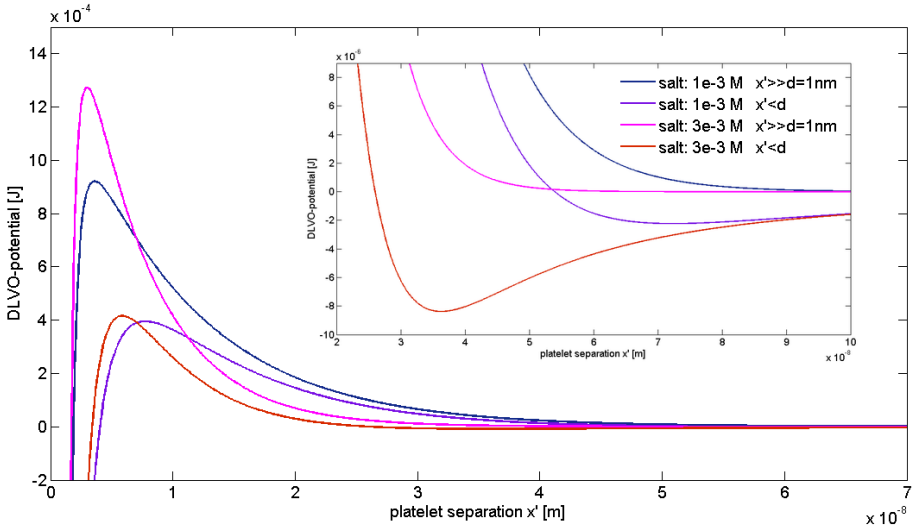

Figure 2.3: DLVO-potentials for platelets with a Hamaker constant of 10^{-19} J and a surface charge of -0.40 C/m^2 in electrolyte solutions. In the inset the axes have been scaled relative to the background figure, and illustrate the presence of potential minima.

Extended DLVO theory, and other models for the interaction between colloidal platelets

The DLVO-theory in its simple form described in the previous sections have found numerous uses in the field of colloid science. Modifications to this theory account for more subtle features of the ion distributions around charged surfaces in electrolyte solvents. One such feature is the reduced mobility of the counter-ions relatively close to the charged particle surface, in the so-called diffuse double layer, and the near complete fixation of the ions even closer to the surface, characterized as belonging to the Stern or Helmholtz layer [33]. This view of the double layer is commonly referred to as Stern layer theory [77]. Some authors [65, 45] are however, clearly critical towards the classical DLVO-theory and argue that simpler explanations which account equally well or better for the experimentally observed features of colloidal dispersions have been proposed. Sogami, Ise and Smalley [65] for istance, absolutely refute the DLVO-theory, and present in its stead a theory known as the Coulombic attraction theory, featuring long-range attractive forces of electromagnetic origin between like-charge colloids in electrolyte suspensions. McBride and Baveye [46] argue that a range of experimental

features of colloidal dispersion are today known not to be compatible with the DLVO-theory. Sogami and Ise [66] point out that the DLVO-theory only considers interactions between colloidal particle pairs, and that it is therefore only valid in highly diluted systems. Experimental results possibly supporting this [46], were presented by Crocker and Grier [8] in studies on like-charge spherical colloids suspended in water. Crocker and Grier found that, for large water volumes, the sphere interaction potential was overall repulsive whereas when the spheres were confined to a smaller volume, the appearance of an apparently attractive potential minimum was observed at spheres separations of around $2-3$ μm. McBride and Baveye [46] argue that the effect of confining walls in the Crocker and Grier study [8] might represent effects that could be expected to occur also from the presence of other colloidal particles. The results of the Crocker and Grier study does however support that the DLVO-theory is not fundamentally incorrect, but that it is misused when applied to non-dilute dispersions.

2.2.3 Hydration forces

In section 2.2.2 the DLVO-theory was presented as a means of predicting or understanding the stability of a colloidal dispersion at varying electrolyte concentrations. A closer look at the DLVO-potentials discussed in that section, reveals that there are important features of dispersions of lamellar water-intercalating colloids that the continuous medium DLVO-theory does not explain. It is well established that for smectite and vermiculite clay platelets the repetition distance d along the stacking direction of the unit layers varies with the amount of intercalated water, and for Na-fluorohectorite stable hydration states have been identified with d-values of 1.0 nm, 1.2 nm and 1.5 nm [9]. The DLVO-potential (which has a maximum barrier height at a separation distances larger than 2.5 nm in a 10^{-3} M 1:1 electrolyte for all the cases discussed in Figure 2.3 – a result that should however be used with caution due to the large uncertainties in critical parameters such as the Hamaker constant), cannot account for the three stable hydration states, and especially so because the clay also hydrates at humid atmospheric conditions [9]. It becomes apparent that the DLVO-theory does not account for the hydration and crystalline swelling properties of lamellar clay particles in aqueous suspensions and it is necessary to address so-called hydration forces, arising in the present discussion between hydrophilic surfaces in water at small separations, in order to understand the water intercalating properties of clay platelets and other layered structures. Hydration forces are not as well theoretically described as the DLVO-forces, but are well experimentally verified. Israelachvili and Pashley [34], measuring the hydration force between mica surfaces, concluded that although this force was found to be overall repulsive for separation distances below about 4 nm it did not decay monotonically but rather, for separations smaller than about 1.5 nm, showed

oscillatory variations with a mean periodicity of 0.25 ± 0.03 nm. This periodicity length is roughly equal to the diameter of a water molecule. Israelachvili [33] summarizes that potential minima at negative energies, i.e. attractive minima, were identified in the case of the mica platelets for separations of approximately 0, 0.28 and 0.56 nm, which correspond fairly well with the observed interlayer separations for the stable hydration states of Na-fluorohectorite described above when the individual unit layers have a thickness of around 1 nm. The convention is thus to consider these hydration states as containing respectively 0, 1 or 2 water layers [9]. Aalerud [1] reports on four stable hydration states observed in Ni-fluorohectorite, at repeat distances of respectively 1.1 nm, 1.4 nm, 1.6 nm and 1.8 nm. The smaller separations between successive hydration states observed for Ni- relative to Na-fluorohectorite could be related to the way in which these different clays hydrate. This possibility is further discussed in the following section.

The structure of clay water layers

Several papers have been dedicated to determining the structure of clay water contents. It is seen that the nature of the intercalated charge balancing cation as well as the origin, position and density of the layer charges are determining parameters in this discussion [63]. The water molecules can coordinate via ion-dipole bonds to the intercalated cations or via dipole-dipole bonds to the clay layer surfaces, whereas the cation can form so-called inner sphere or outer sphere complexes [63], depending on whether it is bound directly via ion-dipole bonds to the clay surface or via ion-dipole bonds to a complete shell of water molecules that via dipole-dipole bonds are associated with one or both opposing clay unit layers. It is seen that the swelling properties[11] of clays are critically dependent upon the intercalated cation valency and the ability of the cation to solvate in water. Odom [54] and more recently Skipper et al. [63] summarize that upon hydration the monovalently intercalated Li- and Na-smectites exhibit in general extensive colloidal swelling whereas the often more naturally common smectites with a large portion of intercalated divalent Ca^{2+} and Mg^{2+} [54], or monovalent K^{+} [63], show practically no colloidal swelling even when fully hydrated.

Ducker and Pashley [13] have investigated the effect that divalent cations in a water solution exerts upon the force between mica platelets. These authors found that divalent rod-shaped diamine cations absorbed unto the mica surfaces so strongly as to almost completely neutralize the surface

[11] In general, the swelling of smectite clays with increasing water content happens in two stages. Crystalline swelling, governed by hydration forces, corresponds with the intercalation of defined layers of water between the platelet surfaces whereas colloidal or osmotic swelling results as the stacked particles delaminate into single unit clay layers and approach the regime described by the DLVO-theory.

charges, leading to a disappearance of the repulsive electrostatic forces and the appearance of a strong adhesive potential minimum at a plates separation distance of around $0.8 - 0.9$ nm. The same charge neutralizing effect was to a more moderate degree observed when the mica plates were immersed in a $CaCl_2$ solution. Skipper [63] argues that outer-sphere forming divalent cations act as charge balancing pillars between adjacent unit layers, precluding the colloidal swelling seen in monovalently intercalated Li- and Na-smectites. The lack of swelling properties in K-smectites is explained by the tendency for K^+-ions to form inner sphere complexes both to tetrahedral and octahedral charge sites. In contrast, Li^+-ions are seen to form outer sphere complexes, whereas Na^+-ions are thought to form inner sphere complexes to tetrahedral charge sites and outer sphere complexes to the deeper octahedral charge sites [63] that are found in for instance fluorohectorites. Israelachvili [33] summarizes, based on results obtained by Kjellander et al. [35], Marra [43] and others, that so-called ion-correlation effects between strongly negatively charged surfaces in $CaCl_2$ solutions, have been shown to effectively cause the appearance of attractive short-range forces. According to Israelachvili, these results could explain the observed non-swelling characteristics of negatively charged clay surfaces in the presence of divalent cations [33].

2.3 Colloidal liquid crystals

The possibility of order arising in colloidal dispersions due to shape anisotropies in the colloidal species was introduced already in section 2.1.1, and briefly explained in that section based on the thermodynamic considerations of Onsager [55]. The analytical results obtained for hard-rod colloids are however not directly transferable to fluorohectorite systems, as the colloidal species in this case consist of platelet-like particles that are both irregularly shaped and highly polydisperse. Furthermore, fluorohectorite platelets as well as other charged particles are not hard, i.e. short-range repulsive only, but are also affected by long-range repulsive forces, according to the DLVO-theory, or possibly also by long-range attractive forces, according to the Columbic attraction theory [65]. Computer simulations taking into account hard-core interacting platelets [15, 76], have shown that liquid crystalline phases do form in suspensions of platelet-shaped colloids. As the formation of ordered phases in systems also affected by long-range forces is a well documented experimental fact, the current section will not delve further into the thermodynamic or other origins of liquid crystalline order in colloidal systems. Rather the focus in the present discussion will be on the characterization of the uniaxial nematic via a quantity known as the order parameter, and on the aligning and deforming effects which external factors such as container walls or applied fields can exert on this phase. At the end of this section

the issue of light propagation in anisotropic media will be addressed. This topic is relevant for the observation of liquid crystalline samples between crossed polarizers, which is an extensively used first method for identifying anisotropic phases through their birefringent properties. Presently however, the nematic order parameter will be deduced along with the introduction of the so-called director, which is also later discussed in connection with light propagation.

2.3.1 The director field and the nematic order parameter

The current section deals with properties of a liquid crystalline phase known as the nematic. The presence of nematic order in fluorohectorite dispersions was already discussed in section 2.1.1. As shown in Figure 2.4, nematic order is present in a colloidal dispersions when the colloidal species show a preferential orientation. The director $\vec{n}$ is a unit vector specifying the aver-

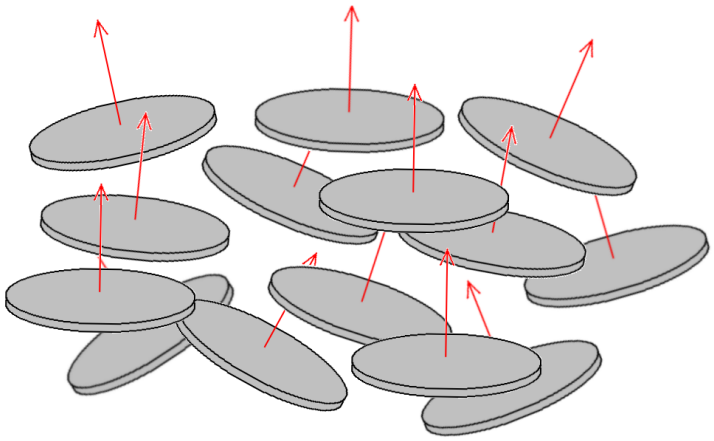

Figure 2.4: Illustration of the orientational order of a nematic. The platelets' face normals, corresponding with their optical axes, are illustrated by the red arrows. The average direction of the red arrows gives the nematic director.

age orientation of the nematogens within a volume of the nematic phase. It is common to define the director so that it coincides with the average orientation of the optical axes. The meaning of the term optical axis is discussed in section 2.3.3 for uniaxial nematics. In most cases the director orientation is however not uniform throughout the extent of the nematic phase, but is a function of position and can be written as a director field $\vec{n}\left(\vec{r}\right) = \vec{n}\left(x, y, z\right)$. For a given local director orientation, there is a distribution of orientations of the nematogens around this average value. Choosing a coordinate system so that the local director points along the angular coordinate θ, the fraction of nematogens oriented with their optical axis within the solid angle $d\theta d\phi$

around the direction (θ, ϕ) can be written as:

$$\omega(\theta, \phi) \sin\theta d\theta d\phi \tag{2.42}$$

Because for a given domain of a nematic phase there are two equivalent choices for the director orientation, i.e. either $\vec{n}$ or $-\vec{n}$, the distribution function has the property $\omega(\theta, \phi) = \omega(\pi - \theta, \phi)$. Normalization furthermore requires that:

$$1 = \int_0^{2\pi} \int_0^{\pi} \omega(\theta, \phi) \sin\theta d\theta d\phi \tag{2.43}$$

In the case of uniaxial symmetry where the distribution function is independent on ϕ, this condition of normalization can be rewritten as:

$$1 = 2\pi \int_0^{\pi} \omega(\theta) \sin\theta d\theta = \int_0^{\pi} \omega'(\theta) \sin\theta d\theta \tag{2.44}$$

The new orientational distribution function $\omega'(\theta) = 2\pi\omega(\theta)$ can be expanded as a series of Legendre polynomials in $\cos\theta$ [69]:

$$\omega'(\theta) = \sum_0^{\infty} \frac{2l+1}{2} S_l P_l(\cos\theta) \tag{2.45}$$

Here P_l are the Legendre polynomials of degree l accompanied by the series coefficients S_l. The first few Legendre polynomials in $\cos\theta$ are listed in Table 2.3.

Table 2.3: The first four Legendre polynomials in $\cos\theta$.

l	P_l
0	1
1	$\cos\theta$
2	$(1/2)\left(3\cos^2\theta - 1\right)$
3	$(1/2)\left(5\cos^3\theta - 3\cos\theta\right)$

The Legendre polynomials are orthogonal to each other [69]:

$$\int_0^{\pi} P_l(\cos\theta) P_k(\cos\theta) \sin\theta d\theta = \frac{2}{2l+1} \delta_{lk} \tag{2.46}$$

Because of this orthogonality, the series coefficients S_l can be found by multiplying each side of Equation 2.45 with $P_k(\cos\theta)$ and integrating over θ:

$$\int_0^{\pi} P_k(\cos\theta) \omega'(\theta) \sin\theta d\theta = \sum_0^{\infty} \frac{2l+1}{2} S_l \int_0^{\pi} P_l(\cos\theta) P_k(\cos\theta) \sin\theta d\theta \tag{2.47}$$

The only non-zero contribution of the sum comes from the term where $l = k$:

$$\int_0^{\pi} P_k(\cos\theta)\,\omega'(\theta)\sin\theta d\theta = \frac{2l+1}{2} S_k \frac{2}{2l+1} \tag{2.48}$$

Hence the series coefficients are given through the following relation:

$$S_l = \int_0^{\pi} P_l(\cos\theta)\,\omega'(\theta)\sin\theta d\theta = \langle P_l \rangle \tag{2.49}$$

For the first Legendre polynomial where $l = 0$, the right side of Equation 2.49 reduces to the normalization integral so that $S_0 \equiv 1$. When $l = 1$ the integral equals the expectation value of the even function $\cos\theta$ in the interval from 0 to π, yielding $S_1 \equiv 0$. The first non-zero series coefficient S_l after the constant $S_0 \equiv 1$ is hence the S_2 term, expressed through Equation 2.49 as:

$$S_2 = \int_0^{\pi} P_2(\cos\theta)\,\omega'(\theta)\sin\theta d\theta = \left\langle \frac{3\cos^2\theta - 1}{2} \right\rangle \tag{2.50}$$

S_2 is characteristic of the degree of order and is known as the nematic order parameter [69]. In the theoretical case of a perfectly aligned nematic so that all the nematogens are oriented at $\theta = 0$, the expectation value $\langle 3\cos^2\theta - 1 \rangle = 2$ and so the order parameter $S_2 = 1$. In the isotropic phase where all orientations are equally likely, the orientational distribution function $\omega'(\theta)$ uniformly weights all angles and can hence be placed outside the integral yielding the following expression for the order parameter in the isotropic state:

$$\begin{aligned} S_2^I &= \omega'(\theta) \int_0^{\pi} \left(\frac{3\cos^2\theta - 1}{2} \right) \sin\theta d\theta \\ &= \omega'(\theta) \left[\frac{\cos\theta \sin^2\theta}{2} \right]_0^{\pi} = \omega'(\theta)\,[0] = 0 \end{aligned} \tag{2.51}$$

It can be proved [69] that the difference $\Delta n = n_{\parallel} - n_{\perp}$ in refractive indexes responsible for the birefringent properties of a nematic phase is proportional to the nematic order parameter S_2. The birefringence of a liquid crystalline sample therefore indicates the order.

2.3.2 Deformations of the liquid crystalline nematic in external fields

The director field of a typical liquid crystal in its nematic phase, as introduced in the previous section, is usually not uniform throughout the extent of the phase unless specific measures are taken to ensure it. There are mainly three ways by which manipulation of the director field can be achieved. These include field, flow and wall induced alignments. The former and latter will be further treated in the following sections, and will

be connected in a discussion on the so-called Fréedericksz transition in Na-fluorohectorite dispersions later on. Flow induced alignment is a well known feature of dispersions of shape-anisotropic colloids, where an increased local ordering of the colloidal species occurs when the suspensions for instance are contained between walls, and the movement of one wall along with the no-slip condition at the wall boundary induce a shear [36]. The subject of hydrodynamics is an involved one from the startout, and for suspensions containing shape-anisotropic colloids, the director field features in as a new hydrodynamic variable. In the current discussion, it will be sufficient to consider flow induced birefringence as a qualitative feature that indicates the presence of shape-anisotropic colloids. Flow birefringence in clay-water suspensions have been observed for instance in the case of bentonite [24]; here the presence of flow-induced birefringence was found to be indicative of the possibility for the at-rest isotropic suspensions undergoing phase transitions to liquid crystalline states when the colloid concentration was increased.

The role of aligning walls

Liquid crystalline colloidal particles are seen to align with container walls in two distinguishable fashions. Planar wall anchoring describes the case where the director is oriented parallel with the aligning wall, whereas homeotropic anchoring is achieved when the director is oriented perpendicular to the aligning wall. The two configurations are illustrated in Figure 2.5.

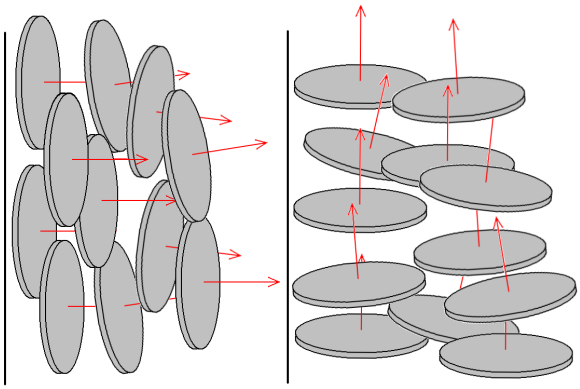

Figure 2.5: Illustration of homeotropic anchoring (left) and planar wall anchoring (right) of disc-like nematogens.

Azevedo et al. [10] have shown that the standing nematic phase of Na-fluorohectorite clay platelets in saline solutions is strongly anchored homeotropically to common glass walls, and that this anchoring close to the walls persist even when a magnetic field of 2 T favoring re-orientation is

applied to the phase. Wall anchoring is an important phenomenon in both practical applications of liquid crystals and in the study of defects, whose character can be used to distinguish different liquid crystalline phases from each other. Liquid crystal displays utilize wall anchoring by placing rod-like nematogens between two surface modified or grafted plates that favor director alignments at right angles to each other, causing a continuous twist of the phase in the volume between the two plates [7]. Polarizers with their axes oriented along the imposed director orientation are placed outside the grafted plates and when incident white light encounters one of the polarizers, the component with a polarization compatible with the polarizer axis is transmitted and allowed to enter the nematic phase. As this plane-polarized light traverses the twisted nematic it will have its polarization axis rotated in response to the rotating director field so that when it encounters the second polarizer it will be polarized along this polarizer's axis and therefore transmitted [7]. An electrical field can be applied to this setup via electrodes placed parallel with the polarizers and grafted plates. At sufficient field strengths the nematogens will orient with the field and the twist imposed by the grafted plates will be lost as a uniform director field develops. In this state the nematic phase no longer changes the polarization of the light transmitted by the first polarizer and it is hence blocked by the second.

Particle anisotropies and field induced alignment

In the previous section on wall alignment, the possibility of orienting a nematic phase via the application of an external field was briefly introduced. The reason for this orientational response to external fields is rooted in the anisotropy of the nematogens. As discussed, shape anisotropy is a prerequisite for liquid crystalline order due to competing effects between orientational and translational entropy as functions of the nematogen density. Likewise, anisotropy in the electrical permittivity or magnetic permeability of a material is required in order for the material to orient in response to applied electric or magnetic fields. These anisotropies are usually expressed as follows, where $\Delta\epsilon$ denotes the dielectric permittivity and $\Delta\chi$ the diamagnetic susceptibility anisotropy:

$$\Delta\epsilon = \epsilon_{\parallel} - \epsilon_{\perp} \tag{2.52}$$

$$\Delta\chi = \chi_{\parallel} - \chi_{\perp} \tag{2.53}$$

The $_{\parallel}$ subscript denotes the electric permittivity and magnetic susceptibility for fields $\vec{E} \parallel \vec{n}$ and $\vec{B} \parallel \vec{n}$, whereas the $_{\perp}$ subscript denotes the same parameters for fields $\vec{E} \perp \vec{n}$ and $\vec{B} \perp \vec{n}$, respectively. The director $\vec{n}$ will be further discussed in section 2.3.3, dealing with the propagation of light in anisotropic media. The current section provides a background for that discussion, as well as for the discussion of section 2.3.2 on the Fréedericksz

transition. A common background of electromagnetism can be found for reference in Appendix A.

The orientational response of a dielectrically or diamagnetically anisotropic particle in an electric or magnetic field can be found through minimizing the electric or magnetic free energy. The free energy densities $f_{\vec{E}}$ and $f_{\vec{B}}$, attributable respectively to the presence of an electric or magnetic field, can be written for linear media as [22, 26]:

$$f_{\vec{E}} = -\frac{1}{2}\vec{E}\cdot\vec{D} \tag{2.54}$$

$$f_{\vec{B}} = -\frac{1}{2}\vec{B}\cdot\vec{H} \tag{2.55}$$

Because $\vec{B} = \bar{\mu}\vec{H}$, an expression can be found for the magnetic free energy density as a function of $\vec{H}$ and of the orientation of the nematic director $\vec{n}$ with respects to $\vec{H}$. The electric case will not be further treated in the present discussion. The field $\vec{H}$ can be decomposed into two components, one parallel and one perpendicular to the director, so that the magnetic field $\vec{B}$ can be expressed as:

$$\begin{aligned}
\vec{B} &= \mu_0\vec{H} + \mu_0\chi\vec{H} \\
&= \mu_0\vec{H} + \mu_0\chi_{\parallel}\vec{H}_{\parallel} + \mu_0\chi_{\perp}\vec{H}_{\perp} \\
&= \mu_0\vec{H} + \mu_0\chi_{\parallel}\left(\vec{n}\cdot\vec{H}\right)\vec{n} + \mu_0\chi_{\perp}\vec{H} - \mu_0\chi_{\perp}\left(\vec{n}\cdot\vec{H}\right)\vec{n} \\
&= \mu_0\vec{H} + \mu_0\chi_{\perp}\vec{H} + \mu_0\Delta\chi\left(\vec{n}\cdot\vec{H}\right)\vec{n}
\end{aligned} \tag{2.56}$$

The expression for the magnetic free energy density can then be written as:

$$f_{\vec{H}} = -\frac{1}{2}\left[\mu_0 H^2 + \mu_0\chi_{\perp}H^2 + \mu_0\Delta\chi\left(\vec{n}\cdot\vec{H}\right)^2\right] \tag{2.57}$$

It is worth noting that only the last term of this equation depends on the relative orientation of the director with respects to the field. Minimization of this term will therefore determine the most energetically favorable orientation of the director in response to the applied field. Because $(\vec{n}\cdot\vec{H})^2$ reaches it's maximum when $\vec{n} \parallel \vec{H}$, it will be favorable for nematogens of positive susceptibility anisotropy $\Delta\chi > 0$ to orient with their director parallel with the field $\vec{H}$. The minimum of $(\vec{n}\cdot\vec{H})^2$ on the other hand occurs when $\vec{n} \perp \vec{H}$, so that nematogens of negative susceptibility anisotropy $\Delta\chi < 0$ will orient with their director perpendicular to the field $\vec{H}$.

Free energy minimization for discotic nematics subjected to magnetic fields

As seen in the two previous sections concerning the aligning effects of walls and external fields, the orientation of a nematic phase can be made to vary.

When an initially aligned nematic phase with a homogeneous director field is subjected to a sufficiently strong force favoring another director orientation, the director field becomes distorted and the free energy of the phase changes as the system now is able to do work through the action of restoring elastic forces. The change ΔF in the Helmholtz free energy F resulting from director field distortions can be expressed as a volume integral of the corresponding change Δf in the free energy density f [57]:

$$\Delta F = \int \Delta f dV \tag{2.58}$$

If $a\,|\nabla \vec{n}| \ll 1$, i.e. the director field $\vec{n}$ varies little over the extent of a where a is a typical nematogenic distance, the change in the free energy density can be expressed as a power series in $\nabla \vec{n}$ [57]. Oseen [56] and Frank [21], as well as Zocher [83], found that three surviving terms in the series expansion of Δf correspond to three basic modes of distortion of the director field for uniaxial nematics, each contributing an independent term to the Helmholtz free energy F of the system. The three distortions modes are respectively called splaying, twisting and bending, and are illustrated in Figure 2.6. The second order approximation to the increase Δf in the Helmholtz free energy density of a nematic phase due to director field distortions can thus be written in the form of the Frank-Oseen equation [56, 21, 36]:

$$\Delta f_{123} = \frac{1}{2}\left[K_{11}\left([\nabla \cdot \vec{n}]\right)^2 + K_{22}\left(\vec{n} \cdot [\nabla \times \vec{n}]\right)^2 + K_{33}\left(|\vec{n} \times [\nabla \times \vec{n}]\,|\right)^2\right] \tag{2.59}$$

Here the series coefficients K_{11}, K_{22} and K_{33} are bulk elastic constants called Frank moduli, related respectively to splay, twist and bend deformations. The Frank moduli are measured in units of force. For disc-like nematogens, experimental as well as theoretical studies have found that generally $K_{22} \geq K_{11} > K_{33}$ [80, 67].

A fourth elasticity term writes out as [68];

$$f_{24} = \frac{-K_{24}}{2}\nabla\left(\vec{n} \cdot (\nabla \cdot \vec{n}) + \vec{n} \times (\nabla \times \vec{n})\right) \tag{2.60}$$

K_{24} is called the saddle-splay constant [68]. Because the contribution from f_{24} to the volume integral of Equation 2.58 can be transformed into an integral over the surfaces of the phase [68], the K_{24} elasticity constant is termed a surface contribution.

The free energy density has one further surface term which arises due to the interaction of the director field with boundaries. This term can be expressed as [68]:

$$f_s = \frac{C}{2}\left(1 - (\vec{n} \cdot \vec{n}_s)^2\right) \tag{2.61}$$

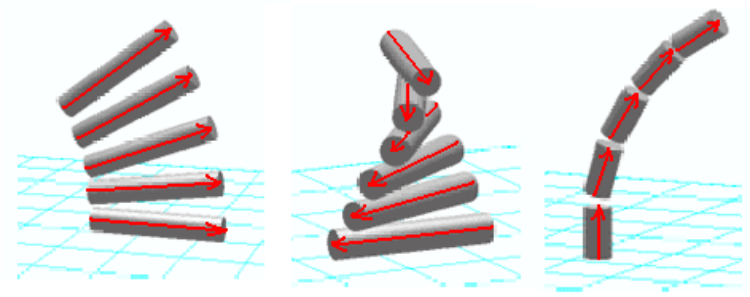

Figure 2.6: Illustration of splay, twist and bend distortions (left to right) for rod-like nematogens. If the long cylindrical axis is shortened, the figure illustrates the same distortion modes for discs. The red arrows indicate the local director. Figure retrieved from [50] and slightly modified.

Here $C > 0$ is a constant and $\vec{n}_s$ the preferred orientation of the director at the boundary. From this expression it is seen that the local free energy close to the boundary, in the absence of other forces influencing the director field, is minimized when $\vec{n} \cdot \vec{n}_s = 1$, so that the angle between $\vec{n}$ and $\vec{n}_s$ equals $0°$ and the two vectors are parallel.

One last contribution to the Helmholtz free energy density of a nematic phase will be considered. This contribution arises when the phase is affected by an auxhilary magnetic field $\vec{H}$. According to the discussion of section **??**, the contribution to the free energy density due to an applied magnetic field can be written as:

$$f_{\vec{H}} = -\frac{1}{2}\left[\mu_0 H^2 + \mu_0 \chi_\perp H^2 + \mu_0 \Delta\chi \left(\vec{n} \cdot \vec{H}\right)^2\right] \tag{2.62}$$

The Fréedericksz transition in fluorohectorite dispersions

The previous sections have introduced three different forms of director field distortions, as well as a theoretical background for evaluating the free energy of a deformed uniaxial nematic. The present section deals with a special form of director field distortions known as a Fréedericksz transition. The Fréedericksz transition in nematics occur when a reorienting field is applied to an aligned phase. In the present discussion only magnetic fields will be dealt with. Below a certain threshold value, this applied field is too weak to affect the aligned phase and no director field distortions are seen. However, above the threshold the field becomes strong enough to induce distortions as it becomes favorable for the nematogens to align with the field. According to the discussion of the previous section, two different types of alignment are seen. For nematogens of positive $\Delta\chi$, the stable configuration for sufficient field strengths is achieved when $\vec{n} \parallel \vec{H}$, whereas for nematogens of negative

$\Delta\chi$ the stable configuration occurs when $\vec{n} \perp \vec{H}$. From Azevedo et al. [10] it is known that Na-fluorohectorite platelets have a negative diamagnetic susceptibility anisotropy $\Delta\chi < 0$. The current section will thus address the Fréedericksz transition for disc-like nematogens of negative $\Delta\chi$.

Consider a magnetically aligned standing nematic of disc-like nematogens of negative $\Delta\chi$ where the average platelet face orientation is parallel with the xz-plane of a right handed cartesian coordinate system due to long term exposure of the phase to a magnetic field of sufficient field strength pointing along x, so that a stable state has been reached. The conventional nematic director in this case points in the y or $-y$ directions. It is important to note that this picture is a simplification. It's validity will be further discussed in the subsequent paragraphs and also in the results section. Presently however, the aligned phase is rotated by 90° so that the average platelet face orientation now is parallel with the yz-plane and the director $\vec{n}$ points along x or $-x$, parallel with the field $\vec{H}$. Reorientation back to the stable $\vec{n} \perp \vec{H}$ configuration can now proceed via four independent pathways, characterized by rotation either counterclockwise or clockwise around the z-axis, or the y-axis. Of course, combinations of these might also occur so that the stable state might consist of platelets that are tilted. All the stable states are however, characterized by $\vec{n} \perp \vec{H}$. The situation is illustrated in Figure 2.7, showing the stable vertical and a tilted stable orientation for a field pointing along x.

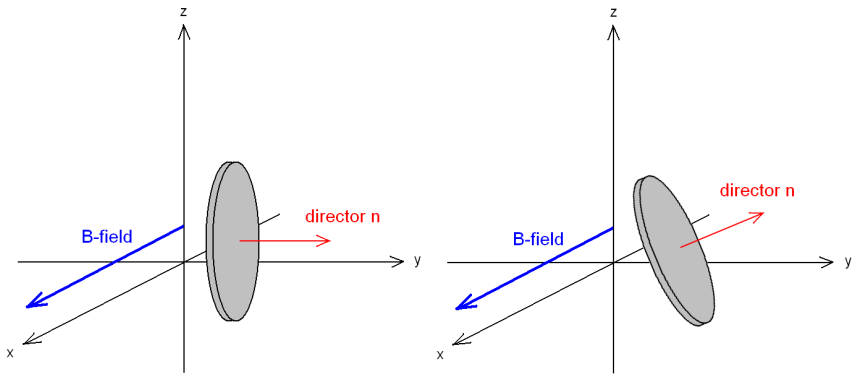

Figure 2.7: Two stable fluorohectorite platelet orientations in a magnetic field pointing along x. In both cases, the director or optical axis of the platelets are perpendicular to the field.

Blake et al. [4] have investigated the Fréedericksz transition for rod-like nematogens of positive $\Delta\chi$ from the point of view of bifurcation theory. In their study, parallel wall alignment between two opposing plates was

used to produce an overall oriented phase to which a magnetic field was applied perpendicularly or at a slight angle to the plates. In analogy to the present discussion, for sufficient field strengths the transition to the stable state could proceed via either counterclockwise or clockwise rotation of the nematogens. The bifurcation in the study by Blake et al. [4] thus occurred when the field strength became strong enough to produce realignment, as the original symmetry of the problem was broken and the system could proceed via two different pathways towards the realigned state.

It is apparent that there are some differences between a nematic fluorohectorite dispersion and the system studied by Blake et al. in [4]. Firstly, the diamagnetic susceptibility anisotropy $\Delta\chi$ for the rod-like nematogens of the Blake study was positive, leading to a stable state above the field threshold characterized by $\vec{n} \parallel \vec{H}$, whereas in a Na-fluorohectorite dispersion the stable state above the threshold is reached when $\vec{n} \perp \vec{H}$ because of the platelets' negative $\Delta\chi$. Furthermore it is seen that, in the case where the field was applied parallel to the aligning plates, Blake et al.'s system undergoes a so-called pitchfork bifurcation where the two possible pathways of counterclockwise or clockwise rotations are equally likely. In the standing nematic phase of Na-fluorohectorite platelets on the other hand, there are four possible pathways, of which rotations around the axes y or z introduced above, are not necessarily equally likely since, at least initially, the y rotation corresponds with a splay distortion combined with a bend distortion, relative to the initial director field, whereas the z rotation corresponds with a splay and twist distortion. For nematics that display large enough anisotropies in elasticity, it may be energetically favorable to combine different distortion modes [57]. This is known to cause periodic structures associated with the Fréedericksz transition.

The last and perhaps most fundamental difference between the Blake study and the currently discussed fluorohectorite system, pertains to the competing forces which produce the director field distortions in the two cases. In the study by Blake et al. the competing forces of alignment were the parallel wall anchoring imposed by the opposing plates and the response of the rod-like nematogens to the magnetic field. In the case of Na-fluorohectorite dispersions on the other hand, three different aligning forces feature. These are respectively the homeotropic wall alignment produced by wall interactions [10], as well as the preferred orientations imposed by the initial and final fields, which are at 90° to each other with respects to a coordinate system in which the sample capillary remains stationary. The Na-fluorohectorite system is thus the more complex both with respects to the possible reorientation pathways and with respects to their origin. Furthermore, the fact that the Na-fluorohectorite dispersions are contained in capillaries of circular morphologies, presents even the initial magnetically aligned phase with distorted boundaries.

Figure 2.8 shows a splayed and bent director field which can be imag-

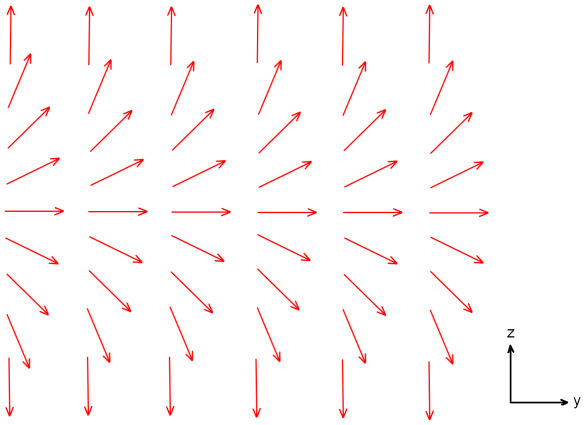

Figure 2.8: A splay and bend distorted director field. For a magnetic field pointing along x and into the page, all depicted orientations fullfill the $\vec{n} \perp \vec{H}$ requirement.

ined as a vertical cut through a Na-fluorohectorite capillary sample having the illustrated director field configurations, if the effects of the walls are neglected. All the orientations shown fullfill the magnetic stability requirement that each platelet's optical axis should be oriented perpendicular to a magnetic field pointing into the page. Assuming the field that now points into the page previously was pointing from the left to the right side of Figure 2.8, parallel with the image plane and the y-axis, the midsection of the illustrated director field shows a local director configuration which could have arisen from a platelet rotation around z; correspondingly the top and bottom sections show director configurations that could originate from rotations around y. Since the Frank elasticity constants for the nematic phase of aqueous fluorohectorite dispersions are not known, any true predictions concerning the effects of subjecting a Na-fluorohectorite capillary sample to magnetic forces cannot be made at present. As mentioned, it is however known that in general the Frank moduli for disc-like nematogens obey the relation that $K_{22} \geq K_{11} > K_{33}$ [80, 67]. If this is valid also for fluorohectorite platelets, then it is seen that the earlier discussed rotation around the y-axis, corresponding to a distortion with respects to the presumed initial director field involving the splay and bend constants K_{11} and K_{33}, contributes a smaller addition to the free energy than the rotation around z, that involves K_{11} and K_{22}. Since free energy minimization is a general principle, used for determining the pathways a system follows, it is seen that the reorientation towards the stable state is more likely to proceed via rotations around the y-axis.

The thread started in the current section will be picked up in section 4.4,

where optical birefringence observations and x-ray scattering data from a Na-fluorohectorite dispersion subjected to magnetic fields are presented. It is also worth mentioning that measurements of the field strengths required for inducing a Fréedericksz transition in initially aligned nematics can be used to determine the relationship between the Frank constants and the strength of the wall anchoring [36, 57]. This does however require an experimental setup which assures that only known distortion modes contribute; since this is far from true, at least initially, in the case of the fluorohectorite dispersions investigated in the current project, such quantitative values can not be obtained in the present discussion.

2.3.3 Light propagation in a liquid crystalline colloid

As discussed in section 2.3.2, a nematic phase is per definition anisotropic both with regards to the shape of the nematogens as well as with respect to their orientational distribution. The behavior of electromagnetic waves traversing such anisotropic phases differs from the behavior of waves propagating in isotropic media. This feature is extensively used in optical investigations of liquid crystals. The current section will thus address the theme of light propagation in anisotropic media, starting with a very brief introduction to electromagnetic waves[12]. A general background for this section can be found in Appendix A, which deals with the basics of classical, Maxwellian electromagnetism.

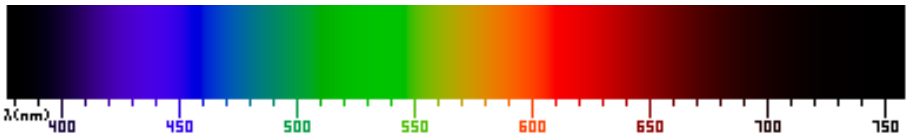

Figure 2.9: The visible spectrum of electromagnetic waves.

Electromagnetic waves are characterized by their wavelength, their electric and magnetic field amplitudes and the plane in which the electrical field amplitude oscillates at any given instance. Perfect linearly polarized light has one specific plane in which the electrical field amplitude oscillates, where the direction of polarization corresponds with the direction of oscillation of the electric field. Circularly polarized light on the other hand can be thought of as a superposition of two linearly polarized waves oscillating with equal amplitudes at right angles to each other, but with a relative phase shift of $\pi/2$ radians. If the electrical field amplitudes of the two linearly polarized waves are unequal or the phase shift is different from $\pi/2$, the light

[12]The current section mainly deals with light as electromagnetic waves, whereas in section 2.4 on x-ray scattering, electromagnetic radiation is considered also from the quantum mechanical perspective.

resulting from their combination is elliptically polarized. Humans are not in general able to distinguish polarized from non-polarized light. This is however a truth with modifications, as an optical effect in the human eye known as Haidinger's brushes causes the central field of vision to appear as a diffuse cross of yellow and blue lobes when the incident light is linearly polarized [5][13]. The visible spectrum for human beings spans a small region of wavelengths ranging from around 400 nm to 700 nmeter [7], see Figure 2.9.

Light in anisotropic media

Light propagation in an anisotropic medium differs from propagation in an isotropic medium. Figure 2.10 illustrates the changes occurring when going from a dielectrically isotropic to a dielectrically anisotropic medium. The electric flux density $\vec{D}$ in the anisotropic case now oscillates at an angle with the electric field $\vec{E}$ [36], and thus the direction of propagation $\vec{k} \propto \vec{D} \times \vec{H}$ of the wave phase no longer coincides with the direction of energy transfer, defined through the Poynting vector $\vec{S} = \vec{E} \times \vec{H}$.

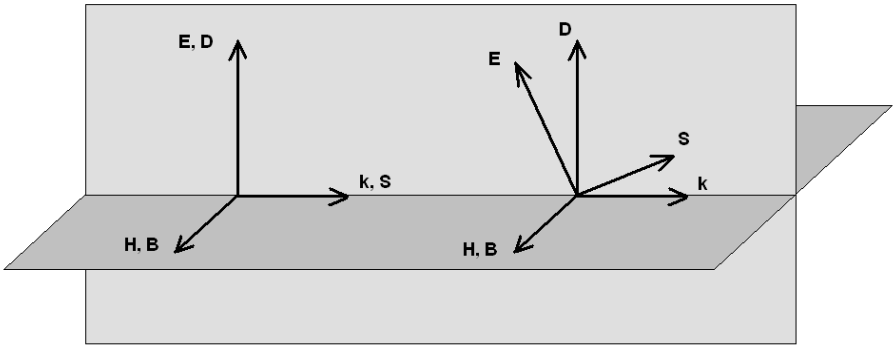

Figure 2.10: Light propagation in a dielectrically isotropic medium (left) and in a dielectrically anisotropic medium (right).

As is the case for isotropic media, the relation between the velocity c of light in vacuum and the phase velocity v of light in a linear, anisotropic medium is given by the expression $N = c/v$, where N is the medium's effective refractive index. In uniaxial anisotropic media the electric permittivity tensor has two independent components $\epsilon_{\|}$ and $\epsilon_{\perp}$ [36, 62], denoting respectively the dielectric permittivity for fields oscillating along the director $\vec{n}$ or

[13]Interestingly, this effect is quite easily observed if a polarizer plate is held up towards white and bright skies. The direction of the yellow lobes observed is perpendicular with the polarization of the electrical field. The brushes are also relatively easy too see in a white page displayed on an LCD screen that emits plane polarized light.

perpendicular to it. In this case the Fresnel equation, known from optical theory, takes the following simplified form [36]:

$$\left(N^2 - \epsilon_\perp\right)\left(\epsilon_\parallel N_z^2 + \epsilon_\perp\left(N_x^2 + N_y^2\right) - \epsilon_\parallel\epsilon_\perp\right) = 0 \tag{2.63}$$

Here z is chosen to lie along the uniaxial medium's director $\vec{n}$. N_z denotes the absolute value of the z-component of $\vec{N}$, and N_x and N_y the same values along the x- and y-directions of a cartesian coordinate system. This equation has two solutions, obtained by setting either the first or second factor to zero;

$$1 = \frac{N^2}{\epsilon_\perp} \tag{2.64}$$

$$1 = \frac{N_z^2}{\epsilon_\perp} + \frac{N_x^2 + N_y^2}{\epsilon_\parallel} \tag{2.65}$$

These two solutions define respectively a sphere and an oblate or prolate ellipsoid that intersect at $N_x = N_y = 0$ and $N_z = \pm\sqrt{\epsilon_\perp}$. The uniaxial medium's optical axis is defined as the vector between these two points [36, 62], which for conventional nematics on average corresponds with the director $\vec{n}$.

From this discussion, it becomes apparent that two special directions of propagation can be distinguished in a uniaxial material. The ordinary wave, propagating with a wave vector $\vec{k}$ oriented along the uniaxial director $\vec{n}$ will experience an index of refraction $n_\perp = \sqrt{\epsilon_\perp}$. The so-called extraordinary wave on the other hand propagates with $\vec{k}$ oriented at an angle θ relative to the director $\vec{n}$. Noting that $N_z^2 = N^2\cos^2\theta$ and that $N_x^2 + N_y^2 = N^2\sin^2\theta$ [14], the ellipsoidal solution of Equation 2.63 can be written as:

$$1 = \frac{N^2\cos^2\theta}{\epsilon_\perp} + \frac{N^2\sin^2\theta}{\epsilon_\parallel} \tag{2.66}$$

Rearranging this expression yields the following solution for the refractive index as a function of the angle θ:

$$N(\theta) = \frac{n_\parallel n_\perp}{\sqrt{n_\parallel^2\cos^2\theta + n_\perp^2\sin^2\theta}} \tag{2.67}$$

[14] A general cartesian coordinate (x, y, z) can be written in spherical coordinates as $(r\cos\phi\sin\theta, r\sin\phi\sin\theta, r\cos\theta)$. Based on this, the refractive index component along z is given as $N_z = N\cos\theta$. Furthermore, the expression $N_x^2 + N_y^2$ can be written as:

$$\begin{aligned} N_x^2 + N_y^2 &= N^2\cos^2\phi\sin^2\theta + N^2\sin^2\phi\sin^2\theta \\ &= N^2\sin^2\theta\left(\cos^2\phi + \sin^2\phi\right) \\ &= N^2\sin^2\theta \end{aligned}$$

Propagation along the director so that $\theta = 0°$ retrieves the previous result that $N(0°) = n_\perp$. Propagation perpendicular to the director so that $\theta = 90°$ yields $N(90°) = n_\parallel$. Disc-like nematogens, such as clay platelets, usually form an optically negative nematic phase characterized by an extraordinary index of refraction $n_\parallel$ that is smaller than the ordinary index of refraction $n_\perp$ [36], so that $\Delta n = n_\parallel - n_\perp < 0$. It the present discussion, effects that might arise due to the discrete nature of the anisotropic phase (i.e. the clay platelets) are not considered.

Optical observations between crossed polarizers

The observation of a liquid crystalline sample between crossed polarizers is an important and relatively straightforward investigation technique that is widely employed. The following discussion illustrates what happens when incoming white, unpolarized light passes through a crossed polarizer setup with a nematic phase inserted between the polarizer plates. Consider a cartesian coordinate system in which a polarizer is placed at $y = a$ parallel with the xz-plane and with its axis oriented along the z-direction. When incident light propagating in the y-direction strikes this polarizer, per definition only the component polarized along z will be transmitted. This linearly polarized light then travels through a nematic phase of uniform director orientation $\vec{n}$ placed between $y = b$ and $y = c$. This light can be decomposed into two components, one polarized parallel with and one perpendicular to $\vec{n}$, traveling respectively with phase velocities $v_\parallel = c/n_\parallel$ and $v_\perp = c/n_\perp$. Because these velocities are different, the two components will get out of phase and the combined light, whose polarization is determined by the phase difference between the two components, thus becomes in general elliptically polarized. A second polarizer, commonly known as the analyzer, is placed parallel with the xz-plane on the opposite side of the nematic phase at $y = d$. This analyzer has its axis parallel with the x-direction. As the elliptically polarized light emerging from the nematic phase strikes the analyzer, the component polarized along x will be transmitted. If the nematic phase had not been present, the light transmitted by the first polarizer would have been extinguished by the analyzer.

The intensity I of the light emerging from a setup of crossed polarizers can be written as [62]:

$$I = \frac{I_0}{2} \sin^2 [2\alpha] \sin^2 [\pi \Delta n (\lambda) \, l/\lambda] \tag{2.68}$$

Here I_0 is the initial intensity, α the angle the director $\vec{n}$ makes with the polarizer axis, $\Delta n = n_\parallel - n_\perp$ the effective birefringence, λ the wavelength of the light and l the thickness of the sample along the ordinary beam path. The product $\Delta n l$ is commonly referred to as the retardation. This equation is valid when the wavevector $\vec{k}$ of the incident light is perpendicular to the

director $\vec{n}$. A slightly more complicated expression based on the deduced index of refraction of Equation 2.67 is valid in the general case, where θ denotes the angle between the the wavevector $\vec{k}$ of the incident light and the director $\vec{n}$:

$$I = \frac{I_0}{2}\sin^2\left[2\alpha\right]\sin^2\left[\frac{\pi l}{\lambda}\left(\frac{n_{\parallel}(\lambda)n_{\perp}(\lambda)}{\sqrt{n_{\parallel}(\lambda)^2\cos^2\theta + n_{\perp}(\lambda)^2\sin^2\theta}} - n_{\perp}(\lambda)\right)\right] \quad (2.69)$$

Dividing Equation 2.68 by I_0 yields an expression for the relative transmission:

$$T = \frac{1}{2}\sin^2\left[2\alpha\right]\sin^2\left[\pi\Delta n\left(\lambda\right)l/\lambda\right] \quad (2.70)$$

For a given retardation Δnl, maximum transmission is achieved when $\sin^2\left[2\alpha\right] = 1$ so that $\alpha = \pi/4 + N\pi/2$ where $N = 0, \pm1, \pm2...$, whereas extinction (zero transmission) occurs when $\sin^2\left[2\alpha\right] = 0$, i.e. when $\alpha = N\pi/2$. A liquid crystal thus appears dark between crossed polarizers when the director is oriented parallel with either the polarizer or analyzer axis, or perpendicular to both – the latter case being valid from considerations of Equation 2.69. In the opposite case, a liquid crystal appears brightest when the director lies in the plane of the crossed polarizers at an angle of 45° with the polarizer axes. For a given α, the transmission is at maximum when $\sin^2\left[\pi\Delta n\left(\lambda\right)l/\lambda\right] = 1$ so that the retardation $\Delta nl = \left(1/2 + N\right)\lambda$. Extinction occurs when this expression equates to zero, i.e. when $\Delta nl = N\lambda$. It is apparent from Equation 2.70 that the relative transmission for different wavelengths (i.e. different colors) is dependent on the retardation. A plot of the relative transmission as a function of light wavelength for four different retardations can be found in Figure 2.11.

For small retardations, no visible wavelengths are extinct or close to extinct, and the transmitted light from the uniaxial material between crossed polarizers appears white or neutrally gray [62]. As the retardation increases, the first extinct wavelength will be in the short wavelength range of the visible spectrum, corresponding to violet and blue colors. The transmitted intensity will therefore be a combination of red, yellow and green. For larger retardations, the low wavelengths will again be strongly transmitted while the longer wavelengths go extinct. Figure 2.12 shows a so-called Michel-Lévy chart which displays the expected color of the transmitted light as a function of the retardation.

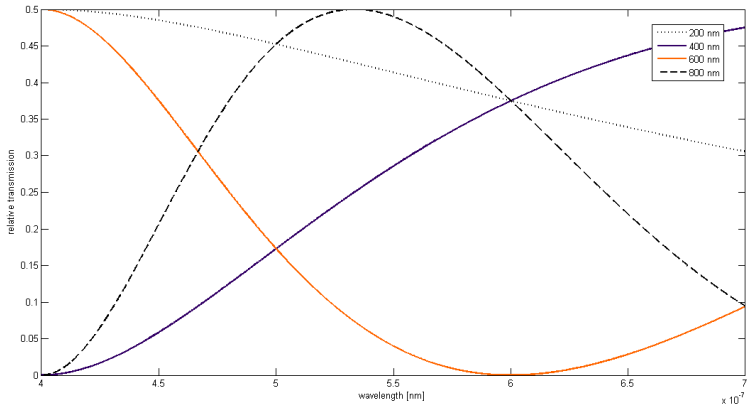

Figure 2.11: Plot of the relative transmitted intensity I/I_0 of Equation 2.70 as a function of wavelength for retardations Δnl of respectively 200 nm, 400 nm, 600 nm and 800 nm, for $\alpha = 45°$.

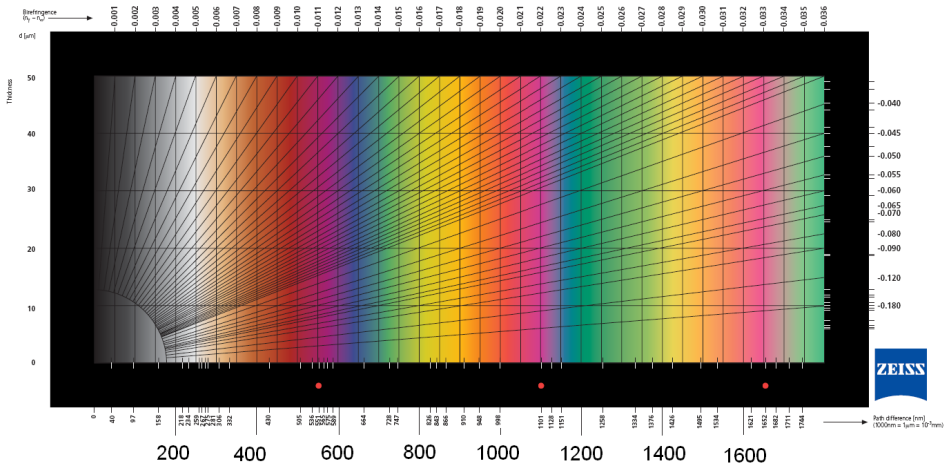

Figure 2.12: Michel-Lévy chart, retrieved from a Carl Zeiss information brochure at [51]. The topmost axis lists values of the birefringence Δn and the left axis the sample thickness l in µm. The bottom axis gives values of the retardation Δnl corresponding with the displayed colors, in nm. The three red dots show the positions (left to right) or respectively 1st, 2nd and 3rd order magneta.

2.4 X-ray scattering

Scattering techniques are today an integral part of the natural sciences which deal with the structure of matter on the length scales of atoms and molecules. There are three types of radiation used in modern scattering facilities. These comprise scattering of neutrons, of electrons or of photons, also known as electromagnetic waves. In essence a scattering experiment is designed to probe the structure of matter by recording the radiation transmitted or reflected from the material. The spatial intensity profile of the scattered radiation will be dependent on the material structure, or more specifically, on the interaction potential distribution of the material as seen by the incident radiation. For a given material, the potential seen will be dependent upon the type of radiation. Neutrons interact with matter mainly via nuclear forces and hence sees the scattering potential of the material's neutrons and protons, comprising the very small atomic cores. Electrons interact with matter via the electromagnetic force and thus experience the potential set up by the material's charges, i.e. it's electrons and protons. When electromagnetic radiation hits a material it can undergo a series of different interactions that are critically dependent upon the radiation energy. Electromagnetic radiation falling within the x-ray spectrum is used for structural analyses. The next sections will thus in more detail address the specifics of x-ray scattering, first from a fundamental viewpoint and then within the context of modern materials science.

Some central concepts of scattering theory are however common for all types of radiation. Two of these basic concepts are the scattering cross section, usually denoted as σ, and the related differential scattering cross section $d\sigma/d\Omega$ which defines the amount of radiation scattered into the solid angle element $d\Omega$ per unit time. The defining expression for the differential scattering cross section can be written as [2]:

$$\frac{d\sigma}{d\Omega} = \frac{I_{s,\Delta\Omega}}{I_0 N \Delta\Omega} \tag{2.71}$$

Here $I_{s,\Delta\Omega}$ is the number of radiation quanta scattered into a solid angle $\Delta\Omega$ per second, I_0 the number of radiation quanta incident on the illuminated sample area per second, and N the number of scatterers in the illuminated sample volume. The differential scattering cross section is thus a measure of how strongly a given scatterer in a sample scatters incident radiation into the solid angle element $d\Omega$.

2.4.1 The interaction of x-rays with matter

As already mentioned, x-rays are commonly used for structural studies. X-rays are a type of electromagnetic radiation characterized by having a wavelength roughly on the order of 1 Å [2]. It is common practice to consider x-

rays, as well as all other parts of the electromagnetic spectrum, as both classical electromagnetic waves and quantum mechanical photons. Each quantum mechanical photon is described as having an energy $E = h\nu = \hbar\omega = \hbar ck$ where h is Planck's constant, $\hbar$ it's reduced version, ν and ω the photon's spatial and radial frequencies, respectively, and k the length of the wavevector $\vec{k}$. The photon momentum is given as $\vec{p} = \hbar\vec{k}$. The so-called photon wavelength λ, which corresponds with the classical wavelength within Maxwellian electromagnetism, is related to the wavenumber k via the relation $\lambda = 2\pi/k$. In the classical picture, the equation for the electric field of a plane electromagnetic wave, $E(\vec{r}, t) = E_0 \exp\left[i\vec{k}\cdot\vec{r} - i\omega t\right]\vec{o}$, incorporates the same quantities which are used to characterize the quantum mechanical photon.

X-ray scattering on free electrons and the Thomson cross section

The primary interaction of x-rays with matter takes place on the material's electrons [2]. Classicly this interaction is described via the ability of the electrical radiation field to induce an oscillatory motion of the material's electrons. Because an oscillating electron is an electrical charge which continuously accelerates and de-accelerates, such an electron will emit electromagnetic radiation.

Quantum mechanically, scattering as well as photon absorption are described via perturbation theory. In Appendix B the differential Thomson scattering cross section is derived for the interaction of a photon of wavevector $\vec{k}$ and polarization $\vec{o}$ with a free electron initially at rest. It is required that the photon energies involved are much smaller than the rest mass energy of the electron, $\hbar kc \ll m_e c^2$ where $\hbar kc$ is the photon energy, so that the system can be treated non-relativisticly. The contribution to the Hamiltonian of the combined system quadratic in the vector potential $\vec{A}$ serves to annihilate the initial photon, while the scattered photon of wavevector $\vec{k}'$ and polarization $\vec{o}'$ is created and the electron receives momentum. However, it is seen that the non-relativistic treatment leads to an approximation which dictates the scattering to be elastic. It is possible to choose the two independent polarizations of the photons so that these are oriented either parallel with or perpendicular to the scattering plane containing $\vec{k}$ and $\vec{k}'$, but with the parallel polarization of the final photon making an angle θ with the parallel polarization of the initial photon. The differential scattering cross section for photon-electron interactions leading to a scattered photon detectable within the solid angle element $d\Omega$, is found to be dependent upon the polarization of the incoming photon. For an incoming photon that with certainty was polarized in the scattering plane, the differential scattering cross section is $d\sigma/d\Omega_{\parallel}$, whereas for an initial photon polarized perpendicular to the plane, the differential scattering cross section is $d\sigma/d\Omega_{\perp}$. From the discussion of Appendix B, these two differential cross

sections are expressed as:

$$\frac{d\sigma}{d\Omega_{\parallel}} = r_0^2 \cos^2\theta \tag{2.72}$$

$$\frac{d\sigma}{d\Omega_{\perp}} = r_0^2 \tag{2.73}$$

Here $r_0 = e^2/4\pi\epsilon_0 m_e c^2 = 2.818$ fm is the Thomson scattering length, that represents the distance for which the Coulomb energy between two electrons equals the electron rest mass energy. Now, the unpolarized differential Thomson cross section is the weighted sum of the polarized contributions:

$$\frac{d\sigma}{d\Omega} = \frac{1}{2} r_0^2 \left(1 + \cos^2\theta\right) \tag{2.74}$$

The total scattering cross section is found through multiplying Equation 2.74 by the solid angle element $d\Omega$ and integrating:

$$\sigma = \frac{8\pi}{3} r_0^2 = 665 \text{ mb} \tag{2.75}$$

This scattering cross section, as well as the differential cross sections, are energy independent. A more sophisticated treatment, taking into account relativistic effects, results in the so-called differential Klein-Nishina cross section:

$$\frac{d\sigma}{d\Omega} = \frac{1}{2} r_0^2 \left(f\left(\hbar kc, \theta\right) - f\left(\hbar kc, \theta\right)^2 \sin^2\theta + f\left(\hbar kc, \theta\right)^3\right) \tag{2.76}$$

Here the quantity $f\left(\hbar kc, \theta\right)$ is given as:

$$f(\hbar kc, \theta) = \frac{1}{1 + \left(\left(\hbar kc / m_e c^2\right)\left(1 - \cos\theta\right)\right)} \tag{2.77}$$

In the non-relativistic limit where $\hbar kc \ll m_e c^2$, $f\left(\hbar kc, \theta\right) \approx 1$, and the result of Equation 2.74 is retrieved because $1 - \sin^2\theta + 1 = 1 + \cos^2\theta$. Because the rest mass energy of an electron is $m_e c^2 = 511$ keV, whereas the energy of a typical x-ray photon of wavelength 1 Å is $\hbar kc = 12.4$ keV, the non-relativistic expressions of equations 2.74 and 2.75 are valid for x-ray scattering, which thus can be considered elastic.

Momentum transfer and the scattering vector

A much used quantity within the field of scattering theory and experiment, is the so-called scattering vector $\vec{q}$, and it's length q. It is derived by considering the relation for momentum transfer in a scattering event, which writes out as:

$$\hbar\vec{k}' + \hbar\vec{q} = \hbar\vec{k} \tag{2.78}$$

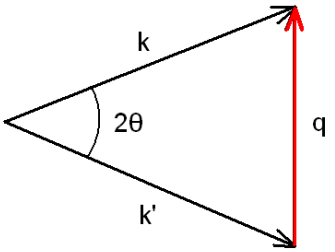

Figure 2.13: Momentum transfer in a scattering event.

The situation is illustrated in Figure 2.13. Now, since the scattering is elastic, $k' = k$, and the length of the scattering vector $\vec{q}$ is by geometrical considerations given by:

$$\sin\theta = \frac{q/2}{k} \tag{2.79}$$

Since $k = 2\pi/\lambda$, this can be re-written in terms of the photon wavelength λ, yielding the following commonly encountered expression for the length of the scattering vector:

$$q = \frac{4\pi \sin\theta}{\lambda} \tag{2.80}$$

Now there seems to be a discrepancy between this momentum transfer and the fact that the scattering is elastic. This discrepancy arises because the electron was initially at rest. Any change in momentum direction for an electron initially at rest implies a gain in kinetic energy, incompatible with elastic photon scattering. If the electron initially was not at rest, this would not be a problem. However, recall that the elastic scattering limit arose out of an approximation, that was based on the electron rest mass $m_e c^2$ being much larger than the initial photon energy $\hbar kc$. Within this approximation, the momentum transferred to the electron would result in a kinetic energy increase negligible with respects to other energies involved.

Photoelectric absorption

In addition to photon scattering, two other processes are generally distinguished as interaction mechanisms between an electron and the electromagnetic radiation field [40]. These two interactions are called pair production and photoelectric absorption. Pair production involves the annihilation of the incident photon in the vicinity of a heavy body such as an atom, along with the creation of an electron-positron pair [40]. But because the rest mass energy of the electron-positron pair is $2 \cdot 511$ keV $= 1.022$ MeV, the incident photon needs to be at least this energetic for pair production to occur, in order not to violate energy conservation. A 1.022 MeV photon

has a wavelength of $1.022\,\mathrm{MeV}/hc = 0.01213\,\text{Å}$, which is much smaller than the wavelengths of around 1 Å encountered in x-ray experiments. Pair production is therefore irrelevant for the present discussion. Photoelectric absorption on the other hand, is the dominant interaction of relatively low energy photons with matter. In this interaction process, the initial photon is annihilated and it's energy transferred to an atomic electron which thus is excited into a continuum state [40]. The resulting hole in the electron's original orbital can be filled either when an electron from a higher orbital falls down into the hole or when the atom de-excites by emitting a so-called Auger electron. In the former case, the energy difference between the higher orbital and the hole state is emitted in the form of a photon.

Because several electron binding energies are in the x-ray range, photoelectric absorption is an important factor in the field of x-ray science [2]. This process cannot be explained classically, so a quantum mechanical treatment is required in order to arrive at the photoelectric absorption cross section. In analogy to the scattering treatment of Appendix B, the photoelectric absorption cross section is calculated from time-dependent perturbation theory. The contribution to the Hamiltonian of the combined system linear in the vector potential $\vec{A}$ serves to annihilate the initial photon, while the electron is transferred from it's orbital state into a final continuum state. This final electron state can be approximated as a free particle state when the electron's kinetic energy is high enough, whereas when the kinetic electron energy is lower, the potential energy term arising from the Coulomb interaction between the electron and the emitting atom must also be taken into account [32].

The differential cross section for photoelectric absorption of a photon of energy $\hbar\omega$ on the 1s electron orbital, also known as the K-shell, according to [32] can be expressed as:

$$\frac{d\sigma}{d\Omega} = \sqrt{32}\alpha^4 Z^5 r_0^2 \left(\frac{m_e c^2}{\hbar\omega}\right)^{7/2} \sin^2\theta \cos^2\phi \left(1 + \frac{v}{c}\cos\theta\right) \tag{2.81}$$

Here $\alpha = e^2/4\pi\epsilon_0\hbar c \approx 1/137$ is the fine structure constant, θ the angle between the initial photon wavevector $\vec{k}$ and the momentum $\vec{p}$ of the freed electron, and ϕ the angle between $\vec{p}$ and the polarization vector of the incoming photon. The expression of Equation 2.81 was deduced non-relativisticly, and is valid when the binding energy of the orbital electron is much smaller than the other energies involved. The total cross section is found by integrating over the solid angle element $d\Omega$:

$$\sigma = \frac{16\sqrt{2}\pi}{3}\alpha^4 Z^5 r_0^2 \left(\frac{m_e c^2}{\hbar\omega}\right)^{7/2} \tag{2.82}$$

It is seen that according to this treatment, the cross section for photoelectric absorption is proportional to $Z^5\,(\hbar\omega)^{-7/2}$, where Z is the number of protons

in the core of the ejecting atom. However, Lilley [40] reports this proportionality factor for the absorption of photons of a few hundred keV, an energy range which is substantially higher than the energy of around 10 keV often encountered in x-ray scattering experiments. In the x-ray range, the proportionality according to Als-Nielsen and McMorrow [2] is more closely described by a factor $Z^4 (\hbar\omega)^{-3}$. The difference is caused by the inclusion in the derivation of the latter proportionality factor of the Coulomb potential between the electron and the atom it escapes from.

Due to effects such as shielding of the core potential by the inner orbitals, tabulated values of the photoelectric absorption cross section should be used in experimental studies [2]. In scattering experiments, photoelectric absorption is a limiting factor which serves to removes flux from the beam. In the field of x-ray imaging on the other hand, it is the contrast in absorption cross section for different Z, i.e. different elements, as well as the tunable penetration depth, which renders this technique immensely useful.

2.4.2 Kinematical scattering theory

As a beam of x-rays hits a sample, flux is removed from the incident direction by two processes. These are the scattering and absorption interactions described in the previous section. Within kinematical scattering theory, the possibility that a photon created in a scattering event might itself undergo further scattering interactions is neglected. For this approximation to be valid the scattering must in some sense be weak.

Within the Born approximation, valid in this limit, it is found that the scattering amplitude $F(\vec{q})$ for x-rays incident on a material sample is proportional to the Fourier transform of the material's real space electron density distribution $\rho(\vec{r})$ [61, 2]:

$$F(\vec{q}) = \int \rho(\vec{r}) \exp[i\vec{q}\cdot\vec{r}]\, d^3r = \mathcal{F}[\rho(\vec{r})] \tag{2.83}$$

The differential scattering cross section $d\sigma/d\Omega$ is proportional to the absolute square of the scattering amplitude [32]:

$$\frac{d\sigma}{d\Omega} \propto |F(\vec{q})|^2 \tag{2.84}$$

Now, the observable intensity $I(\theta, \phi)$ of the scattered radiation is proportional to the differential cross section $d\sigma/d\Omega$. It is therefore the absolute square of the Fourier transform of $\rho(\vec{r})$ which is directly measured in a scattering experiment. Transforming $|F(\vec{q})|^2$ back into real space yields the

so-called correlation function $P(\vec{r})$ [61]:

$$\begin{aligned} P(\vec{r}) &= \mathcal{F}^{-1}\left[|F(\vec{q})|^2\right] \\ &= \mathcal{F}^{-1}\left[F^*(\vec{q}) \cdot F(\vec{q})\right] \\ &= \mathcal{F}^{-1}\left[F^*(\vec{q})\right](*)\,\mathcal{F}^{-1}\left[F(\vec{q})\right] \\ &= \rho(-\vec{r})(*)\,\rho(\vec{r}) \end{aligned} \tag{2.85}$$

The second line was arrived at by writing the absolute square $|F(\vec{q})|^2$ of the scattering amplitude as the product of $F(\vec{q})$ with it's complex conjugate $F^*(\vec{q})$, factored in from the left. The transition to the second last line makes use of the fact that the Fourier transform of the convolution of two functions g and h equals the product of their respective stand-alone Fourier transforms:

$$\mathcal{F}[g(*)h] = \mathcal{F}[g]\,\mathcal{F}[h] \tag{2.86}$$

This identity is of fundamental importance within the field of scattering theory. It allows the total distribution $\rho(\vec{r})$ of scattering ability of a material to be written as a convolution of simpler functions, whose Fourier transforms are much easier to find than the Fourier transform of $\rho(\vec{r})$ taken as a whole.

The splitting of $\rho(\vec{r})$ into a convolution of simpler functions

The current section considers how the scattering amplitude $F(\vec{q})$ can be written as a product of a set of Fourier transformed functions whose convolution in real space equals the total distribution $\rho(\vec{r})$ of electrons of the material considered. Now, as discussed, the most basic scattering elements of a material are the electrons, whose total distribution within the material is written as $\rho(\vec{r})$. The time dependence of this distribution is neglected in the current discussion[15]. Since a material does consist of spatial units larger than electrons, such as atoms and molecules, $\rho(\vec{r})$ can be split into the convolution of at least two functions, those being the distribution of electrons within an atom, and the distribution of atoms within the material. For spatially periodic structures, the latter can be further broken down into a convolution of functions that reflect respectively the arrangements of atoms within the so-called unit cell, and the arrangement of unit cells throughout the material. The concept of the unit cell is explained in a later section. Presently, the Fourier transform of the real space distribution of electrons within an atom will be considered. This function is known as the atomic form factor.

[15]The main purpose of the current section is to illustrate how the scattered intensity from a structured material can be successively built up by considering the spatially repeating features of $\rho(\vec{r})$. The time-dependent features of the electron distribution, leading to for instance the inclusion of the Debye-Waller factor in the expression for the scattered intensity, are not treated because the results and discussions section will never attempt to extract information from the exact values of the measured intensities; only their relative variations for different q will be treated.

The atomic form factor

Quantum mechanically, an atom is an object that consists of a very small core of Z protons and N neutrons, surrounded by Z orbiting electrons occupying bound states that can be characterized by wavefunctions $\psi_n(\vec{r})$. According to the Copenhagen interpretation of quantum mechanics, which is widely accepted, the absolute square $|\psi_n(\vec{r})|^2$ of the wavefunction yields the spatial probability distribution for the position of the electron [32]. For a many-electron system, the electron density distribution is a function of the contribution from each occupied orbital. If for a given atom the total electron density from all the occupied orbitals is written as a function $\Psi(\vec{r})$, then the atomic form factor for this atom can be expressed as:

$$f = \int |\Psi(\vec{r})|^2 \exp[i\vec{q}\cdot\vec{r}]\, d^3r \tag{2.87}$$

Values of the atomic form factor for the different elements are tabulated in the International Tables of Crystallography.

The unit cell structure factor and the interference function

Structurally periodic materials are characterized by possessing translational symmetries. For a three-dimensional lattice, the lattice positions in real space are denoted via the vector $\vec{R}_{uvw}$ as a sum over the lattice vectors $\vec{a}$, $\vec{b}$ and $\vec{c}$ multiplied by a set of scalars u, v and w:

$$\vec{R}_{uvw} = u\vec{a} + v\vec{b} + w\vec{c} \tag{2.88}$$

These scalars are integers, so that the possible values of $\vec{R}_{uvw}$ are a sum over integer multiples of the lattice vectors. There are seven possible sets of lattice vectors which are compatible with the space filling requirement of a three dimensional lattice. These are listed in Table 2.4.

Any three dimensional crystalline material belongs to one of the seven crystal systems. It's structure is arrived at by adding a so-called basis to each lattice site $\vec{R}_{uvw}$. The basis consists of j atoms, whose positions with respects to the lattice point $\vec{R}_{uvw}$ are described by the vectors $\sum_j \vec{r}_j$. The positions of all the atoms in a three-dimensional crystalline material are thus given by:

$$\sum_{uvw}\left(\vec{R}_{uvw} + \sum_j \vec{r}_j\right) = \sum_{uvw}\sum_j \left(\vec{R}_{uvw} + \vec{r}_j\right) \tag{2.89}$$

Now, the electron density distribution of a material can be written as a convolution between the density of electrons in an atom, the positions of these atoms in the basis, and the positions of the lattice sites:

$$\rho(\vec{r}) = \sum_j \left(|\Psi(\vec{r})|^2 (*)\, \delta(\vec{r} - \vec{r}_j)\right)(*) \sum_{uvw}\left(\delta\left(\vec{r} - \vec{R}_{uvw}\right)\right) \tag{2.90}$$

Table 2.4: The seven crystal systems compatible with three-dimensional translations in real space.

crystal system	length relations	angular relations
triclinic	$a \neq b \neq c$	$\alpha \neq \beta \neq \gamma$
monoclinic	$a \neq b \neq c$	$\alpha = \beta \neq \gamma$
orthorhombic	$a \neq b \neq c$	$\alpha = \beta = \gamma = 90°$
tetragonal	$a = b \neq c$	$\alpha = \beta = \gamma = 90°$
trigonal	$a = b \neq c$	$\alpha = \beta = 90°$, $\gamma = 120°$
	$a = b = c$	$90° \neq \alpha = \beta = \gamma \neq 120°$
hexagonal	$a = b \neq c$	$\alpha = \beta = 90°$, $\gamma = 120°$
cubic	$a = b = c$	$\alpha = \beta = \gamma = 90°$

The Fourier transform of this yields the scattering amplitude:

$$F(\vec{q}) = \left(\sum_j f_j \mathcal{F}\left[\delta\left(\vec{r} - \vec{r}_j\right)\right] \right) \cdot \left(\sum_{uvw} \mathcal{F}\left[\delta\left(\vec{r} - \vec{R}_{uvw}\right)\right] \right) \tag{2.91}$$

The first factor of this expression is known as the unit cell structure factor $F_{hkl}(\vec{q})$, or simply the structure factor. It reflects the distribution of atoms in the basis which each lattice site is decorated with. The second factor is the so-called interference function $S(\vec{q})$, which introduces the structural periodicity. The hkl index of the unit cell structure factor will be explained in the following. First the explicit expressions for the transforms of Equation 2.91 can be written out. The structure factor can be expressed as follows:

$$\begin{aligned} F_{hkl}(\vec{q}) &= \sum_j f_j \mathcal{F}\left[\delta\left(\vec{r} - \vec{r}_j\right)\right] \\ &= \sum_j f_j \int \delta\left(\vec{r} - \vec{r}_j\right) \exp\left[i\vec{q}\cdot\vec{r}\right] d^3r \\ &= \sum_j f_j \exp\left[i\vec{q}\cdot\vec{r}_j\right] \end{aligned} \tag{2.92}$$

The interference function is slightly more complicated. By performing the Fourier transform incorporated in the last factor of Equation 2.91, it is

initially given by:

$$\begin{aligned} S\left(\vec{q}\right) &= \sum_{uvw} \mathcal{F}\left[\delta\left(\vec{r}-\vec{R}_{uvw}\right)\right] \\ &= \sum_{uvw} \int \delta\left(\vec{r}-\vec{R}_{uvw}\right) \exp\left[i\vec{q}\cdot\vec{r}\right] d^3r \\ &= \sum_{uvw} \exp\left[i\vec{q}\cdot\vec{R}_{uvw}\right] \end{aligned} \tag{2.93}$$

Now for uvw large, this sum is found to be finite only when $\vec{q}\cdot\vec{R}_{uvw}$ equals integer multiples of 2π [61]. This is the Laue condition for diffraction. All $\vec{q}$ fulfilling this requirement are given by the so-called reciprocal lattice vector $\vec{G}_{hkl}$ which, just as $\vec{R}_{uvw}$ represents all real space lattice points, represents all lattice points in reciprocal space. The expression for this vector writes out as:

$$G_{hkl} = h\vec{a}^* + k\vec{b}^* + l\vec{c}^* \tag{2.94}$$

Here $\vec{a}^*$, $\vec{b}^*$ and $\vec{c}^*$ are the reciprocal space equivalents of the real space lattice vectors. The relationship between these two sets of vectors are given as [61]:

$$\vec{a}^* = 2\pi\left(\vec{b}\times\vec{c}\right) / \left(\vec{a}\cdot\left(\vec{b}\times\vec{c}\right)\right) \tag{2.95}$$

$$\vec{b}^* = 2\pi\left(\vec{c}\times\vec{a}\right) / \left(\vec{a}\cdot\left(\vec{b}\times\vec{c}\right)\right) \tag{2.96}$$

$$\vec{c}^* = 2\pi\left(\vec{a}\times\vec{b}\right) / \left(\vec{a}\cdot\left(\vec{b}\times\vec{c}\right)\right) \tag{2.97}$$

Now the product of $\vec{G}_{hkl}$ with $\vec{R}_{uvw}$ reads:

$$\begin{aligned} \vec{G}_{hkl}\cdot\vec{R}_{uvw} &= hu\left(\vec{a}\cdot\vec{a}^*\right) + kv\left(\vec{b}\cdot\vec{b}^*\right) + lw\left(\vec{c}\cdot\vec{c}^*\right) \\ &= 2\pi\left(hu+kv+lw\right) \end{aligned} \tag{2.98}$$

Now back to the interference function of Equation 2.93. In the case of an extended, three-dimensional crystalline structure so that the uvw integers go towards infinity (in reality, they are simply very large), the interference function can be written as [61]:

$$S\left(\vec{q}\right) = \frac{\left(2\pi\right)^3}{\vec{a}\cdot\left(\vec{b}\times\vec{c}\right)} \sum_{hkl} \left(\delta\left(\vec{q}-\vec{G}_{hkl}\right)\right) \tag{2.99}$$

The transition to the last line is based on the following general rule for Fourier transformation of a sum of delta functions, in the limit that $N\to\infty$ [61]:

$$\mathcal{F}\left[\sum_{u=1}^{N\to\infty} \delta\left(r-ua\right)\right] = \frac{2\pi}{a}\sum_h \delta\left(q-2\pi h/a\right) \tag{2.100}$$

When N can not be approximated as going towards infinity, this expression writes out as [61]:

$$\mathcal{F}\left[\sum_{u=1}^{N}\delta\left(r-ua\right)\right]=\frac{\sin\left(qaN/2\right)}{\sin\left(qaN\right)}\exp\left[iqa\left(N-1\right)/2\right] \tag{2.101}$$

Because the observable intensity is proportional to the absolute square of this expression, the phase factor can be neglected. It is common to allow for the scattering vector to deviate slightly from the Laue condition, so that in the one-dimensional case $q=\left(h+s\right)2\pi/a$, where $s\ll 1$. From Equation 2.101 the expression for the interference function in one dimension then becomes:

$$S\left(q\right)=\frac{\sin\left(N\pi\left(h+s\right)\right)}{\sin\left(\pi\left(h+s\right)\right)} \tag{2.102}$$

Now, for a three-dimensional lattice the scattering amplitude can be expressed as the product of the results of equations 2.92 and 2.99, yielding the following:

$$\begin{aligned}F\left(\vec{q}\right) &= S\left(\vec{q}\right)F_{hkl}\left(\vec{q}\right)\\ &= \frac{\left(2\pi\right)^3}{\vec{a}\cdot\left(\vec{b}\times\vec{c}\right)}\sum_{hkl}\sum_{j}f_j\delta\left(\vec{q}-\vec{G}_{hkl}\right)\exp\left[i\vec{q}\cdot\vec{r}_j\right]\\ &= \frac{\left(2\pi\right)^3}{\vec{a}\cdot\left(\vec{b}\times\vec{c}\right)}\sum_{hkl}\sum_{j}f_j\exp\left[i\vec{G}_{hkl}\cdot\vec{r}_j\right]\end{aligned} \tag{2.103}$$

It is common to write the atomic positions r_j as a sum over fractional lattice vectors $x_j\vec{a}$, $y_j\vec{b}$ and $z_j\vec{c}$. The previous expression then simplifies to:

$$F\left(\vec{q}\right)=\frac{\left(2\pi\right)^3}{\vec{a}\cdot\left(\vec{b}\times\vec{c}\right)}\sum_{hkl}\sum_{j}f_j\exp\left[2\pi i\left(hx_j+ky_j+lz_j\right)\right] \tag{2.104}$$

From this expression it is seen that the unit cell structure factor can be written in a simpler form than that presented in Equation 2.92, so that it's expression now reads:

$$F_{hkl}\left(\vec{q}\right)=\sum_{j}f_j\exp\left[2\pi i\left(hx_j+ky_j+lz_j\right)\right] \tag{2.105}$$

For a one-dimensional lattice the scattering amplitude is the product of this expression with Equation 2.102.

Scattering from a stack of planes

Now, in a real material made up of many grains or particles displaying one-dimensional stacked structures, the number of lattice points N in the

stacking direction is normally not constant but varies say, between an N_{min} and an N_{max}. The distribution of different N's over this range can be written as a function $g(N)$. The effect of this non-sharp distribution is that the interference function from a real, one-dimensionally stacked material is a weighted sum over the contributions attributable to each given N [19]:

$$S(\vec{q}, g(N)) = \sum_{N=N_{min}}^{N_{max}} g(N) \frac{\sin(N\pi(h+s))}{\sin(\pi(h+s))} \tag{2.106}$$

The FWHM-value of the main scattering peak from a one-dimensional structure as a function of the scattering vector, is approximately proportional to $1/N_{av}$, where N_{av} is the average number of lattice positions [2, 19]. The real space stacking distance d, corresponding with the length of the vector $\vec{R}_{uvw}$ between neighboring lattice points, might also vary slightly for a one-dimensional stacked structure, such as for instance a clay platelet. According to da Silva et al. [9], both the average number of stacks N_{av} and the so-called strain $\Delta d/d$, can be arrived at by plotting the widths $\Omega_L \approx 2\pi/N_{av}d + \Delta dq/d$ of a range of (00l) Bragg peaks as functions of the scattering vector at peak maxima and interpolating. This procedure does however require prior knowledge of to the so-called instrumental width Ω_G, whose contribution to the observed peak widths is not attributable to the sample itself but to the experimental setup.

The scattered intensity at small angles

The previous sections have treated the scattering from one- and three-dimensionally repeated structures. The former is a representation of a clay platelet, for which the number of unit layers in a given particle represents the number of lattice sites present in the stacking direction. However, it is apparent that colloidal clay dispersions have structural variations that go beyond the unit layer stacks, as the clay particles themselves are embedded in water. This leads to a new kind of scattering contrast, now occurring between the clay particles and their presumed continuous aqueous environment. Because observed first order reciprocal scattering vector lengths are inversely proportional to corresponding repetition distances d in real space, it becomes apparent that the scattering resulting from contrasts between colloidal particles and their environment will be present at small q and hence observable only for low values of the scattering angle.

The form factor for flat discs

Within the field of small angle scattering from colloidal clay dispersion it is common to treat clay platelets as discs [39, 18]; this is an approximation since real clay particles are irregularly shaped. The form factor for a flattened

cylinder of radius R and thickness $t/2$ is given as [27];

$$Y(q,\alpha) = 2C\frac{\sin(q(t/2)\cos\alpha)}{q(t/2)\cos\alpha}\frac{J_1(qR\sin\alpha)}{qR\sin\alpha} \tag{2.107}$$

Here $C = \rho V$ is a constant, equal to the total number of electrons of the flat cylinder, where V is the particle volume and ρ the average electron density; α is the angle between the cylinder normal $\vec{n}$ and the scattering vector $\vec{q}$, and J_1 the first order Bessel function of first kind, which can be expressed for an argument x as [6]:

$$J_1(x) = \frac{x}{2\Gamma(2)}\left(1 - \frac{x^2}{8} + \frac{x^4}{192} - ...\right) \tag{2.108}$$

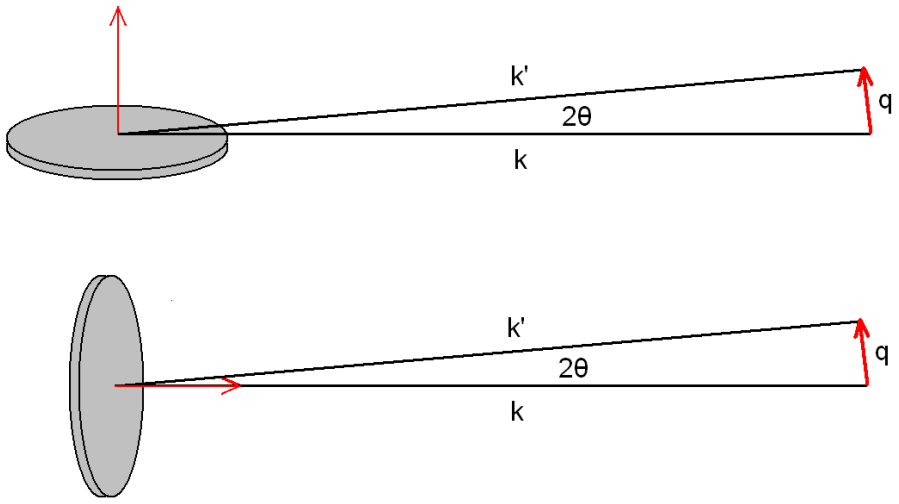

Figure 2.14: Scattering geometries where x-rays of wavevector $\vec{k}$ are incident on clay platelets oriented with their optical axes $\vec{n}$ either perpendicular to or parallel with $\vec{k}$, as shown respectively in the top and bottom images. Because of the small scattering angle 2θ, the topmost image corresponds with a scattering geometry where $\vec{q}$ is approximately parallel with $\vec{n}$, whereas the bottom image has $\vec{q}$ approximately perpendicular to $\vec{n}$.

For fluorohectorite platelets the cylinder normal $\vec{n}$ corresponds with the optical axis. The scattered intensity from a colloidal dispersion of flattened cylinders will be proportional to the absolute square of the cylinder form factor. By considering Equation 2.107, it is seen that the scattered intensity attributable to the contribution from the cylinder form factor will show a q^{-2}-dependence modulated by the sinusoidal and Bessel functions in q.

Figure 2.14 shows two illustrations of how clay platelets may be oriented with respects to the incoming x-ray beam in typical experiments on nematic Na-fluorohectorite dispersions. Now, when the scattering vector $\vec{q} \perp \vec{n}$, the angle $\alpha = 90^\circ$ and the first factor of Equation 2.107 is a sinc-function whose argument goes to zero; it is therefore equal to one, and the form factor is independent on the cylinder thickness t and depends only on the radius R;

$$Y_{\vec{q}\perp\vec{n}}(q) = 2C\frac{J_1(qR)}{qR} \tag{2.109}$$

Because the scattered intensity is proportional to the absolute square of the cylinder form factor, it follows that for a scattering geometry where $\vec{q} \perp \vec{n}$ the contribution to the intensity attributable to the cylinder form factor is proportional to q^{-2} modulated by the Bessel function $J_1(qR)$. In the opposite case where the scattering vector $\vec{q} \parallel \vec{n}$ and $\alpha = 0^\circ$, the second factor in the expression for the cylinder form factor equals the right side of Equation 2.108 divided by x, where $x = qR\sin\alpha$ goes to zero; this factor thus writes out as $1/2\Gamma(2) = 1/2$. The cylinder form factor for $\vec{q} \parallel \vec{n}$ then is dependent only on the cylinder thickness t:

$$Y_{\vec{q}\parallel\vec{n}}(q) = C\frac{\sin(q(t/2))}{q(t/2)} \tag{2.110}$$

Again the scattered intensity will be proportional to the absolute square of this expression, and hence proportional to q^{-2} modulated by the absolute square of the $\sin(q(t/2))$ term. Figure 2.15 shows plots of the absolute square of the cylinder form factor as expressed through equations 2.109 and 2.110. It is seen that when $\vec{q} \perp \vec{n}$ the locations of the maxima of the absolute square of the cylinder form factor will be located on a line proportional to q^{-3} when $qR >\approx 2$, whereas in the $\vec{q} \parallel \vec{n}$ scattering geometry the maxima will lie on a line falling off as q^{-2} for $qt/2 >\approx 1.5$, i.e. when $qt >\approx 3$. These plots were made on the assumption of a monodisperse system. For polydisperse systems characterized by a distribution in particle thicknesses and radii, the oscillations in the absolute square of the form factor will even out and approach the illustrated power laws.

2.4.3 X-ray sources for structural research

The current section will present a brief overview of modern sources of x-rays, where the main focus will be on the basic physical processes involved. A voluminous literature on the technical features of x-ray sources exists. These topics will not be treated in the present discussion. Important parameters in the current discussion are however the x-ray wavelengths, intensities and origins. As already mentioned, x-rays used in structural scattering studies have a wavelength on the order of 1 Å; this length reflects approximate inter-atomic distances, and a wavelength of exactly 1.00 Å corresponds with

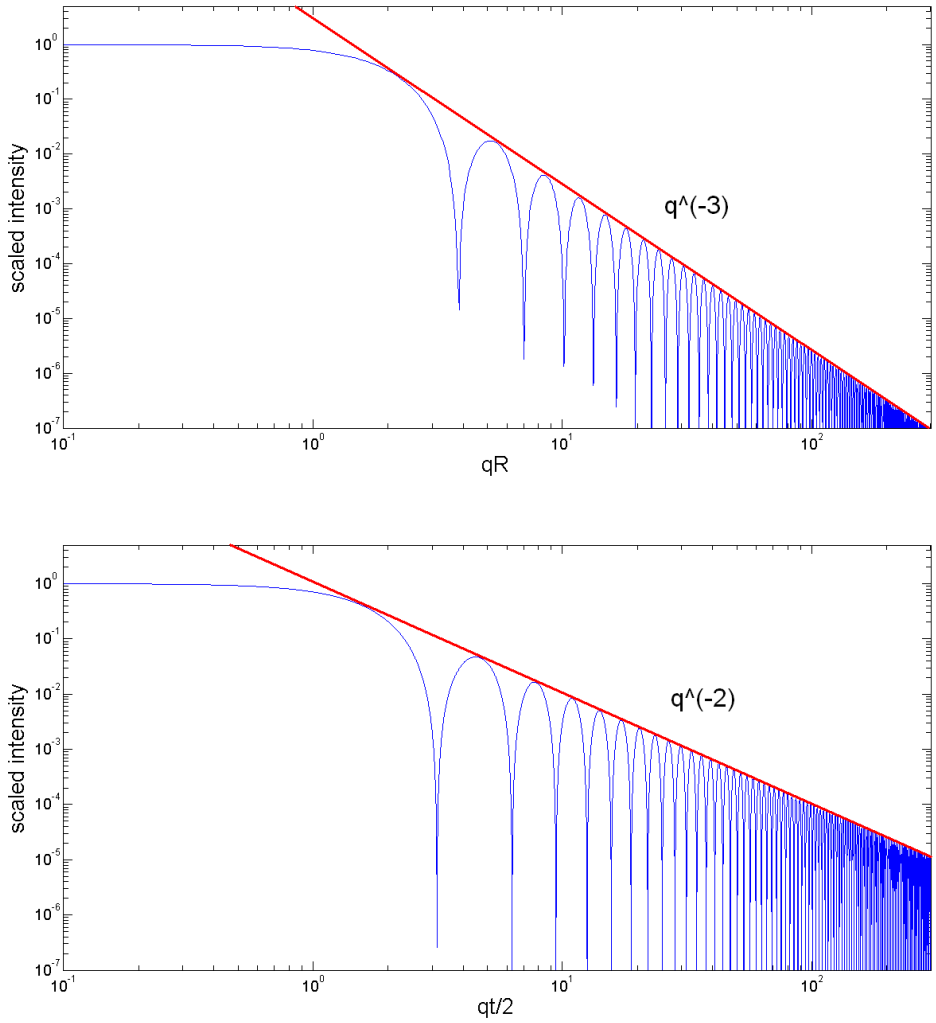

Figure 2.15: Plots of the absolute square of the cylinder form factors of equations 2.109 for $\vec{q} \perp \vec{n}$ (top) and 2.110 for $\vec{q} \parallel \vec{n}$ (bottom), where both squared equations have been divided by the factor C squared, so that for $q = 0$ both plots take a value of one.

a photon energy of 12.4 keV. Now, typical energy differences between certain atomic orbitals are in this range, and this fact is what forms the basis of traditional x-ray sources based on Cu-anodes. Synchrotron sources on the other hand are based on the radiation emitted by accelerating, relativistic electrons.

Cu-anode based x-ray sources

In a traditional Cu-anode based x-ray source, a voltage is applied across a filament, known as the cathode, and a variable current allowed to pass through the filament [19]. When the electrons constituting this current are energetic enough, filament electrons will be knocked free of the material and into the vacuum space surrounding the cathode. Now, in this vacuum chamber there is also a Cu-anode connected by a high voltage to the cathode. The electrons that escape the cathode filament will therefore be accelerated towards the Cu-anode, emitting some electromagnetic radiation. At the anode, the electrons will quickly slow down and emit a continuous Bremsstrahlung background upon which is superimposed discrete x-ray peaks. These peaks originate from electron interactions with the Cu-atoms, where typically a K-shell electron is knocked free of it's orbital. Following such an event, the atom de-excites when a higher orbital electron falls into the hole state orbital [40]. The energy difference between the higher and lower orbital states is emitted in the form of an x-ray photon of a defined energy. The $\mathrm{Cu}_{K\alpha}$-line at a photon wavelength of 1.5418 Å, originating from electron transitions between the L- and K-shells, is used in many x-ray generators.

Synchrotron radiation

Synchrotron radiation arises when relativistic electrons are forced to travel in a segmented, polygonal path by so-called bending magnets. The electrons are first accelerated in a linear accelerator, transferred to a booster ring where they are further accelerated, and then finally injected into the synchrotron storage ring, where the x-rays used for research are generated through the action of the mentioned bending magnets on the electron beam. Typical synchrotrons operate with electron energies in the storage ring of a few GeV. The rest mass energy of an electron is $m_e c^2 = 511$ keV, and so electrons of for instance 2.5 GeV, which is the energy used at the PAL synchrotron, are relativistic, traveling at around 91% the speed of light.

The Lorentz force law relates the electric and magnetic field amplitudes to the force an electromagnetic field exerts on an electron of charge $-e$ and velocity $\vec{v}$ [26]:

$$\vec{F} = -e\left(\vec{E} + \vec{v} \times \vec{B}\right) \tag{2.111}$$

This force law is invariant under coordinate transformations [82], and can therefore also be applied to relativistic charged particles. The path integral

over this force yields the change in the particle's kinetic energy K due to the electromagnetic field [82];

$$\begin{aligned} \Delta K &= -e\left(\int \vec{E}\cdot d\vec{s} + \int \left(\vec{v}\times\vec{B}\right)\cdot\vec{v}dt\right) \\ &= -e\left(\int \vec{E}\cdot d\vec{s}\right) \end{aligned} \tag{2.112}$$

In the integral depending on $\vec{B}$, $d\vec{s}$ has been replaced by $\vec{v}dt$ and, since $(\vec{v}\times\vec{B})\cdot\vec{v}\equiv 0$, it is seen that the magnetic field does not contribute to change the particle's kinetic energy. It does however, contribute to the change $\Delta\vec{p} = \int \vec{F}dt$ in the particle momentum, and because the magnetic field is coupled to the particle velocity via a cross-product, the momentum change will be perpendicular to both $\vec{v}$ and $\vec{B}$.

Now, when any charged particle accelerates, it will induce electromagnetic radiation. The Liénard-generalized Larmor formula expresses the power radiated by a point charge (in the current discussion, an electron) whose instantaneous acceleration is given by the vector $\vec{a}$ [26]:

$$P = \frac{\mu_0 e^2\gamma^6}{6\pi c}\left(a^2 - \left|\frac{\vec{v}\times\vec{a}}{c}\right|^2\right) \tag{2.113}$$

Here γ is the relativity factor:

$$\gamma = \frac{1}{\sqrt{1-(v/c)^2}} \tag{2.114}$$

From Equation 2.113 it is seen that the radiated power of a an accelerating point charge increases massively as v approaches the speed of light. When the acceleration vector $\vec{a}$ is perpendicular to the velocity vector $\vec{v}$, which is valid for electrons traveling in a approximated circular path in a storage ring, the total radiated power is given as [26]:

$$P = \frac{\mu_0 e^2 a^2\gamma^4}{6\pi c} \tag{2.115}$$

Utilizing a cartesian coordinate system where $\vec{v}\parallel z$ and $\vec{a}\parallel x$ so that the polar angle is θ and the azimuthal angle denoted by ϕ, the fractional amount of power dP emitted into a solid angle element $d\Omega$ is given as [26]:

$$\frac{dP}{d\Omega} = \frac{\mu_0 e^2 a^2}{16\pi^2 c}\left(\frac{(1-\beta\cos\theta)^2 - \left(1-\beta^2\right)\sin^2\theta\cos^2\phi}{(1-\beta\cos\theta)^5}\right) \tag{2.116}$$

Here $\beta = v/c$. For relativistic particles this parameter approaches one, and the radiation is increasingly focused around the forward direction along the instantaneous velocity vector $\vec{v}$. From this discussion, it is seen that by using relativistic electrons as x-ray sources, one obtains considerable radiation intensity and collimation, both highly desirable in structural studies.

Chapter 3

Experimental

3.1 Samples and sedimentation photography

The present chapter will deal with factors directly related to the experimental studies performed in the current project; these factors comprise sample preparation, optical photography and x-ray scattering studies, and data analyses. Sample preparation will be addressed first. Five different batches of fluorohectorite powder were utilized in this project, of which two consisted of Na-fluorohectorite, one of Li-fluorohectorite, one of Fe-fluorohectorite and one of Ni-fluorohectorite. The two batches of Na-fluorohectorite are distinguished as apr and nov powders, whereas the Li-, Fe- and Ni-fluorohectorite batches are known as respectively li, fe and ni. The powders were purchased from Corning Inc. in the form of Li-fluorohectorite and ion exchanged prior to the work of this master thesis.

To prepare the colloidal clay-water samples the Na- and Li-fluorohectorite powders were mixed with solutions of 10^{-3} M NaCl and LiCl in water, respectively. The effect of salt concentration on Na-fluorohectorite samples has been thoroughly examined by Ringdal [59] and by Fonseca [16]. The phase behavior of Li-fluorohectorite has not been previously investigated by the COMPLEX group. Because LiCl has the same 1:1 valency as NaCl, the Li-fluorohectorite clay powder was also mixed with a 10^{-3} M salt solution. The colloidal samples were prepared by weighing in first half the amount of salt solution in a glass container, then by weighing in the clay powder, followed by weighing in the rest of the salt solution. The different mixed sample batches are listed in Table 3.1, which also contains information with regards to the mixed Fe- and Ni-fluorohectorite batches.

All samples were mixed in large glass containers of diameters of either 1.5 cm or 3.0 cm. These were shaken for an hour or more in a mechanical shaker before being drawn into a syringe and filled into smaller cylindrical Mark tube sample holders. The Mark tube capillaries were purchased from Hilgenberg, had diameters of respectively 1 mm or 2 mm, a wall thickness

of approximately 10 µm and were made of borosilicate glass. A few samples were also placed in larger, flat rectangular capillaries. These are shown in Figure 3.1. Optical images between crossed polarizers were taken of the samples during sedimentation. The setup used for sample photography was thoroughly described by Ringdal in [59]. Some images were also taken with a Stemi 2000-C microscope and a PixeLINK camera. In this setup, the sample was illuminated by a linear-polarized lightsource. It was found that the microscope setup only was capable of imaging the center of the Mark tube capillaries; it is therefore important to note that the visible birefringent regions in microscope photographs do not extend to the capillary edges.

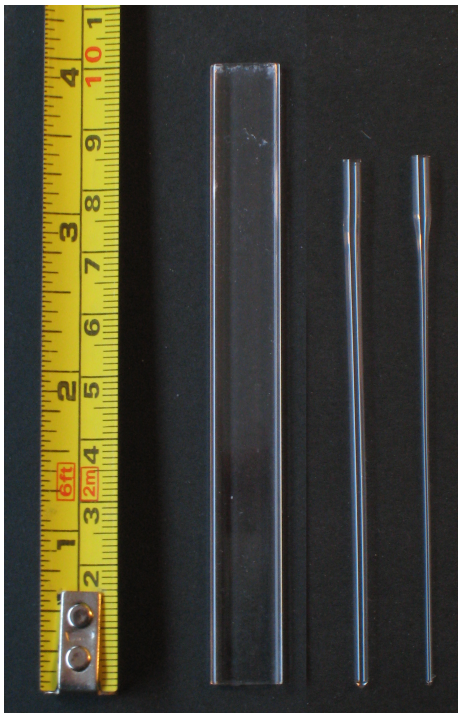

Figure 3.1: Sample holders. A flat rectangular capillary, plus 2 mm and 1 mm Mark tubes.

Table 3.1: The different batches of prepared samples. Each sealed capillary or other means of containment was named starting with the mix number (no. parameter) which it was drawn from. Samples 17 and 18 were mixed in distilled water with no added salt. Note that the distilled water is assumed to have a pH of 7 so that the ion concentration of H_3O^+ and OH^- is of around 10^{-7} M.

no.	powder			salt			mix	
	type	batch	weight [g]	type	molarity [M]	weight [g]	w/w%	date
1	NaFht	nov	0.12	NaCl	$1.0 \cdot 10^{-3}$	4	3.0	15jan08
2	NaFht	nov	0.1028	NaCl	$1.0 \cdot 10^{-3}$	4.0155	2.5	18jan08
3	NaFht	nov	0.1245	NaCl	$1.0 \cdot 10^{-3}$	4.0214	3.0	22jan08
4	NaFht	nov	0.0817	NaCl	$1.0 \cdot 10^{-3}$	4.0075	2.0	28jan08
5	NaFht	nov	0.3718	NaCl	$1.0 \cdot 10^{-3}$	12.0105	3.0	29jan08
6	NaFht	nov	0.6179	NaCl	$1.0 \cdot 10^{-3}$	19.9996	3.0	30jan08
7	NaFht	nov	n/a	NaCl	$1.0 \cdot 10^{-3}$	n/a	3.0	23feb08
8	NiFht	ni	0.2469	$NiCl_2$	$5.0 \cdot 10^{-4}$	8.0182	3.0	2mar08
9	FeFht	fe	0.2412	$FeCl_3$	$3.3 \cdot 10^{-4}$	8.0091	3.0	2mar08
10	FeFht	fe hc	0.1243	$FeCl_3$	$3.3 \cdot 10^{-4}$	4.0602	3.0	2mar08
11	NiFht	ni hc	0.1236	$NiCl_2$	$5.0 \cdot 10^{-4}$	4.0137	3.0	2mar08
12	LiFht	li hc	0.1231	LiCl	$1.0 \cdot 10^{-3}$	4.0098	3.0	3mar08
13	LiFht	li hc	0.1243	LiCl	$1.0 \cdot 10^{-3}$	4.0257	3.0	3mar08
14	NaFht	apr hc	0.7471	NaCl	$1.0 \cdot 10^{-3}$	24.0487	3.0	3mar08
15	NaFht	apr hc	0.7441	NaCl	$1.0 \cdot 10^{-3}$	24.0269	3.0	3mar08
16	LiFht	li hc	0.4177	LiCl	$1.0 \cdot 10^{-3}$	10.0803	4.0	5mar08
17	FeFht	fe hc	0.1250	no salt	$\approx 10^{-7}$	4.0202	3.0	5mar08
18	NiFht	ni hc	0.1267	no salt	$\approx 10^{-7}$	4.0350	3.0	5mar08

3.2 X-ray investigations

Some of the 1 mm and 2 mm Mark tube capillaries of this project were investigated by x-ray scattering. The following sections will briefly address the x-ray facilities of respectively the NTNU lab in Trondheim, Norway and the PLS synchrotron facility in Pohang, South Korea. Certain details pertaining to the analysis of the recorded synchrotron scattering data will also be discussed. Finally an overview is given of the fitting procedures applied for analyzing scattering data in relation to the current project.

3.2.1 Bruker NanoStar SAXS – in-house x-ray facilities

The NTNU COMPLEX lab has a Bruker Nanostar SAXS apparatus, delivering $Cu_{K\alpha}$ radiation, that was used in the current project for studies of the scattering at small angles from the aqueous clay dispersions held in 1 mm Mark tubes. Experimental parameters relevant for the in-house x-ray scattering experiments are listed in Table 3.2.

Table 3.2: Parameters relevant for the x-ray experiments conducted at the NTNU lab.

parameter	value
x-ray wavelength	1.5418 Å
detector size	512×512 pixels
detector active area diameter	11.5 cm
sample-to-detector distance	106 mm
max reciprocal range	0.19 nm^{-1}–3.8 nm^{-1}
max real space range	1.7 nm–33 nm

3.2.2 PLS synchrotron scattering

A four weeks stay at the PLS synchrotron in Pohang, South-Korea featured as a part of the current project. The PLS synchrotron is a third generation synchrotron, running since year 2000 at 2.5 GeV. The beamline used was the GIST owned 5C2, a beamline used for diverse experiments by both students and researches and that thus required a certain amount of preparations and adjustment before being operable. Experimental parameters relevant for the PLS synchrotron scattering experiments are listed in Table 3.3.

Table 3.3: Parameters relevant for the x-ray experiments conducted at the PAL synchrotron.

parameter	value 1st set	value 2nd set
x-ray wavelength	1.243769 Å	1.243769 Å
detector size	1024 × 1024 pixels	1024 × 1024 pixels
beam center	395 × 345 pixels	383 × 195 pixels
pixel size	13 µm	13 µm
sample-to-detector distance	83 mm	107 mm
max reciprocal range	0.94 nm^{-1}–4.7 nm^{-1}	0.62 nm^{-1}–4.5 nm^{-1}
max real space range	1.3 nm–6.7 nm	1.4 nm–10 nm

Complications with non-centered, extended beamstops

The detector used for recording scattered radiation at the 5C2 beamline in relation to the current project had, as shown in Table 3.3, a high resolution determined by an array of 1024 × 1024 13 µm sized pixels. The detector size however was thus only 1.3 × 1.3 cm, and so the detector had to be placed close to the sample in order to cover a large enough solid angle to allow for observation of the Bragg scattered radiation from stacked clay unit layers. In order to avoid the most severe complications of placing the flat detector very close to the sample, a compromise was made between this distance and the usual procedure of having the non-obscured beam hitting the detector center. As shown in Figure 3.2, the detector was placed so as to record as much as possible of the 2wl (001) Bragg ring, by translating it a distance away from the centered position, without having to move it too close to the sample. Figure 3.2 also shows how a normal, non-caked integration procedure in fit2d would be carried out on the recorded data. Performing such an integration on the scattering data from PLS were seen to produce artificial intensity cut-offs, that might easily be mistaken for features attributable to the sample studied. All integrations in this report were hence performed over a limited interval of the detector pixels, defined so as to avoid integrating over regions obscured by either the beamstop or by the walls. This reduced the range of available q-lengths relative to those listed in Table 3.3, both on the high and low q ends of the recorded scattering profiles. It also restricted the azimuthal range to less than 180°.

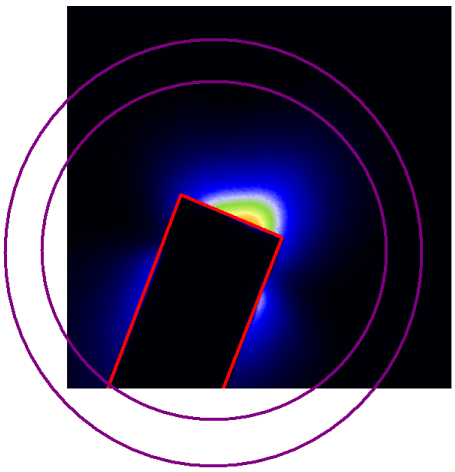

Figure 3.2: Illustration of how a normal fit2d integration procedure on the given scattering data could be thought to produce artificial intensity profile features when the azimuthal angle moves outside of the detector area.

Peak broadening due to sample widths

A possible problem encountered with the use of samples that extend a certain distance along the beam path, especially when the detector is close to the sample, is peak broadening. The situation is illustrated in Figure 3.3. For simplicity, only scattered rays from the two extremities of the sample along the beam path are considered. Now, the relationship between the scattering angle 2θ, which according to Bragg's law is given as $2\theta = 2\sin^{-1}(n\lambda/2d)$, and the length parameters defined in the leftmost illustration of Figure 3.3, is given by:

$$\tan(2\theta) = \frac{r}{l} \tag{3.1}$$

$$\tan(2\theta) = \frac{r+\Delta r}{l+\Delta l} \tag{3.2}$$

From these expressions the detection radii for rays scattered at 2θ respectively from the front or back of the sample can be written as:

$$r = (l)\tan(2\theta) \tag{3.3}$$

$$r+\Delta r = (l+\Delta l)\tan(2\theta) \tag{3.4}$$

Now, in the rightmost picture of Figure 3.3, the relationship between the assumed scattering angles $2\theta'$ and $2\theta' + \Delta 2\theta'$ for the rays detected at respec-

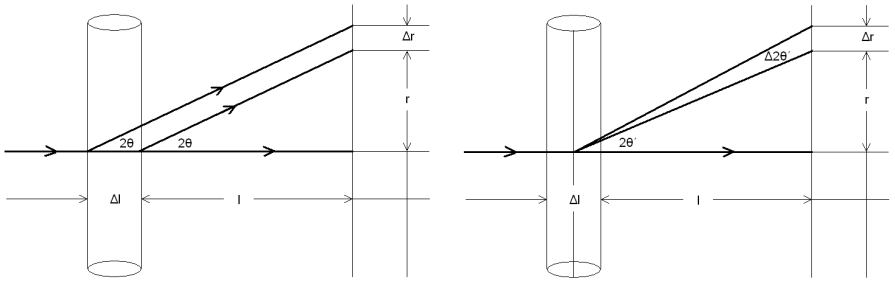

Figure 3.3: Peak broadening due to finite path length of beam through sample. The left figure illustrates the actual experimental setup, whereas the figure to the right shows the geometry of the model in which data analyses are performed.

tively r and $r + \Delta r$, and the associated length parameters, reads:

$$\tan\left(2\theta'\right) = \frac{r}{l + \Delta l/2} \tag{3.5}$$

$$\tan\left(2\theta' + \Delta 2\theta'\right) = \frac{r + \Delta r}{l + \Delta l/2} \tag{3.6}$$

The corresponding q-values are then given as:

$$q\left(2\theta'\right) = \frac{4\pi}{\lambda} \sin\left(\frac{1}{2}\tan^{-1}\left(\frac{r}{l + \Delta l/2}\right)\right) \tag{3.7}$$

$$q\left(2\theta' + \Delta 2\theta'\right) = \frac{4\pi}{\lambda} \sin\left(\frac{1}{2}\tan^{-1}\left(\frac{r + \Delta r}{l + \Delta l/2}\right)\right) \tag{3.8}$$

By inserting the expression for r and $r + \Delta r$, this becomes:

$$q\left(2\theta'\right) = \frac{4\pi}{\lambda} \sin\left(\frac{1}{2}\tan^{-1}\left(\frac{(l)\tan\left(2\theta\right)}{l + \Delta l/2}\right)\right) \tag{3.9}$$

$$q\left(2\theta' + \Delta 2\theta'\right) = \frac{4\pi}{\lambda} \sin\left(\frac{1}{2}\tan^{-1}\left(\frac{(l + \Delta l)\tan\left(2\theta\right)}{l + \Delta l/2}\right)\right) \tag{3.10}$$

Now, the (001) interlayer Bragg peak of 2wl hydrated Na-fluorohectorite has a 2θ value of 0.083 rad, given the experimental parameters of Table 3.3. Assume $\Delta l = 2$ mm. According to the above calculations, this would yield a $q\left(2\theta'\right) = 4.14\ \mathrm{nm}^{-1}$ and a $q\left(2\theta' + \Delta 2\theta'\right) = 4.24\ \mathrm{nm}^{-1}$, or a $q\left(2\theta'\right) = 4.15\ \mathrm{nm}^{-1}$ and a $q\left(2\theta' + \Delta 2\theta'\right) = 4.23\ \mathrm{nm}^{-1}$, for respectively the first and second experimental sets of Table 3.3. In both cases it is seen that, at this scattering angle, the reciprocal space broadening attributable to the finite beam path through the sample is on the order of $0.1\ \mathrm{nm}^{-1}$. For $\Delta l = 1$ mm the broadening is on the order of $0.05\ \mathrm{nm}^{-1}$.

A weakness of this technique for the assessment of peak broadening, lies however in its dependence upon the determined sample-to-detector distance. Because this distance commonly is arrived at by fitting reciprocal peak centra with the known q-values of selected (hkl) peaks, it's determined value is dependent upon the peak broadening or, more precisely, on the peak intensity distribution as a function of 2θ. This distribution, which affects the apparent center of a peak, might depend on the broadening. It is possible that the choice of the mid-sample plane at $l + \Delta l/2$ as an approximation to the determined sample-to-detector distance is not the optimal one. Although for a round capillary sample this plane theoretically does contain the largest number of scatterers, the beam attenuation might serve to shift the plane of maximal scattering events further towards the beam source. Under the assumption that the experimentally determined sample-to-detector distance corresponds with the distance to the plane of maximal scattering, a shift of the latter closer to the beam source, would decrease the broadening relative to that determined for the mid-plane case, as the difference between $2\theta'$ and $2\theta' + \Delta 2\theta'$ in such a geometry becomes smaller. The reverse would be true should the determined sample-to-detector distance corresponds with a scattering plane closer to the detector than the sample mid-plane.

3.3 Software, data analysis and image processing

Mainly two kinds of software were utilized in this project. Image Magick, Microsoft Paint, Adobe PDF and Ghostscript as well as Blaze Media Pro, Windows Movie Maker and Zoom Browser were used for image and film processing. Yorick, MatLab, Origin Pro, fit2d, Bruker SAXS software and a group of Perl scripts and MatLab functions written by Yvés Méheust [48] and modified and extended by Henrik Hemmen [30] for inferring the order of nematic phases from x-ray data, were used in the analysis of the obtained scattering images. A few short comments on the practical uses of Image Magick and Yorick are presented in Appendix C. The theory behind the fitting scripts by Méheust and Hemmen are well documented in [48]. The following section will present a brief overview of this theory.

Script fitting procedures and the nematic order parameter

The current discussion is based on the paper [48] by Méheust et al. and concerns methods for inferring the order of nematics from scattering data. Figure 3.4 shows the geometries of the model presented in [48]. A scatterer, in the current discussion a lamellar fluorohectorite particle, is situated at the origin O of a cartesian coordinate system defined by the mutually perpendicular x, y and z axes. The x-ray beam is fittingly incident along the x-axis and, in the absence of obstructions in the beam path, strikes a detector parallel with the yz-plane in O' on the x-axis, as shown in Figure 3.4.

The fluorohectorite particle is oriented so that it's optical axis $\vec{n}$ is oriented at an angle with respects to a reference orientation $\vec{n}_0$, equal to the director for a uniaxial nematic. The angle between $\vec{n}$ ($\vec{n}_0$) and the yz-plane is denoted by the angular coordinate Θ (Θ_0). The angle between the projection of $\vec{n}$ ($\vec{n}_0$) onto the yz-plane and the z-axis, is the azimuthal angle Φ (Φ_0). Scattered radiation from the fluorohectorite particle strikes the detector in M. The angle between the vector from O' to M and the z-axis is the azimuthal angle ϕ. The vector between O and M makes an angle 2θ with the x-axis.

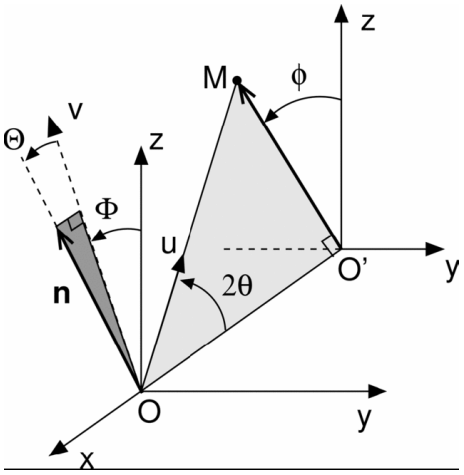

Figure 3.4: Illustration of the geometry of the model used to obtain the nematic order parameter from scattering data, retrieved from [48].

Now, as discussed in section 2.3.1, the orientational distribution function f for the optical axes $\vec{n}$ around the commonly preferred direction $\vec{n}_0$ for a uniaxial nematic is dependent only upon the angular coordinate α between any given $\vec{n}$ and the reference direction $\vec{n}_0$. The α corresponding with 2θ-scattered radiation observable at an M which is also described by the azimuthal ϕ, is given as [48]:

$$\alpha_{2\theta}(\phi) = \arccos\left(\sin\theta \sin\Theta_0 + \cos\theta \cos\Theta_0 \cos\left(\phi - \Phi_0\right)\right) \tag{3.11}$$

The orientational distribution function f for uniaxial nematics is expected to be well described by a so-called Maier-Saupe function of α [48, 41, 42]:

$$f(\alpha) \propto \exp\left(m \cos^2 \alpha\right) \tag{3.12}$$

The order parameter is then given by the expression derived in Equation

2.50, in section 2.3.1[1]:

$$S_2 = \int_0^{\pi} \frac{3\cos^2\alpha - 1}{2} f(\alpha) \sin\alpha d\alpha \tag{3.13}$$

As already mentioned, a series of Perl scripts and MatLab functions, as well as a generated fit2d macro, have been developed by Meheust and Hemmen with for the purpose of quickly and consistently determining the order of nematics studied by x-ray scattering. This collective routine was used on portions of the scattering data acquired in the current project. However, as evidenced by the preliminary scattering image presented in Figure 3.2, the scattering in the full 2wl Bragg ring cannot be recorded by the small detector used at the 5C2 beamline at the PAL synchrotron. A consequence of this is that the Φ-dependence of the orientational distribution function cannot be probed. The fitting procedure for the data of the current project therefore neglects this parameter and assumes an intensity profile that is symmetrical in ϕ. Modifications to the fitting scripts that account for this were added by Méheust and Hemmen.

[1]Note that the symbols have changed somewhat in the current description relative to that of section 2.3.1, where θ denoted the present α. The current description was chosen to match that of the model presented in [48].

Chapter 4

Results and Discussion

4.1 Preparation and phase separation in the gravitational field

Fluorohectorite samples in aqueous suspensions with cations of Na, Li, Fe or Ni as the intercalated species have been investigated in this project with the intent of describing the phase behavior of these samples during settling in the gravitational field. Already upon mixing the different clay powders with distilled water in large sample containers certain distinguishing features become readily observable. Figure 4.1 shows four newly prepared samples of Na- and Ni-fluorohectorite in distilled water, photographed before the containers were shaken to evenly disperse the clay. The Na-fluorohectorite samples show marked swelling and the formation of a membrane like layer of clay powder suspended at the air-water interface. The Ni-fluorohectorite samples on the other hand are shown to have formed a sediment at the bottom of the containers with little membrane formation and no apparent volume swelling. The same experiments performed on Li- and Fe-fluorohectorite showed that the Li-fluorohectorite samples behave in a manner similar to Na-fluorohectorite whereas Fe-fluorohectorite samples display the non-swelling characteristics of Ni-fluorohectorite. Note that non-swelling in this case refers to macroscopic behavior and not to water intercalation and crystalline swelling.

The same behavior documented through Figure 4.1 was also observed when the different cation intercalated fluorohectorite powders were mixed with water containing a chloride salt of the intercalated species. From section 2.2.2 it is known that di- and trivalent electrolytes present DLVO-regimes which differ from those of monovalent electrolytes such as NaCl and LiCl. Calculated from Equation 2.16 the Debye length of a 1:1 electrolyte at a salt concentration of 10^{-3} M is 9.6 nm whereas the same parameter takes a value of 7.9 nm for a 2:1 electrolyte at the same cation concentration. A more detailed picture was described in section 2.2.3, demonstrating

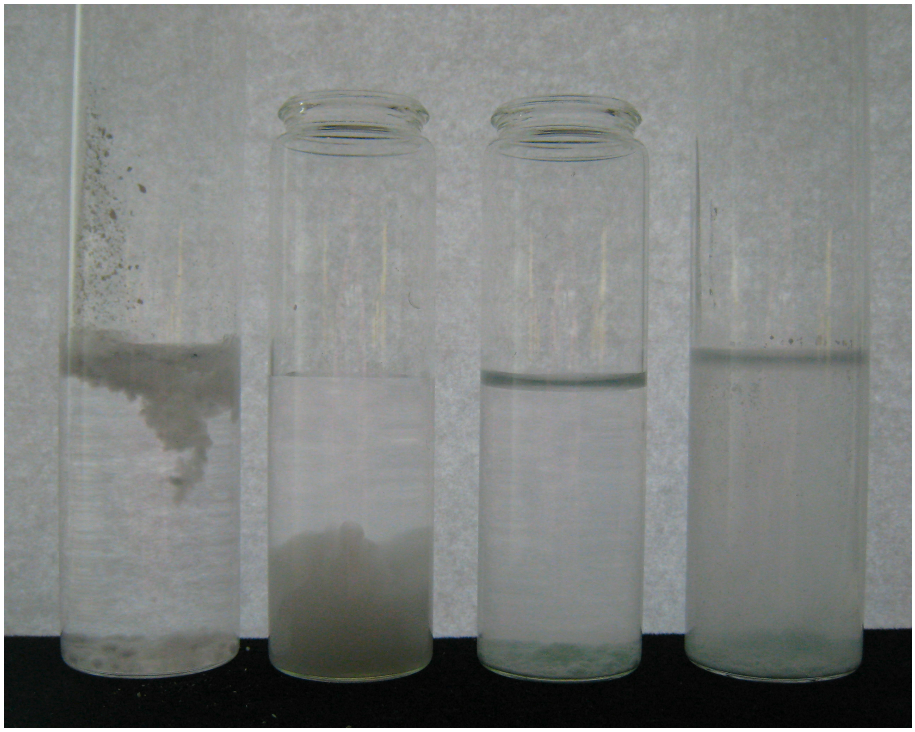

Figure 4.1: Four samples of respectively Na-fluorohectorite and Ni-fluorohectorite in distilled water. The two samples to the left are of Na-fluorohectorite photographed approximately 5 min and 30 min after the clay powder was sprinkled onto the distilled water surface. The macroscopic swelling properties of this clay is clearly demonstrated. The two samples to the right are of Ni-fluorohectorite photographed approximately 30 min and 5 min after the clay powder was added to the distilled water in the glass containers. These clay samples show little swelling and do not form the same membrane like clay layer at the air-water interface as does the Na-fluorohectorite samples. All samples contained approximately the same amount by volume of clay powder.

how di- or trivalent electrolytes are thought to dramatically increase the screening of surface potentials, thus promoting flocculation and aggregation which again leads to faster sedimentation rates. In the above case however, the Na- and Ni-fluorohectorite powders were also mixed with distilled water which should contain only a very small amount of ionic species. Unless the dialysis of the clay powders was incomplete upon drying it is therefore unlikely that any valency dependent features of the aqueous solvent should account for the striking dissimilarities between the different clay powders seen in Figure 4.1. Dialysis performed on the Fe- and Ni-fluorohectorite powder batches used in this experiment showed no traces of remnant Cl^- ions. It can however be envisioned that the presence of the intercalated species on the exposed fluorohectorite surfaces is sufficiently strong so as to markedly increase potential screening for di- and trivalent cations relative to monovalent ones.

It is well known, also from the discussions of section 2.2.3, that the nature of the intercalated ion significantly affects the swelling capacity of a given clay powder. Odom [54] and more recently Skipper et al. [63] summarize that upon hydration Na-smectites exhibit in general extensive swelling whereas the often more naturally common smectites with a large portion of intercalated Ca and Mg [54] or K [63] show practically no swelling even when fully hydrated. The most common ionic forms of Ca and Mg are the divalent Ca^{2+} and Mg^{2+} ions, whereas K occurs as monovalent K^+. Salles et al. [60] have investigated the hydration of monovalently intercalated montmorillonites, finding that hydration of the intercalated cations is the main driving force during hydration of the swelling Na- and Li-montmorillonites whereas for the non-swelling K-, Rb- and Cs-montmorillonites hydration of the silicate layers becomes increasingly important. As discussed in section 2.2.3, many studies have been devoted to determining the nature of the water layers in hydrated clays, finding that both intercalated cation valencies, radii and hydration enthalpies, as well as the types and locations of the layer charges are important parameters. Altogether, the behaviors observed in the current discussion for respectively mono- and di- or trivalently intercalated fluorohectorites, even if not fully understood, still match the results obtained for other montomorillonite/smectites [46, 54, 60, 63].

Further obvious differences were however observed between respectively the Na- and Li-fluorohectorite and the Fe- and Ni-fluorohectorite samples investigated in this project. Na- and Li-fluorohectorite samples were seen to remain dispersed after mixing, forming moderate, true sediments only during the first few hours after preparation, after which the much slower phase separation occurred on timescales of weeks and months in the large containers. Over the course of a few days to several weeks the Li-fluorohectorite capillary samples investigated were observed to undergo phase transitions relatively similar to previous and to current observations on the phase separation of Na-fluorohectorite in the gravitational field. This is further discussed in a

later section. No clear phase separations however were observed for neither the Fe- nor especially the Ni-fluorohectorite samples prepared in this project. Even at relatively low di- or trivalent salt concentrations of about 10^{-4} M the Fe- and Ni-fluorohectorite samples were seen to form flocs after the containers were shaken, which grew in size on timescales of a few seconds. If left alone, these samples sedimented and formed a clear-cut boundary to a transparent, colorless upper phase with presumably little to no dispersed clay in it in a matter of an hour or so. However, it was found that shaking the Fe- and Ni-fluorohectorite containers easily re-dispersed the clay. Based on these preliminary investigations, Fe- and Ni-fluorohectorite samples mixed with distilled water were subjected to ultrasonic treatment for several hours. These treated samples no longer showed naked-eye observable flocculation but rather formed loose, seemingly non-flocculated sediments. The Ni-fluorohectorite samples again were seen to develop a clear-cut boundary between the loose sediment and a transparent, colorless upper phase whereas in the Fe-fluorohectorite samples the upper, less dense phase was seen to contain dispersed clay that after more than two months still had not settled out of suspension. When these observations are taken together with the discussion of section 2.2.1 on gravitational sedimentation, it seems likely that the reason for the originally fast sedimentation seen in the Fe- and Ni-fluorohectorite samples might have been the presence of larger aggregated structures, present either in the original powders or created as flocs upon contact with water. The ultrasonic treatment likely destroyed some of these presumed aggregates, leading to the slower sedimentation rates, something which argues in favor of the hypothesis that a certain amount of aggregates were present already in the powdered Fe- and Ni-fluorohectorite samples. It can however also be envisioned that the presence of the intercalated cation species on the exposed platelets surfaces is sufficient to cause the observed flocculation in the case of Fe- and Ni-fluorohectorite samples.

The following sections further describe the gravitationally induced phase separation observed in Na- and Li-fluorohectorite samples; a brief view is also presented with regards to a sedimenting Ni-fluorohectorite capillary sample.

4.1.1 Na-fluorohectorite

When newly prepared Na-fluorohectorite dispersions are left to sediment in the earth's gravitational field, several strata of visible phases develop over the course of days, weeks and months [12, 59]. This sedimentation behavior is at once highly reproducible, as illustrated in Figure 4.2, but also dependent on the geometry of the sample container. The following section will address the gravitational phase separation of aqueous Na-fluorohectorite dispersions.

Figure 4.2: Two Na-fluorohectorite samples of the apr batch in 10^{-3} M NaCl solutions demonstrate that their gravitationally induced phase separation is highly reproducible.

Sedimentation behavior in 1 mm **and** 2 mm **Mark tubes**

Figure 4.3 shows the sedimentation behavior of a 3w/w% Na-fluorohectorite sample held in a 2 mm Mark tube. A brownish-white sediment becomes visible to the naked eye during the first few hours of sedimentation, and during the first days, speckles that appear faintly bright between crossed polarizers appear in the middle of the capillaries. During the first week of sedimentation a second, gel-like and cloudy phase immediately above the sediment becomes visible to the naked eye while the birefringent speckles grow brighter. There are extensive dynamics in the birefringent region as the speckles sediment and in a matter of one to two weeks form a well-defined layer on top of the isotropic gel-like region and the sediment. The ordered character of this birefringent phase has been previously demonstrated also through anisotropic x-ray scattering patterns [18] and by diffusion MRI imaging [10], showing how the clay platelets of this phase are standing with their face normals oriented on average perpendiucular to the gravitiational force. Above the birefringent phase there exists a cloudy region that disappears on timescales of approximately two weeks. The upper part of the samples are cloudy right after preparation but after a few hours become clear to naked eye observations and dark between crossed polarizers, indicating an isotropic state. About three weeks after sample preparation, a second birefringent layer precipitates out of this isotropic phase to form

a new phase atop the standing nematic. This new, more slowly forming phase is visibly different from the first birefringent phase both to the naked eye and especially when viewed between crossed polarizers with the polarizer and analyzer axes at respectively $-45°$ and $45°$ with the vertical. A narrow boundary layer between the two birefringent phases is in most cases visible and some investigations indicate that the particles in this layer are lying with their face normals parallel with the gravitational field [31, 59]. It is believed that phase boundaries act in much the same way as a wall, imposing homeotropic alignment of the clay platelets with respects to the interface plane – a feature that has also been observed in dispersions of gibbsite platelets suspended in toluene [72]. In many of the 2 mm samples however, the boundary layer between the two birefringent phases is either isotropic or appears to have a slanted orientation.

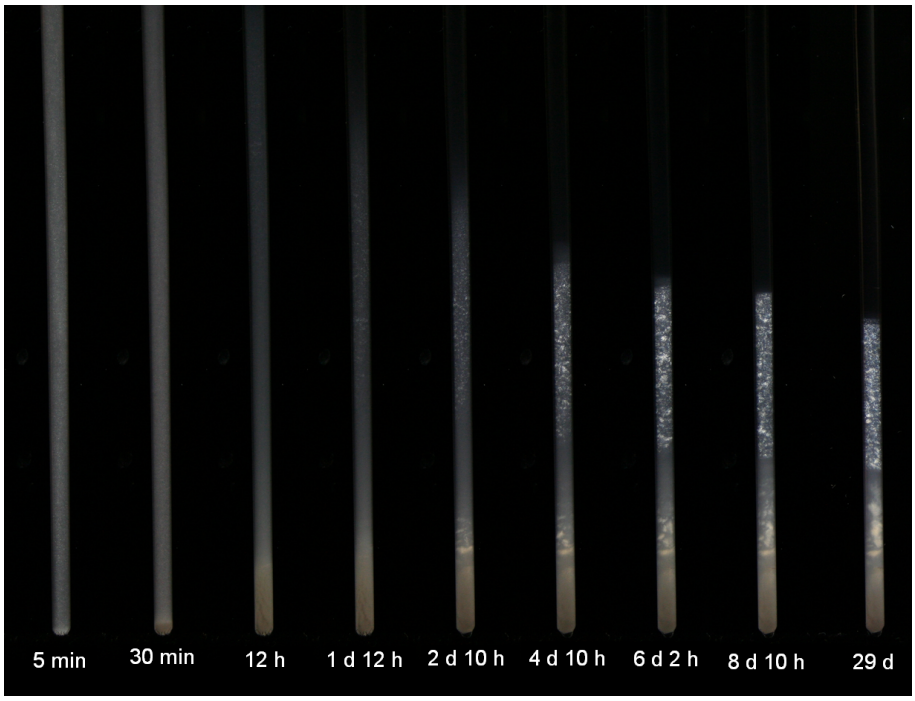

Figure 4.3: Picture series taken between crossed polarizers of a typical sedimentation process in a 3w/w% Na-fluorohectorite sample in 10^{-3} M NaCl solution. The sample was number 7.5 held in a 2 mm Mark tube.

Boundaries

As already mentioned, the presence of boundary layers between the standing nematic and the isotropic gel immediately below it have recently been observed in fluorohectorite dispersions [31, 30]; similar phenomena have also been observed by van der Beek et al. in [72] for suspensions of gibbiste platelets in toluene. Figure 4.4 shows the presence of a corresponding boundary region between the second nematic and upper isotropic phases in the 1 mm Na-fluorohectorite Mark tube sample m.1. The birefringence from the boundary layer is extinguished when the polarizers are in the 90° position with respects to the long capillary axis, whereas it is very bright when the polarizers are in the 45° position. From the discussion of section 2.3.3, this indicates that the particles in the boundary layer are standing up or lying down. Because the appearance of the boundary layer was found to change little when the sample was rotated around it's long capillary axis, it is shown that the face down configuration is the correct one. It is thus illustrated that the homeotropic-like orientation with respects to a phase boundary observed in [31, 30, 72] can occur also between the second nematic phase of fluorohectorite dispersions and the isotropic phase immediately above it.

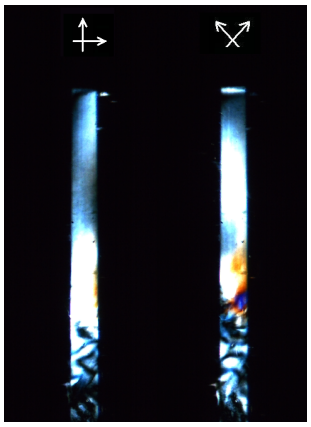

Figure 4.4: Photographs of sample m.1 between crossed polarizers. In the rightmost image the polarizers' axes make an angle of approximately 45° with the long capillary axis and a narrow boundary region between the second nematic and isotropic phases is clearly visible.

Figure 4.5 shows images taken between 90° crossed polarizers of aged Na-fluorohectorite dispersions held in 1 cm diameter glass capillaries. In addition to prominent birefringent textures, it is seen that at a given depth, all the photographed samples transitions from a clear to a cloudy state. The transition was also visible when the samples were viewed without crossed

polarizers. It is interesting to note that the prominent and colored birefringent textures carry over from the clear to the cloudy regions in a fashion seemingly undisrupted by this change in optical properties. In order to investigate the thixotropic behavior of the samples, one of them were tilted upside down, and observed as a relatively large air bubble present in the upper parts of the sealed capillaries rose against gravity through the phases present. All observed phases were thus determined to be of a more viscous nature than pure water samples, and an especially slow movement of the air bubble was seen through the cloudy regions. With the currently unresolved status of clay gels in mind, it is interesting to note that even highly viscous phases of Na-fluorohectorite platelets display a marked birefringence. Whether the birefringence in clay gels really reflects a true Onsager-like transition to the nematic state, is however unclear [24].

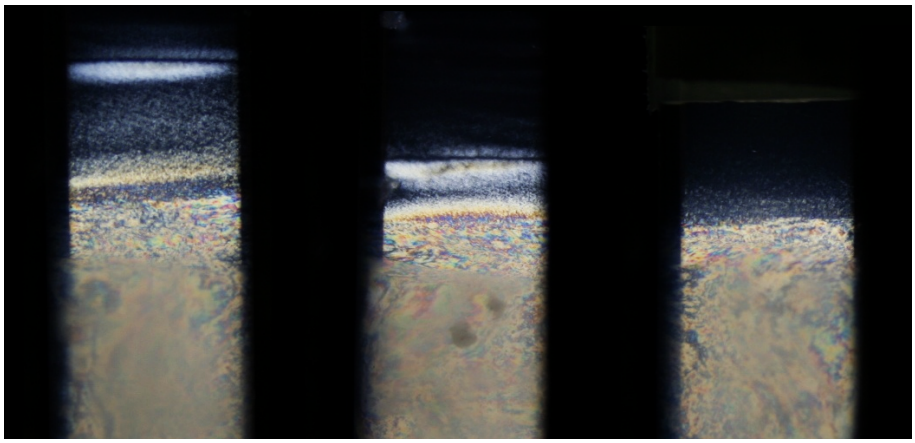

Figure 4.5: Images between 90° crossed polarizers of aged and strongly gelled Na-fluorohectorite dispersions held in thick glass capillaries approximately 1 cm in diameter. The samples were prepared by D.M. Fonseca more than a year before the images were taken. In all three images a marked transition from a clear to cloudy appearance is seen. Interestingly, the nematic structure carries through from the clear to the cloudy regions in a continuous fashion.

4.1.2 Li-fluorohectorite

Figure 4.6 shows a set of images taken between crossed polarizers of sample 16.v. Already in the first image, taken approximately 5 min after the dispersion was filled into the flat rectangular sample holder, the sample is markedly birefringent and has a grainy texture, indicating that ordered regions likely grow by a so-called nucleation and growth process. After two hours the upper parts of the dispersion is less birefringent and faint vertical striped features are visible, similar to those observed by Ringdal [59] in Na-fluorohectorite dispersions. After twelve hours a marked horizontal boundary exists between the sedimented regions and the upper regions from which fall-out is still seen to occur. After about five days, markedly birefringent regions are present above the large sedimented bottom phase. After eight days, tactoids from the upper parts of the sample are still sedimenting and contributing to the growth of the smaller domain dominated nematic phase.

4.1.3 Ni-fluorohectorite

Figure 4.7 shows a picture series of the sedimentation behavior of a 2 mm Ni-fluorohectorite Mark tube sample. The sample is visible between crossed polarizers, but does not show any birefringent textures or grains. It is likely that diffuse light scattering similar to that seen from the sedimented regions of normal Na-fluorohectorite samples, is the reason why this sample is visible between crossed polarizers. The faintly green hue of the sedimented regions are due to the color of the Li-fluorohectorite itself, which is lightly sea green, as seen in Figure 4.1.

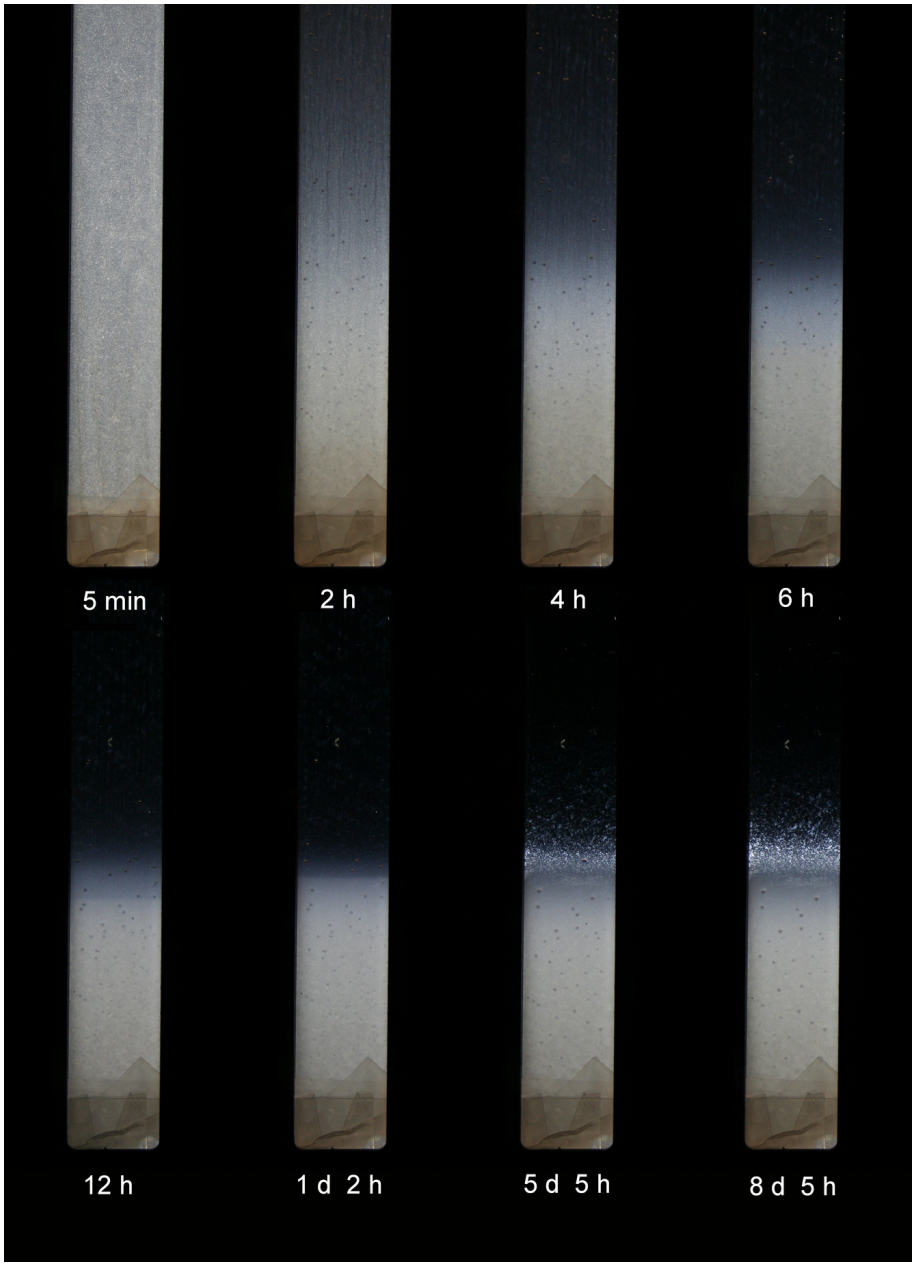

Figure 4.6: Picture series taken between 90° crossed polarizers of the sedimentation behavior of Li-fluorohectorite sample 16.v.

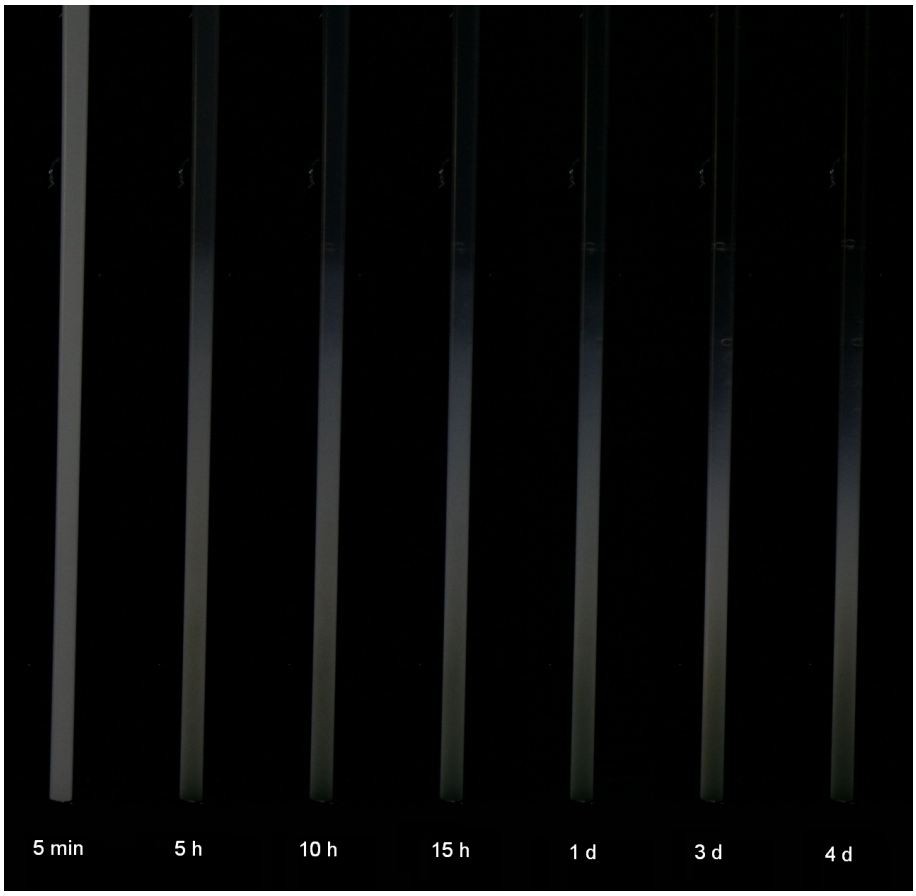

Figure 4.7: Picture series taken between 90° crossed polarizers of the sedimentation behavior of Ni-fluorohectorite sample 18.1.

4.1.4 Flow birefringence and dynamic boundary effects in large sample containers

Figures 4.8 and 4.9 shows images of flow birefringence induced in the isotropic upper phases of large sample containers of 3w/w% Na-fluorohectorite dispersions, approximately six weeks old. The sample in the first figure was tilted over and shows a marked birefringence pattern which decays on timescales of a few seconds. Interesting boundary effects are visible in the images of

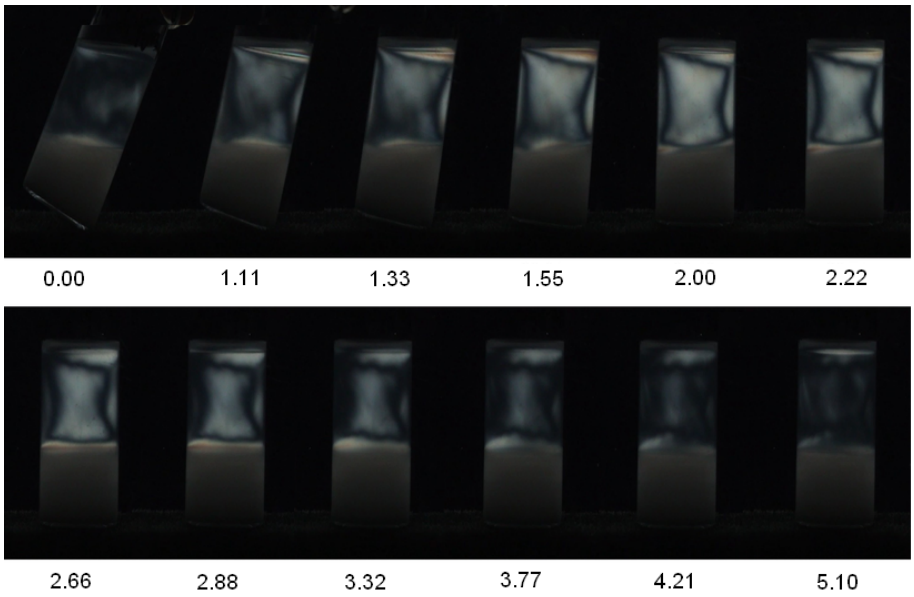

Figure 4.8: Flow birefringence in a large sample container 3 cm in diameter. The sample was an approximately six weeks old 3w/w% Na-fluorohectorite dispersion of electrolyte strength 10^{-3} M. The upper parts of the sample were originally completely dark between crossed polarizers. As the birefringence decays, marked bounday effects are visible as vertical and horizontal black stripes. The times are given in seconds relative to the first frame shown.

Figure 4.8. It appears that the boundary between the denser, white phase and the flow birefringent phase, as well as the dispersion-air interface, affect the orientation of the dispersed platelets in manners similar to the container walls. Marked dark regions are seen to propagate from these boundaries inwards. The regions can either be dark because they are isotropic, or they can be dark due to the specific director orientations imposed by the boundaries. If the latter is true, the fluorohectorite particles in the marked dark regions are either lying flat down or standing up, with their optical axes oriented in the image plane or perpendicular to it. By comparison with

the Michel-Lévy chart shown in Figure 2.12, the dominant color of the flow birefringent region of the tilted sample corresponds with first order gray. The presence of flow birefringence indicates that after six weeks of gravitational sedimentation, a marked amount of Na-fluorohectorite particles are still dispersed in the suspension.

Figure 4.9 shows a birefringence pattern induced by relatively vigorous shaking of an 3 cm in diameter glass tube containing Na-fluorohectorite; also approximately six weeks old. It is seen that some of the denser phase has been disturbed by the shaking. In contrast to the images shown in Figure 4.8, the current sample is highly colorful, and again demonstrates the presence of dispersed particles. The increased birefringence relative to that observed in Figure 4.8 might be attributed to the stronger agitating forces applied to the shaken sample.

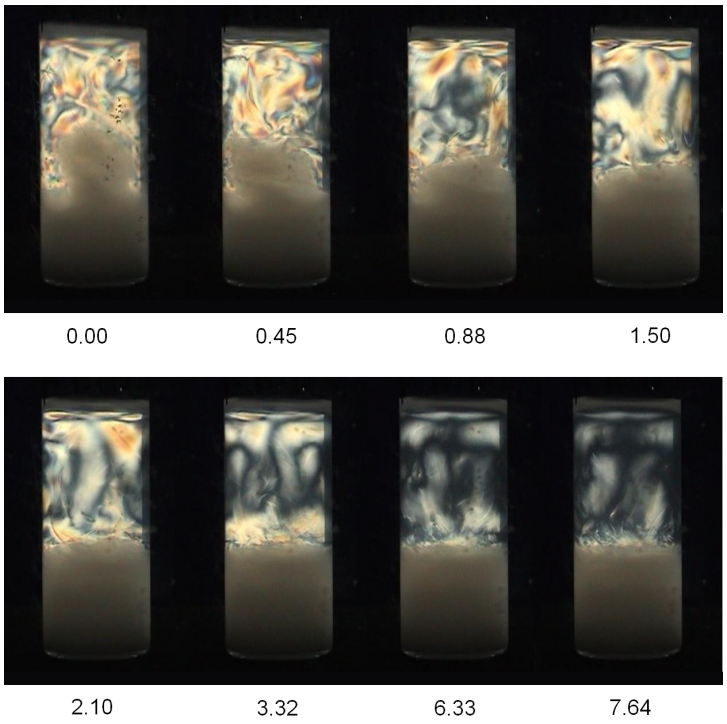

Figure 4.9: Strong and colorful flow birefringence induced by shaking of a 3 cm in diameter Na-fluorohectorite sample. The times are given in seconds relative to the first frame shown.

4.2 Investigations on phase stabilization

The phase behavior of colloidal clay suspensions in the gravitational field is of fundamental interest and could have practical analogies to the behavior of clay deposits subjected to varying salinity conditions. However, with regards to practical technological applications of liquid crystalline clay suspensions the issue of phase stability arises. It can easily be imagined that, if for instance an LCD screen consisted of a strongly sedimenting phase, this would be problematic. This section therefore concerns attempts at drawing and isolating separate phases from the gravitationally settled Na-fluorohectorite samples of one of the larger containers. From a fundamental as well as from a practical point of view, it is interesting to see if such isolated samples either show further sedimentation in a manner similar to the original samples, in a differing manner, or perhaps in some cases show no significant sedimentation behavior at all. The latter can be thought to occur for samples that for instance are strongly gelled so that the sedimentation would be hindered by a possibly partially arrested particle arrangement.

To prepare single phase samples of Na-fluorohectorite, six batches of 1.5 ml each were successively drawn from the top down of the three weeks old sample 5 and labeled respectively as x5, y5, z5, æ5, ø5 and å5. After å5 the next attempt at extracting a sample proved difficult to draw into the syringe, indicating its strongly gelled character, and hence no more samples were drawn after å5. The different drawn samples were filled into 2 mm Mark tubes and left standing in the gravitational field for several weeks. Optical photographs of the samples taken eight weeks after they were placed in the Mark tubes are shown in figures 4.11 and 4.12. Photographs of the same samples taken immediately after preparation were completely devoid of birefringence in the case of the x5, y5 and z5 samples whereas, as illustrated in Figure 4.10, the samples drawn from the lower phases exhibited strong flow birefringence.

The Mark tubes containing samples x5, y5 and z5 drawn from the topmost phase of the (partially) settled sample 5 were completely devoid of birefringence a few minutes after preparation. However, in the eight weeks old samples a small region at the very bottom of the Mark tubes has become bright between crossed polarizers for all these samples, as shown in Figure 4.11. This could be expected in light of the flow birefringent properties discussed in the previous section, which demonstrated that several weeks old large container samples still contain significant amounts of dispersed particles. With regards to texture, the phases observed in samples x5, y5 and z5 are similar in appearance to the second birefringent phase that is usually seen to precipitate out of the isotropic phase of the Na-fluorohectorite Mark tube samples approximately three weeks after preparation. The x5 Mark tubes stand out by seeming to have less texture which might be indicative of larger domain formations. A notable feature is the color of the birefrin-

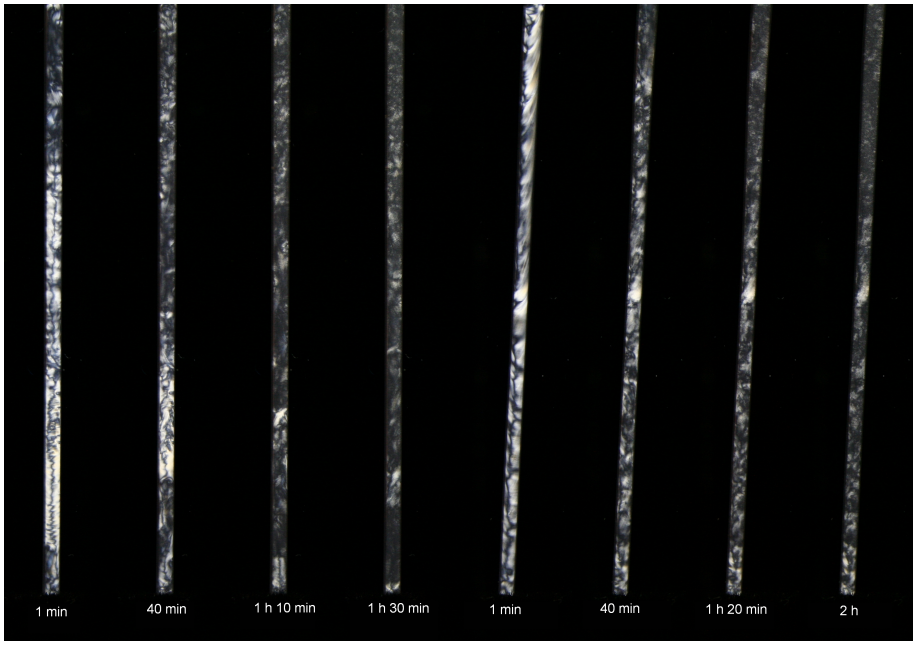

Figure 4.10: Mark tube samples ø5.III and ø5.VI, drawn from the upper phase of the three weeks old Na-fluorohectorite sample 5, photographed immediately after they were filled into the capillaries.

gent phase of the x5, y5 and z5 samples which appears to be more green compared with the usually bluish color of the newly formed second birefringent phase for samples y5 and z5 whereas sample x5 is more yellow. From the Michel-Lévy chart presented in Figure 2.12, it is seen that the a change from blue to green to yellow corresponds with the expected color sequence for retardations Δnl that correspondingly increase. Under the assumption that the observed colors for samples x5, y5 and z5 are of first order, the corresponding retardations would be of between 650 nm and 850 nm, with reference to the Michel-Lévy chart shown in Figure 2.12. With a sample thickness of $2.00 - 2 \cdot 0.01$ mm $= 1.98$ mm, the corresponding birefringence Δn obtains values of between $3.3 \cdot 10^{-4}$ and $4.3 \cdot 10^{-4}$.

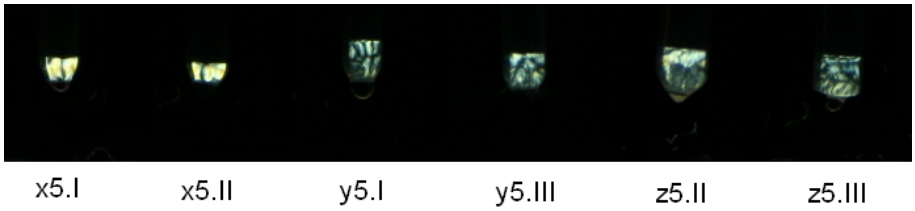

Figure 4.11: Mark tube samples, drawn from the upper phase of the three weeks old Na-fluorohectorite sample 5, photographed eight weeks after preparation.

A second glance at the DLVO-plots that were presented in Figure 2.3 in section 2.2.2, could shed some light on the apparently less textured character of the x5 samples, which were drawn from the topmost parts of the partially settled original dispersion. From this plot it is seen that clay platelets consisting of relatively fewer stacks are in general expected to be more overall repulsive than platelets consisting of many unit layers. Because platelets that are overall repulsive do not show the nucleation and growth processes which are expected for platelets whose interaction potentials display secondary minima, the presence of smaller-stack particles in sample x5 could be the reason for it's slightly less textured appearance. The presence of such smaller stacks in the upper parts of a partially sedimented dispersion is supported by the results of section 2.2.1, where it was shown that particles with smaller volumes sediment more slowly. It is however important to note that the hypothesis that smaller particle stacks are present in the topmost regions of partially settled samples is a tentative one, which is strongly reliant on the applicability of the results obtained in the DLVO-potential discussion of section 2.2.2.

Figure 4.12 shows æ5, ø5 and å5 samples eight weeks after preparation. It is clear, also in comparison with the images of Figure 4.10, that some sedimentation or setteling has occurred in these samples. However, none

of the Mark tubes show an actual sediment but rather an isotropic bottom phase, visible in Figure 4.12 for samples ø5.V and å5.III. It is likely that this phase corresponds with the isotropic gel-like regions normally observed in 2 mm Mark tube samples of Na-fluorohectorite right above the sediment. To explain the lack of an actual sediment it is necessary to try assess what separates these drawn Mark tube samples from a usual Na-fluorohectorite sample. The most obvious feature might be related to size fractionation in the gravitational field; a feature already briefly discussed in relation to the x5 samples. According to Equation 2.2 the terminal velocity of a particle in water at standard gravity is proportional to the particle volume divided by its Stokes equivalent radius. In the gravitational field, particles of equal mass density hence will be size fractionated because the larger particles with a larger volume-to-radius ratio will sediment faster. In addition, Brownian motion further hinders the sedimentation of the smallest particles. It is likely that by drawing samples from an already (partially) settled Na-fluorohectorite dispersion, the largest particles present in the original dispersion are excluded as they remain in the sediment and the lower gelled phase (which were not included in the drawn samples).

However, this discussion raises the question of whether only the largest clay particles form true sediments. It can be envisioned that, as gravitational setteling progresses, the transition to a sedimented phase occurs at a particle concentration which is higher than the concentration limit for gelling which again, as seen in for example Figure 4.12, is higher than the critical concentration for the isotropic to nematic phase transition. This behavior has essentially been established in phase diagrams for water-dispersed Na-fluorohectorite in [16]. It might also be possible that the speed of settling affects the resulting particle arrangement. According to Equation 2.2 the particles with the largest volume-to-radius ratios have the highest terminal velocities. This means that setteling into the initial sedimented phase of the usual Na-fluorohectorite samples happens at a much faster rate than for example setteling into the second birefringent phase. This effect has been clearly observed, as for example during the gravitational setteling of Na-fluorohectorite in 2 mm Mark tubes, see Figure 4.3, where the sediment forms an approximately 1 cm high region in a matter of hours, whereas growth into for example the second birefringent phase happens at much slower rate of only a few mm per month. Because gelling is a time dependent phenomenon, where the arrested gel structure develops over the course of hours or even days or more, it is possible that the more rapidly setteling large particles of the usual Na-fluorohectorite dispersions do not have time to form extended structures as they settle out of solution (provided that extended structures are indeed a term characterizing the gelled state - this is currently not known). Later on, gel formation might be prevented when the particles of the sedimented phase are densely packed so that the degrees of motional freedom here are fewer than in the dispersed phase and a transition

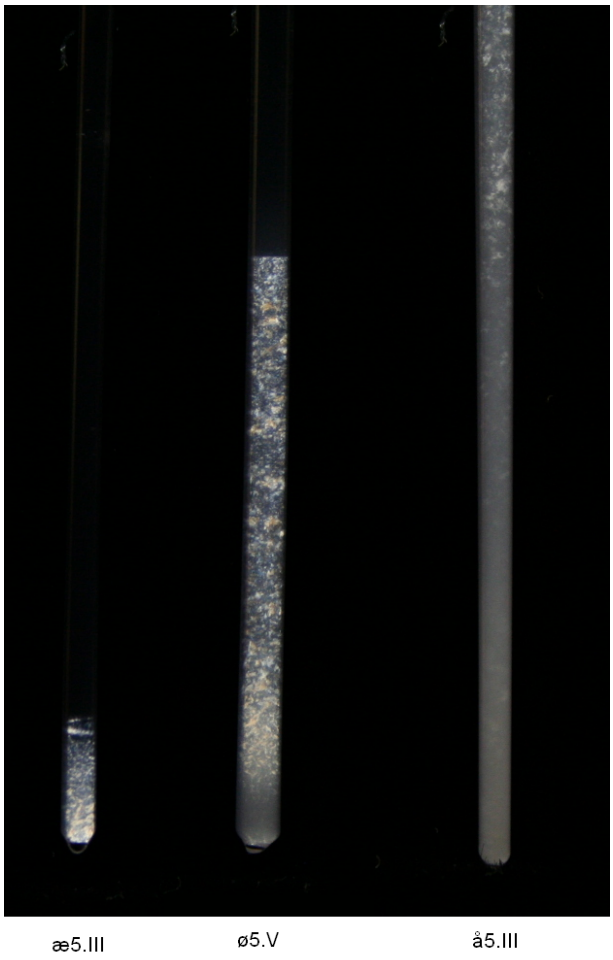

Figure 4.12: Mark tube samples, drawn from the lower phases of the three weeks old Na-fluorohectorite sample 5, photographed eight weeks after preparation.

to the gelled state is not possible. This might shed some light on the lack of sediment formation in the drawn capillary samples because here the largest particles with the most rapid terminal velocities are no longer present and thus a gelled phase is seen to form the bottom part of the capillary samples.

4.3 True uniaxial nematic order observed in evaporating capillary samples

As briefly discussed in section 2.2, evaporation may be used as a phase shift inducing factor in colloidal liquid crystal dispersions. Evaporation may occur in cooperation with a gravity induced concentration gradient or, in samples where the colloidal species have a density approximately equal to the solvent, evaporation may be the only contributing factor leading to phase separation. The samples prepared in this project were not initially intended to undergo evaporation. Some samples were however less effectively sealed than others, so that slow evaporation was seen to occur on timescales of several weeks. By chance, this evaporation led to the discovery of a new birefringent region at the top of the evaporating samples, exhibiting a strong rainbow-like optical spectrum between crossed polarizers.

Optical birefringence observations

Figure 4.13 demonstrates the existence of this phase in the 1 mm Mark tube sample 3.14. When the crossed polarizers are in the 90° position with respect to the long capillary axis, the sample appears similar to usual, non-evaporated Na-fluorohectorite samples except for the fact that there is no upper dark isotropic phase present due to the evaporation. But when the polarizers are rotated to a 45° tilt, the upper birefringent phase shows a striking color spectrum, ranging from red via green and blue to a final purple. Figure 4.14 demonstrates the presence of the same colored region in sample 3.3 and shows how this phase is at its definite brightest with the polarizers in the 45° position. From the discussion of section 2.3.3 this indicates that the director is oriented along either the vertical or the horizontal and that the particles are thus either lying face down or standing. As discussed in section 2.1.1, previous studies have demonstrated that the majority of Na-fluorohectorite particles in the main birefringent phase are indeed standing, but with their face normals (or more correctly the projections of their face normals) semi-randomly distributed in the horizontal plane, with an orientational distribution that likely depends upon the distance from the aligning walls. Because the new nematic phase observed in the evaporated samples appears considerably brighter and more homogeneous between crossed polarizers compared with the usually observed standing nematic, it seems possible that the particles in this region have adopted a face down config-

uration, effectively increasing the order since rotation around the nematic director now no longer changes the platelet orientation. If this is indeed the case, the colored region of the evaporated samples presents a new form of extended nematic arrangement in suspensions of Na-fluorohectorite, where the director now coincides with the platelets' face normals.

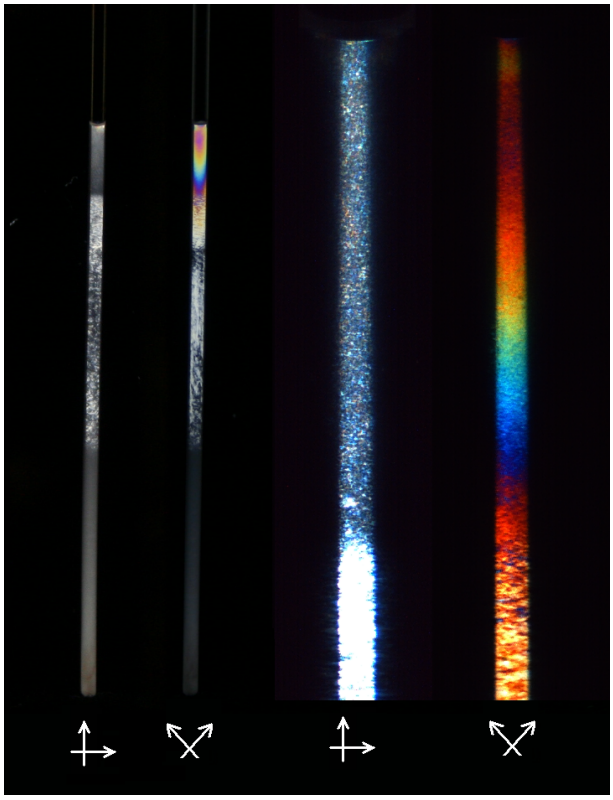

Figure 4.13: Photographs of sample 3.14 after slow evaporation to a little more than half the original volume had occurred over the course of approximately two months. The orientation of the polarizers with respects to the long capillary axis is indicated in the figure. The exposure time was significantly reduced in the images where the polarizers were at a 45° tilt with respect to the long capillary axis, since the striking color variations here were at their brightest and most well defined. With the crossed polarizers at 90°, the color spectrum is hardly visible.

There are two particularly interesting optical characteristics of the colored phase, the first being the colors themselves, which correspond well with those presented in the Michel-Lévy chart of Figure 2.12 for a retardation Δnl continuously decreasing with sample depth from a reference position at

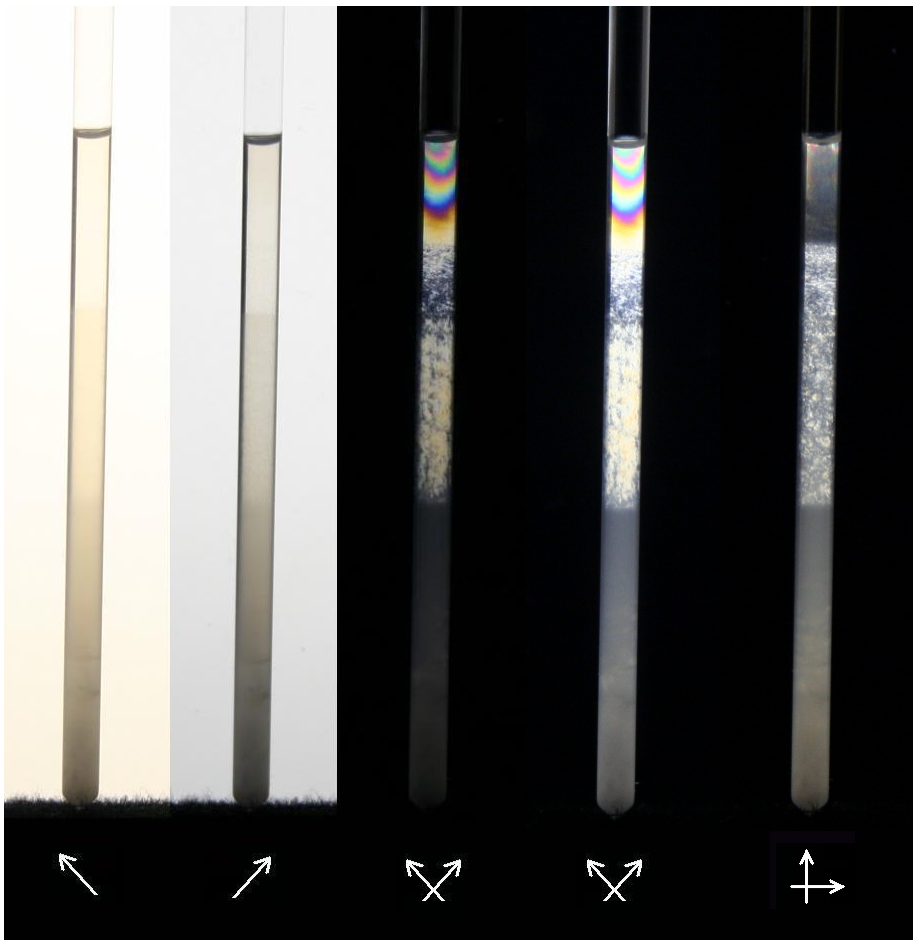

Figure 4.14: Photographs of sample 3.3 after slow evaporation to about half the original volume had occurred over the course of approximately two months. In the leftmost image only the analyzer is present, tilted at a 45° angle with respects to the long capillary axis. The second picture from the left shows the similar situation where only the polarizer is present at a 45° tilt. The striking colors of the third and fourth images from the left only appear when the sample is viewed between polarizers. In the two rightmost pictures, the exposure time was increased and kept at a fixed value for both the 45° and 90° orientations.

the dispersion-air interface[1]. Since the light path l through the sample is proportional to the capillary thickness, which can be presumed a constant function of the height except for at the very top and bottom of the capillary, a decreasing retardation with sample depth indicates that the birefringence Δn decreases. A second notable property of the colored phase, especially noticeable in Figure 4.14, is the curved appearance of any given monochrome region. This curve could be thought to follow the shape of the dispersion-air meniscus or even to reflect wall anchoring, but a closer look at Figure 4.14 reveals that this is not the case. A more likely explanation takes into account the curved shape of the Mark tube capillaries themselves, which causes the light path through the edges of the sample to be considerably shorter than that through the center of the capillary. It is seen that the sequence of colors observed for instance in Figure 4.14 upon going from the center of the capillary and outwards, corresponds with a decreasing retardation. This decrease is thus attributable to the diminishing light path encountered as one moves further and further from the center of the capillary and finally encounter the capillary edges.

Values of the birefringence Δn can be obtained from the observed colors of the evaporated samples. Considering the images of sample 3.3 in Figure 4.14, the first observed color, going from the bottom upwards, is a straw-yellow hue followed by a dark magneta and blue. Comparing these colors with the Michel-Lévy chart of Figure 2.12, it is seen that they correspond with first order retardations ranging from around 250 nm to 600 nm. The subsequent colors range in a continuous fashion from this first order magneta to third order magneta, and to the green retardation successing it; the latter has a retardation of about 1800 nm which, under the assumption of a sample thickness l of $2.00 - 2 \cdot 0.01$ mm $= 1.98$ mm, corresponds with a birefringence $\Delta n = 9.1 \cdot 10^{-4}$. There could be several explanations for the high birefringence observed close to the dispersion-air interface relative to that observed at larger sample depths. According to Strobl [69], both the birefringence Δn as well as the total diamagnetic susceptibility anisotropy $\Delta\chi_{tot}$ of the dispersion, are proportional to the nematic order parameter S_2 of a uniaxial nematic. This assumes all regions of the nematic phase consists of nematogens of equal anisotropic properties. The total diamagnetic susceptibility anisotropy in this case denotes contributions both from the anisotropy of each individual nematogen platelet as well as the contribution attributable to their relative order with respects to each other. For polydisperse fluorohectorite dispersions however, it is seen that both an increase in the order parameter as well as an increase in the diamagnetic susceptibility for individual Na-fluorohectorite platelets, lead to an increase

[1]From the Michel-Lévy chart it is seen that a sequence of red-magneta-blue-green-yellow colors indicates a corresponding increase in retardation, whereas the opposite sequence of red-yellow-green-blue-magneta in the same manner indicates a decrease in retardation.

in $\Delta\chi_{tot}$. The most likely explanation for the decrease in birefringence with increasing sample depth relative to the dispersion-air interface, seems to be that the order decreases. This possibility is further investigated with x-ray scattering techniques in the following section. An additional contributing explanation could be that the platelet anisotropies are larger closer to the dispersion-air interface. That the increased birefringence observed high in the capillary should be attributable to higher Na-fluorohectorite densities, seems unlikely in light of previous discussions on the size-selecting properties of gravity; it is also known from previous studies on gravitationally settled Na-fluorohectorite dispersions that the clay density increases with increasing sample depth [59], as would be expected.

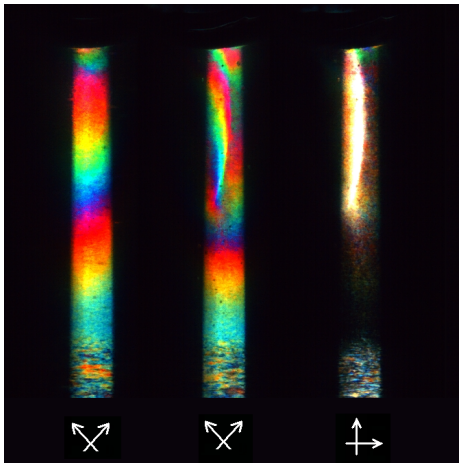

Figure 4.15: Photographs of sample 3.7 between 45° and 90° crossed polarizers, as indicated. In the middle and rightmost images the sample was rotated around it's long capillary axis relative to it's position in the leftmost image. A separate area displaying a tilted color spectrum is clearly visible in the middle image with the polarizers at 45°. In the rightmost photograph, taken between 90° crossed polarizers, this area is bright relative to the rest of the colored phase.

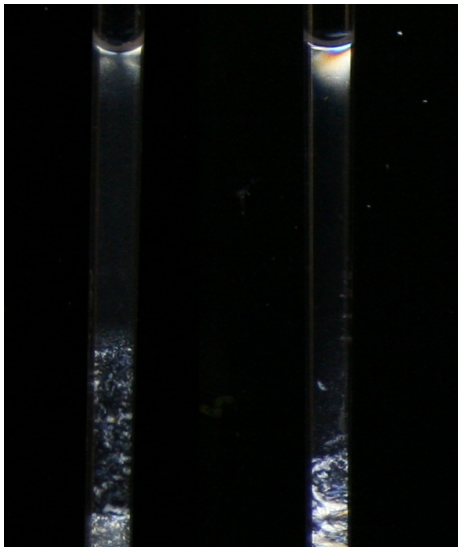

Figure 4.16: Photographs taken between 90° crossed polarizers of only modestly evaporated Na-fluorohectorite samples. It is seen that order grows from the dispersion-air interface downwards.

In-house SAXS analyses

Figure 4.17 shows the results of a SAXS scan along the long capillary axis of sample 3.14. Striking anisotropic scattering patterns with lobes fanning the vertical dominate the first few scans. The positions of these scans along the capillary axis coincide with the colored region observed between crossed polarizers in Figure 4.13. The scattering lobe orientation confirms that the vast majority of Na-fluorohectorite platelets in this phase are indeed lying face down. This is the first observation of an extended region with true uniaxial nematic ordering in aqueous suspensions of Na-fluorohectorite.

Figure 4.18 shows the azimuthally integrated intensities of the scattering images recorded from sample 3.14, as functions of the scattering vector length q for two ranges of sample depths. The reference depth of 0.00 mm is the position of the scan recorded closest to the dispersion-air interface. In this scan, as well as in the subsequent six scans reaching down to a depth of -6.00 mm, two broad-distribution peaks are clearly visible, at scattering vectors which vary with sample depth. The non-peaked intensities are seen to be proportional to q^{-2}, as expected for horizontal platelets from the plots of Figure 2.15.

Figure 4.19 shows a set of raw scattering images recorded from a vertical scan of sample 4.13. This sample had undergone further evaporation relative to sample 3.14. Notably, the scattering patterns from this sample are even more anisotropic than the patterns from sample 3.14, and especially in the

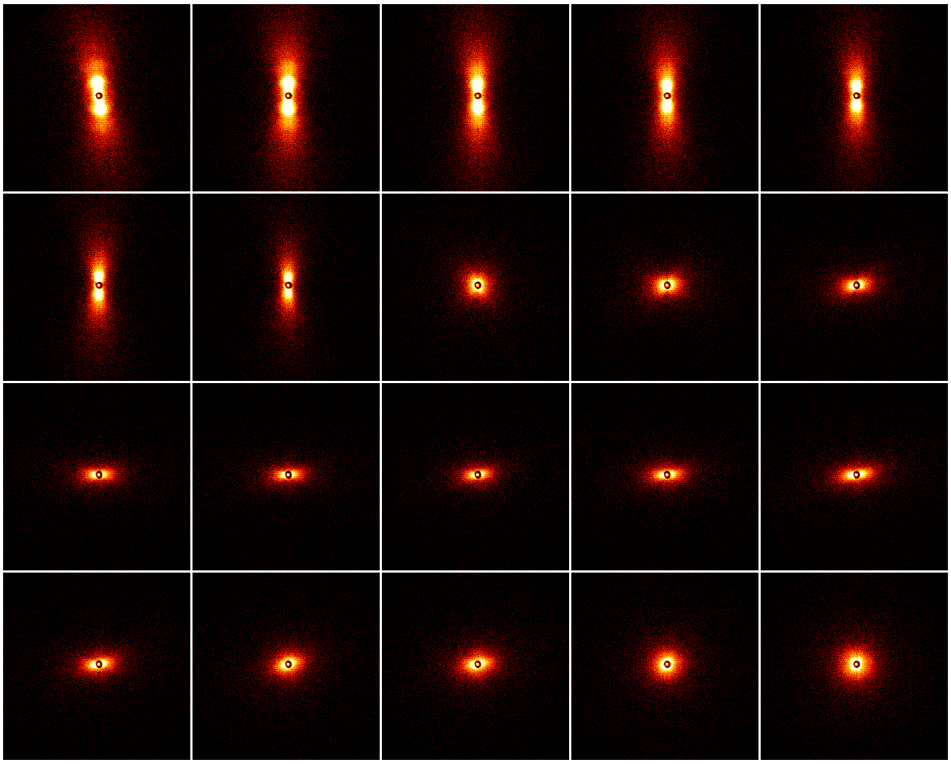

Figure 4.17: Raw SAXS data from a vertical scan of sample 3.14 at step length intervals of 1.0 mm. Each image was recorded with an exposure time of 1800 s. The image in the upper left corner was recorded close to the dispersion-air interface and shows a marked anisotropic and slightly tilted scattering pattern with respects to the image vertical, that is repeated as almost completely vertical anisotropic patterns in the subsequent six images ranging down to a depth of −6.00 mm. This vertical distance corresponds with the extent of the rainbow colored birefringent region shown in Figure 4.13. The subsequent SAXS scans show the usual anisotropic pattern of the nematic phase where the platelets are standing, followed by isotropic scans attributable to the gelled phase.

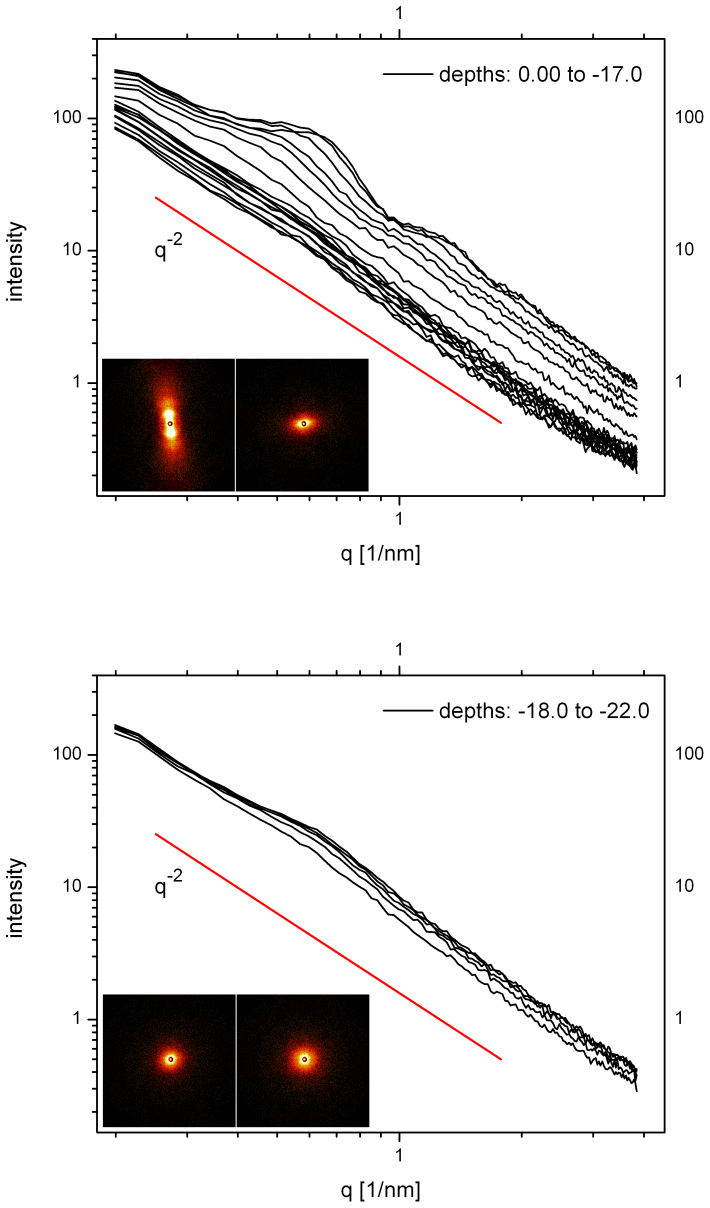

Figure 4.18: Scattered intensities from sample 3.14 as functions of the scattering vector q, plotted with logarithmic axes. The topmost image shows the intensities recorded at sample depths between 0.00 mm and -17.0 mm, whereas the bottom image shows intensities recorded between -18.0 mm and -22.0 mm. The insets show the raw two-dimensional scattering images for respectively the first and last scans included in the respective plots. The fitted line illustrates that the non-peaked intensities are proportional to q^{-2}.

first image of Figure 4.19, shapes that resemble Bragg scattering rings are visible. Figures 4.20 and 4.21 show the azimuthally integrated intensities of these scans for three ranges of sample depths. Intensity peaks whose q locations vary with sample depth are, in analogy to the peaks observed in the scattering from sample 3.14, also observed in the plots of figures 4.20 and 4.21. The peaks in the scattering from sample 4.13 are however, relative to the approximately q^{-2} shaped background, more intense than those observed for sample 3.14, and also generally appear at higher values of the scattering vector q. In order to find the precise peak positions, a q^{-2}-shaped background was manually subtracted from the intensity profiles. A representative resulting plot, at the -2.00 mm, is shown in Figure 4.22. Resulting peak locations are listed in Table 4.1.

Table 4.1: Peak centra obtained from the scattering profiles of sample 4.13. The 2nd/1st parameter is the location of the 2nd peak divided by the location of the 1st.

depth [mm]	1st peak [nm^{-1}]	2nd peak [nm^{-1}]	2nd/1st
-0.00	1.14	2.34	2.05
-0.50	1.13	2.34	2.07
-1.00	1.10	2.24	2.04
-1.50	1.05	2.12	2.02
-2.00	0.97	2.00	2.06
-2.50	0.90	1.83	2.03
-3.00	0.86	1.78	2.07
-3.50	0.83	1.77	2.13
-4.00	0.82	–	–
-4.50	0.78	–	–

It is seen that the 2nd peak is located at a q that is well approximated as the double of the q-location of the 1st peak, indicating that these peaks are (001) and (002) reflections[2]. The real-space distances corresponding with the (001) peak then spans from a value of 5.51 nm at the 0.00 mm depth to a value of around 7.57 nm at -3.50 mm. These distances reflect characterizing distances in the studied sample, and are on the order of the Debye-Hückel screening length. The possible physical meaning of these distances will be further discussed in the next section, dealing with synchrotron scattering from sample 4.13.

[2]The choice of the l-index is justified when it later becomes apparent that the small angle peaks share the anisotropy of the (001) Bragg scattering from the unit layers.

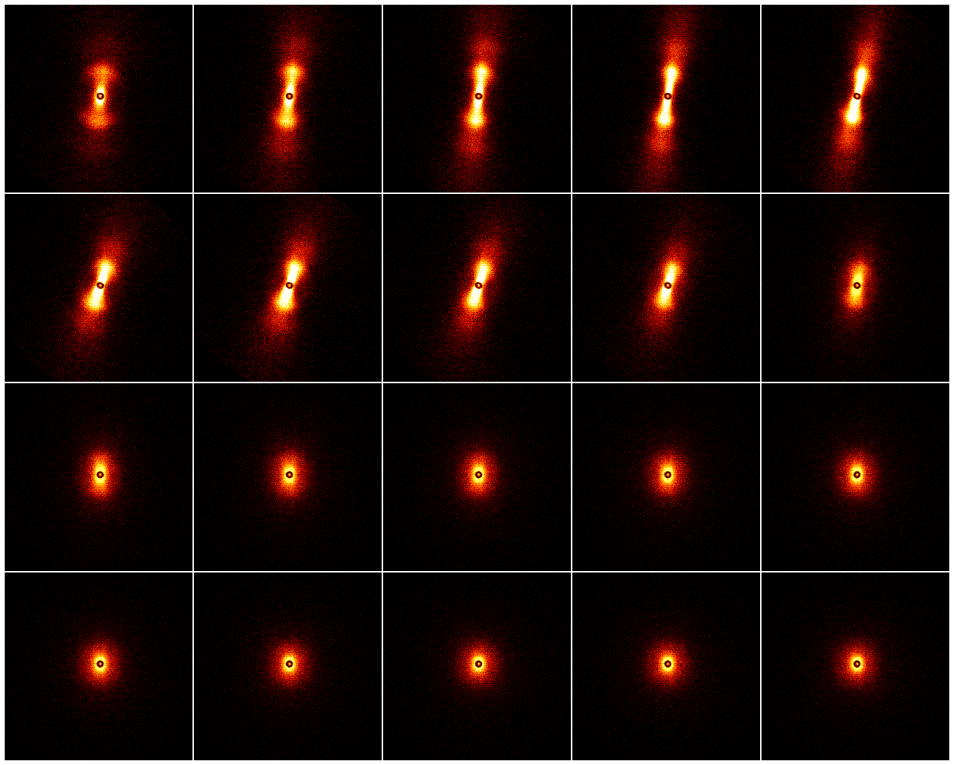

Figure 4.19: Raw SAXS data from a vertical scan of the highly evaporated sample 4.13 at step length intervals of 0.5 mm. Each scattering image was recorded with an exposure time of 1800 s. The diffractogram in the upper left corner was recorded immediately below the dispersion-air interface.

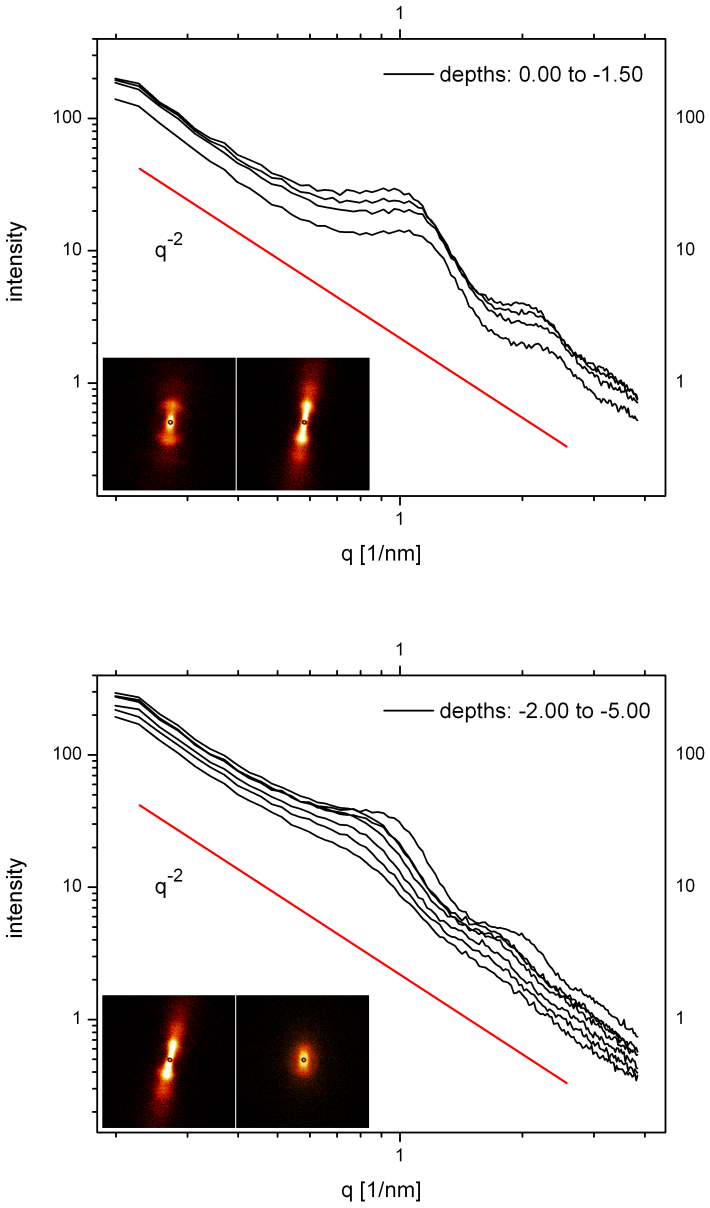

Figure 4.20: Scattered intensities from sample 4.13 as functions of the scattering vector q, plotted with logarithmic axes. The topmost image shows the intensities recorded at sample depths between 0.00 mm and -1.50 mm, whereas the bottom image shows intensities recorded between -2.00 mm and -5.00 mm. The insets show the raw two-dimensional scattering images for respectively the first and last scans included in the respective plots. The fitted line illustrates that the non-peaked parts of the intensities are approximately proportional to q^{-2}.

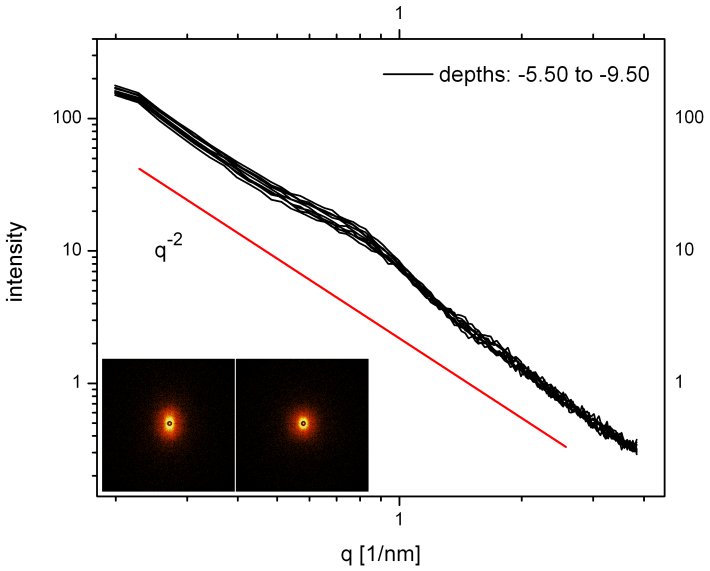

Figure 4.21: Scattered intensities from sample 4.13 as functions of the scattering vector q, plotted with logarithmic axes. The plot shows the intensities recorded at sample depths between -5.50 mm and -9.50 mm.

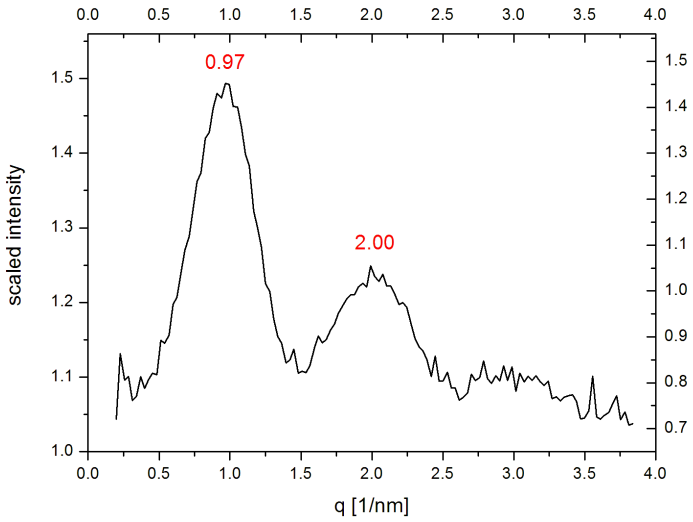

Figure 4.22: Logarithm of the background subtracted intensity from sample 4.13 at a depth of -2.00 mm.

Synchrotron studies

Figure 4.23 shows four representative raw scattering images obtained during a vertical scan of the 1 mm Mark tube sample 4.13 with a beam defining slit of dimensions 150×800 µm. Corresponding plots of the integrated intensities as functions of the scattering vector are found in figures 4.24, 4.25 and 4.26. Interestingly, it is seen that the (001) Bragg peak from the unit layer stacks, appearing at a scattering vector of 4.19 nm, grows considerably weaker relative to the small angle scattering in the scans taken higher in the sample. The raw intensity profiles recorded close to the dispersion-air interface are strikingly anisotropic. Another notable observation is the presence

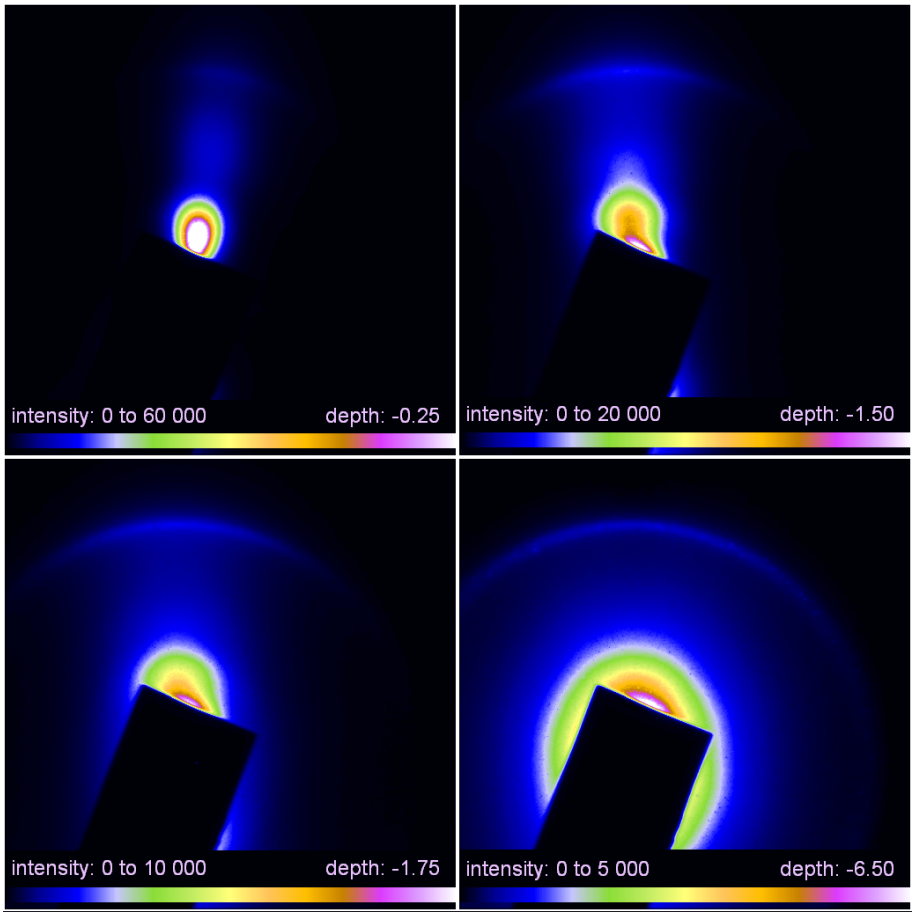

Figure 4.23: Raw scattering images recorded from sample 4.13 at four different depths. The intensity ranges spanned by the color spectrum varied as shown on the figures. Thus the green color of for instance the upper left image represents a substantially higher count than that represented by the green color of the lower right image.

of moderate speckles in the Bragg ring, in the scans taken at larger depths. The speckles are visible in the raw scattering image shown in the bottom right corner of Figure 4.23, and were observed also at neighboring depths. As previously noted, it is expected from the discussion of section 2.2.1 that the larger particles present in the initially polydisperse Na-fluorohectorite dispersions will have sedimented at a significantly higher rate than particles with smaller volumes. The above results corroborates this, as the speckles observed in the scans from the lower sample regions might be attributed to the presence of larger stacked structures. The dominance over the (001) 2wl Bragg ring by small angle scattering in the higher parts of the sample indicates that the particles in this region are spatially correlated also beyond the unit layer stacking. It is a possibility that the particles in the higher sample regions consist of considerably fewer stacked layers, this being either a feature of the original polydisperse powder itself, or the result of initially stacked particles having undergone a degree of delamination or colloidal swelling, leading to new interlayer separations in the range of the observed small angle scattering. The complete or near-complete delamination of Na-fluorohectorite particles in water suspensions has been thought not to occur due to the high layer charge density of fluorohectorites [12]. Previous studies have reported that Na-fluorohectorite particles exist as stacks of between 20 and 100 unit layers in aqueous suspensions [12]. However, since these studies were based on Bragg scattering, they are insensitive to the presence of considerably smaller stacks and even more notably, the technique does not at all see single unit layers, whose presence in the higher sample regions thus would likely go undetected. It is hence not impossible that the reported range of between 20 and 100 unit layers represents an upper bound to the number of stacks N, and that the distribution in N tails off down to the single layer state. Further investigations into the stacking polydispersity of Na-fluorohectorite dispersions might thus be prudent, especially in light of the great differences in swelling capacities observed in section 4.1 for respectively mono- or di- and trivalently intercalated fluorohectorites, which are all known to intercalate water and undergo crystalline swelling.

From both the two-dimensional scattering data of Figure 4.23 and from the plots of the integrated intensity profiles of sample 4.13, it is obvious that changes in the sample structure occur as one moves down from the dispersion-air interface. The intensities at the depths shown in figures 4.24, 4.25 and 4.26 correspond with the depths at which significant changes are seen to occur in the intensity profiles. From the obvious wandering of two broadly distributed small angle peaks with sample depth, similar to those observed with the in-house x-ray equipment, it is apparent that characterizing distances larger than the interlayer spacing of the traditional 2wl structure are present in the colored phase of sample 4.13. The most intense of these peaks is visible only at depths of 0.00 mm and -0.25 mm, and have already at the latter value peaked outside of the experimental q-range. At the depth

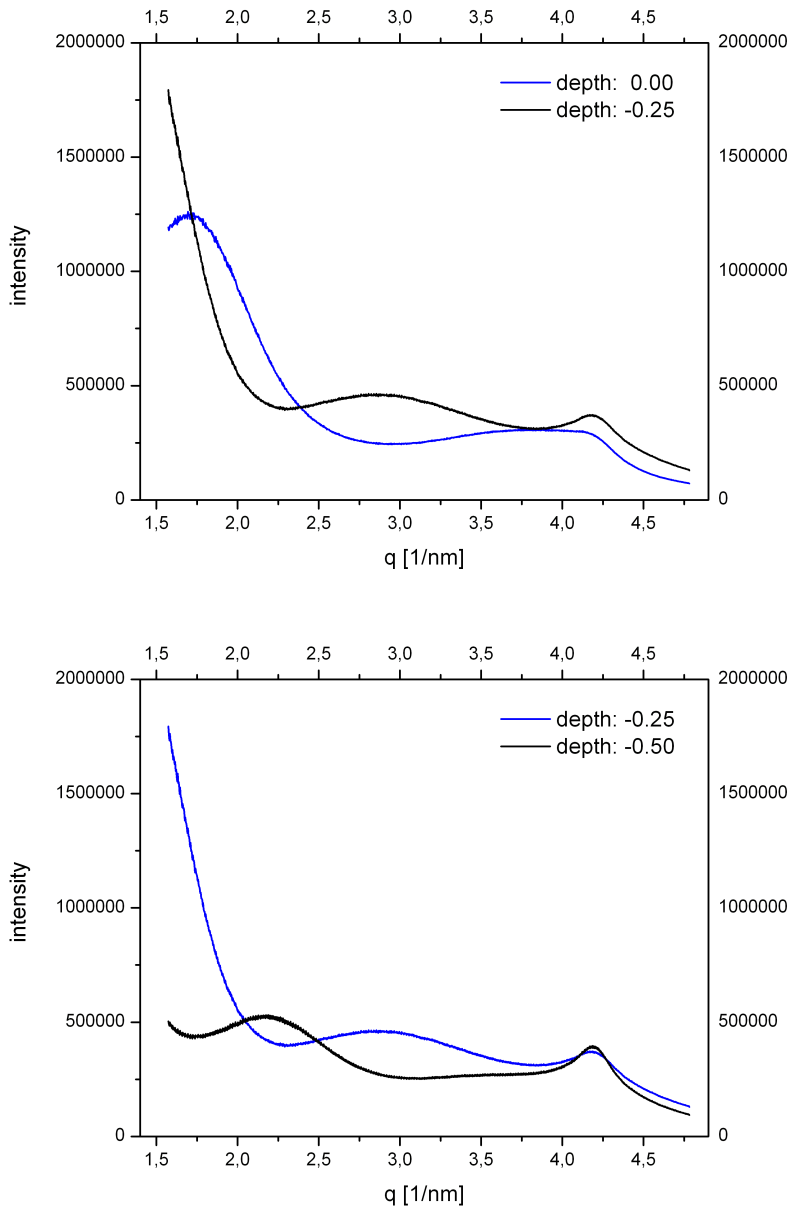

Figure 4.24: Integrated intensities from the colored phase of the partially evaporated sample 4.13. The depths are given in mm relative to the position of the first scan, which was taken at a depth of 0.00 mm, close to the dispersion-air interface.

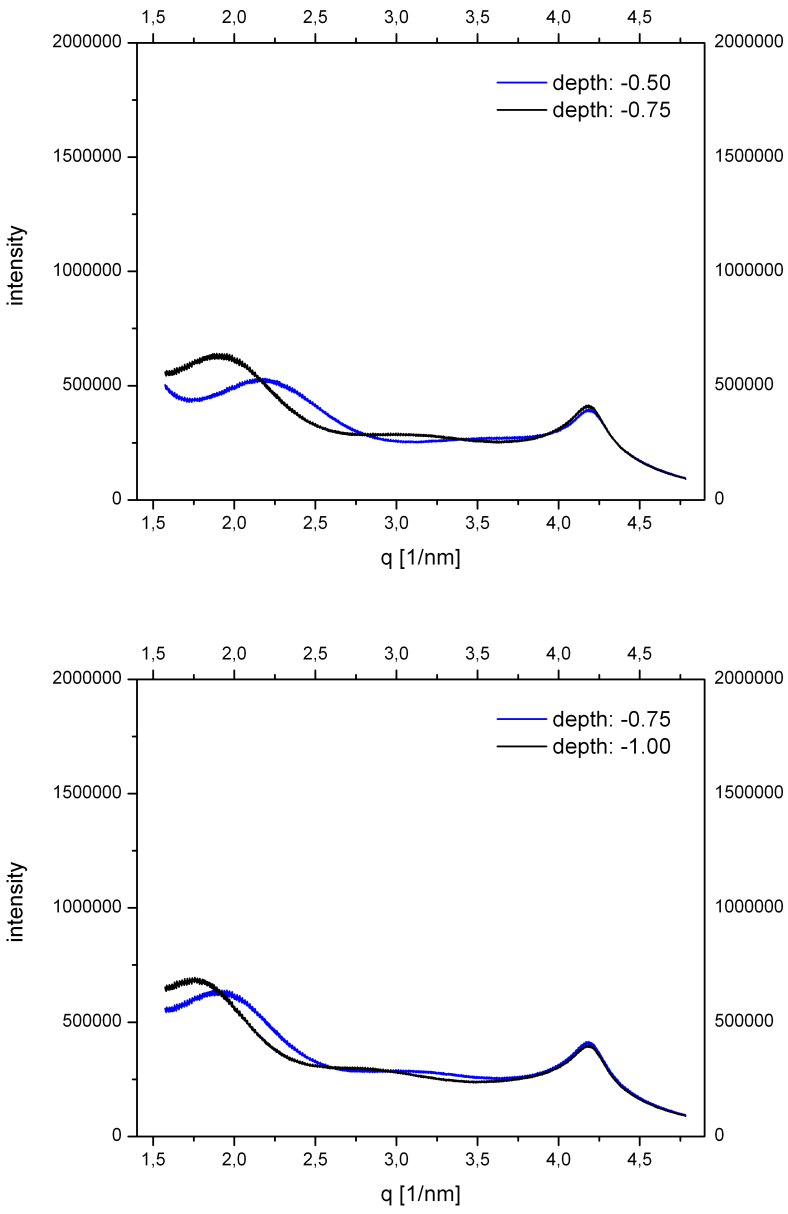

Figure 4.25: Integrated intensities from the colored phase of the partially evaporated sample 4.13. The depths are given in mm relative to the position of the first scan, which was taken at a depth of 0.00 mm, close to the dispersion-air interface.

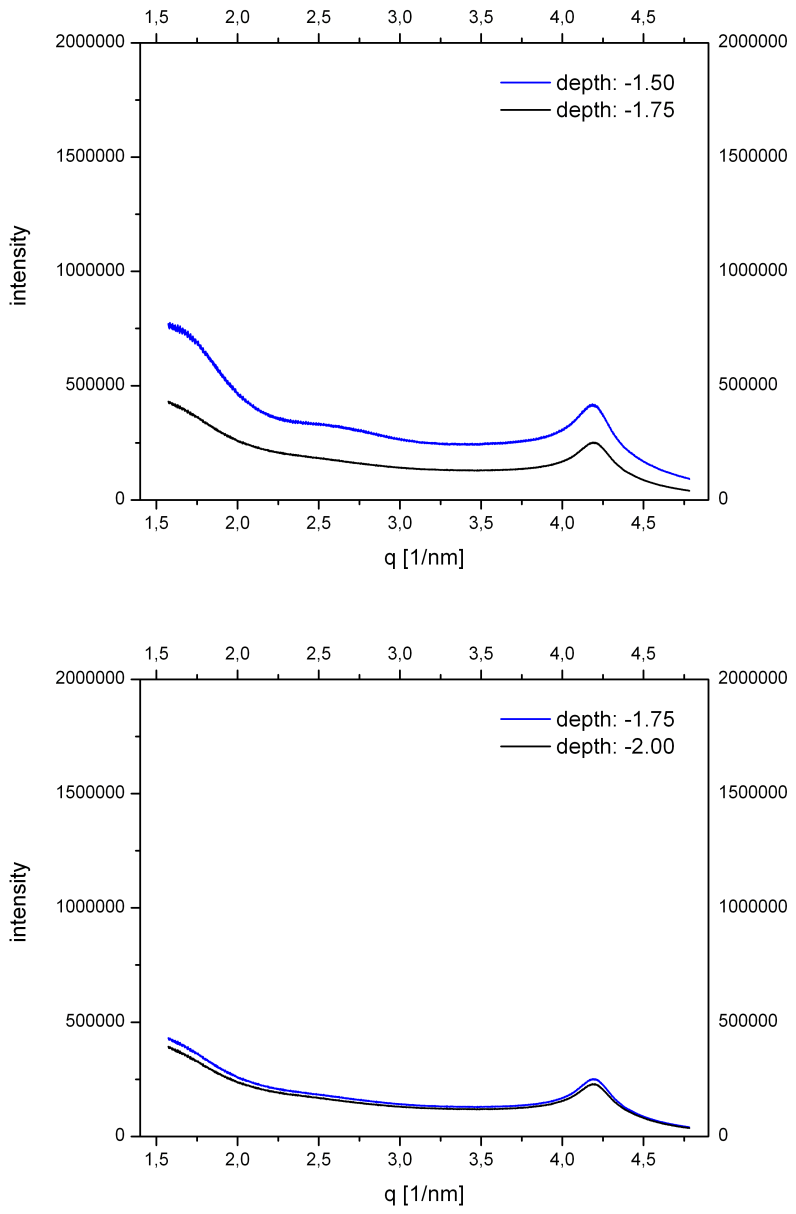

Figure 4.26: Integrated intensities from the colored phase of the partially evaporated sample 4.13. The depths are given in mm relative to the position of the first scan, which was taken at a depth of 0.00 mm, close to the dispersion-air interface.

of the reference scan however, the peak reaches it's maximum within the experimental range, at a q-value of 1.7 nm^{-1}. The second, broadly distributed peak in the integrated intensity profiles from sample 4.13 is visible for a larger range of depths, and has it's first clear peak at a depth of -0.25 mm, where it maxes out at approximately 2.9 nm^{-1}. However, already at a depth of -1.00 mm this peak has moved considerably and reaches it's maximum at a q-value of approximately 1.75 nm^{-1}. At depths of between -0.75 mm and -1.25 mm a third, very weak peak is also visible. The peak locations obtained are presented in Table 4.2, which also shows how the 3rd peak is located at a scattering vector that is approximately 1.5 times that which the 2nd peak is found at. This indicates that the 2nd and 3rd peaks could correspond to (002) and (003) order reflections. The fundamental real space separation responsible for this scattering then is seen to range from around 4.3 nm at the -0.25 mm depth, to a value of between 7.3 nm and 7.6 nm at -1.25 mm. These distances roughly corresponds with those observed for the same sample with the in-house x-ray equipment, as discussed earlier. The fact that the phase close to the air-interface now adopts even smaller particle separations might be a results of the sample having undergone further evaporation in the approximately three weeks that passed between the in-house and synchrotron scattering recordings. The observed real-space distances are, if the interpretation of these peaks as (001), (002) and (003) reflections is correct, considerably below the range of minimal inter-particle separations expected from the locations of the secondary minima of the DLVO-theory, as discussed in section 2.2.2. However, it should be recalled that the calculations of that section were based on rough estimates to critical parameters such as the Hamaker constant, and it can therefore not be excluded that the peaks seen in the scattering from sample 4.13 does reflect inter-particle separations, between the surfaces of either small or larger stacks – rather, this is the most likely explanation for these peaks. That the small angle intensity peaks originate from scattering between platelet faces is made probable by the anisotropy of these peaks, which follows the anisotropy of the 2wl (001) Bragg scattering. From the wandering of the discussed peaks towards lower q-values with increasing sample depth, it is seen that the real space correlations responsible for this scattering correspondingly increase as one moves further away from the dispersion-air interface.

Figure 4.27 shows a range of intensity profiles recorded from sample 4.13 on a log-log plot. From this plot it becomes clear that a marked change in the sample occurs upon transitioning from the -1.50 mm to -1.75 mm depth. The scattered intensity drops considerably, but then remains relatively uniform throughout the rest of the scanned series, ranging down to a depth of -6.50 mm. Figure 4.28 shows peak centra and widths found from the 2θ-integrated intensity profiles of sample 4.13. The integration over the scattering angle was limited to the range immediately surrounding the (001) 2wl Bragg ring, and the intensity profiles fitted with Gaussian dis-

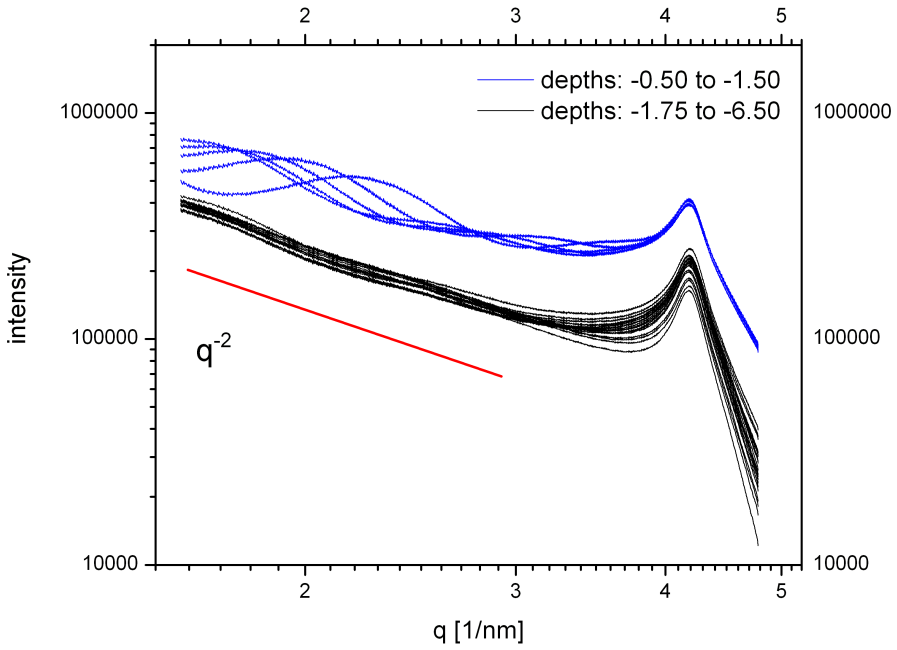

Figure 4.27: Log-log plot of integrated intensities recorded from sample 4.13 as functions of the scattering vector. Note the marked drop in the intensity between depths of -1.50 mm and -1.75 mm.

Table 4.2: Peak centra obtained from the scattering profiles of sample 4.13. The 3rd/2nd parameter is the location of the 3rd peak divided by the location of the 2nd.

depth [mm]	1st peak [nm^{-1}]	2nd peak [nm^{-1}]	3rd peak [nm^{-1}]	3rd/2nd
-0.00	1.7	–	–	–
-0.25	–	2.9	–	–
-0.50	–	2.2	–	–
-0.75	–	1.9	3.0	1.6
-1.00	–	1.75	2.7	1.5
-1.25	–	1.65	2.6	1.6

tributions. Estimated errors were output by the fitting procedure and are shown along with the data points. The topmost plot of Figure 4.28 shows how the scattered intensities at different depths peak at different values of the azimuthal angle ϕ. A general tendency of going from a tilted to a more vertical orientation is clearly visible. The second plot of Figure 4.28 shows peak widths obtained from the Gaussian fits. These widths might be used as a first approximation to assessing the order of the investigated sample; it is thus seen that, with the exception of the 0.00 mm position, the nematic order decreases with increasing sample depth. However, a more precise evaluation of the order was accomplished by fitting the scattering data with a Maier-Saupe type distribution, described by Méheust in [48]. As described in section 3.3, this fitting procedure allows for the calculation of the order parameter S_2, that was discussed in section 2.3.1 for a uniaxial nematic. Values of S_2 obtained from the scattering data recorded from sample 4.13 are listed in Table 4.3 and plotted in Figure 4.29. It is seen that close to the dispersion-air interface the order parameter adopts values between 0.77 and 0.91, that are considerably and consistently higher than the values in the range from 0.3 to 0.7 previously reported for the standing nematic phase of Na-fluorohectorite dispersions [30]. Based on Monte Carlo studies of hard and infinitely thin platelets, Eppenga and Frenkel [15] found that immediately above the isotropic-nematic transition, their system quickly attains an order parameter larger than 0.6; however, studies on nematic phases in clay gels often yields values below this, such as for instance the values of around 0.55 found by Lemaire et al. for laponite gels in [39]. Lemaire et al. compare their results with predicted values for the order parameter of between 0.7 to 0.8, explaining their relatively low value based on the possibility of topological defects in the laponite gel. Similarly, the values of between 0.3 and 0.7 obtained for Na-fluorohectorite by Hemmen in [30], as well as the

Table 4.3: Order parameters S_2 for sample 4.13 calculated from scattering data recorded at different depths. The depths are in mm relative to the position of the dispersion-air interface.

depth	S_2	depth	S_2	depth	S_2
0.00	0.77	-2.25	0.58	-4.50	0.42
-0.25	0.91	-2.50	0.56	-4.75	0.42
-0.50	0.89	-2.75	0.54	-5.00	0.40
-0.75	0.87	-3.00	0.53	-5.25	0.39
-1.00	0.85	-3.25	0.51	-5.50	0.35
-1.25	0.83	-3.50	0.50	-5.75	0.34
-1.50	0.83	-3.75	0.48	-6.00	0.35
-1.75	0.66	-4.00	0.47	-6.25	0.35
-2.00	0.62	-4.25	0.44	-6.50	0.30

lower values obtained for sample 4.13 at depths beyond -1.50 mm, could be explained by the presence of smaller nematic domains, so that the incident x-ray beam effectively averages out the actual order parameter, valid for individual domains, to a lower value. It is interesting in this respect, to observe from Figure 4.29 that the sudden jump in the order parameter down to previously reported values between depths of -1.50 mm and -1.75 mm corresponds with the marked drop in intensity noted between these depths in Figure 4.27. Because the ordered state of the face-down platelets of the colored phase correspond with the requirement for observing Bragg scattering at the detector plane, the drop in intensity with a suddenly decreasing order parameter is well understood. It is also seen from the ϕ locations of the intensity peak centra plotted in Figure 4.28, that between the two depths of -1.50 mm and -1.75 mm, the continuous clockwise tilting observed in the scattering data from the dispersion-air interface downwards, suddenly changes to a counter-clockwise tilt. Note that the decrease in the order parameter with increasing sample depth could be predicted for the evaporated samples already in the discussion of their optical properties, where the observed color changes were found to indicate a decreasing birefringence with sample depth. As mentioned in section 2.3.1, the birefringence Δn and hence also the retardation Δnl of a liquid crystalline phase is proportional to S_2. It is also worth pointing out that, based on the relatively linear relationship between the Gaussian widths found from the integrated intensities of sample 4.13 and the calculated Maier-Saupe-based order parameter, illustrated in Figure 4.30, a Gaussian analysis of the azimuthal intensity profiles likely can present a valid first approximation to the order for uniaxial fluorohectorite suspensions.

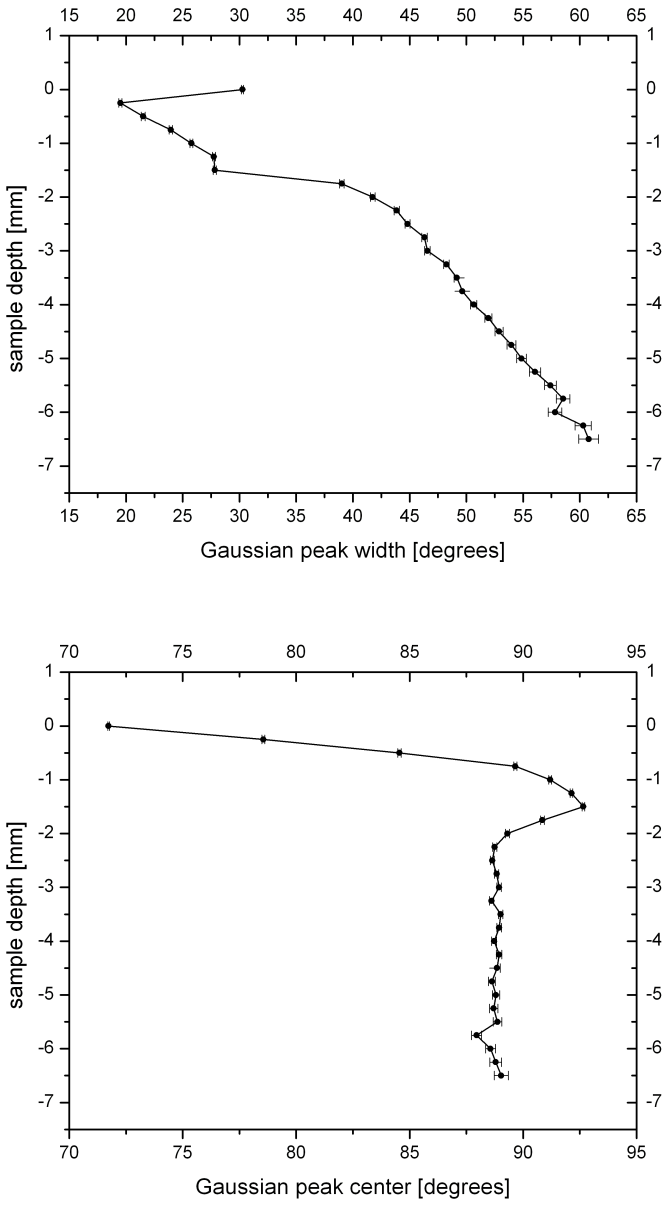

Figure 4.28: Plots of peak centra (top) and widths (bottom) found from Gaussian fits to the 2θ integrated diffractograms recorded from sample 4.13 at varying sample depths. The 2θ integration was limited to the 2wl (001) Bragg peak.

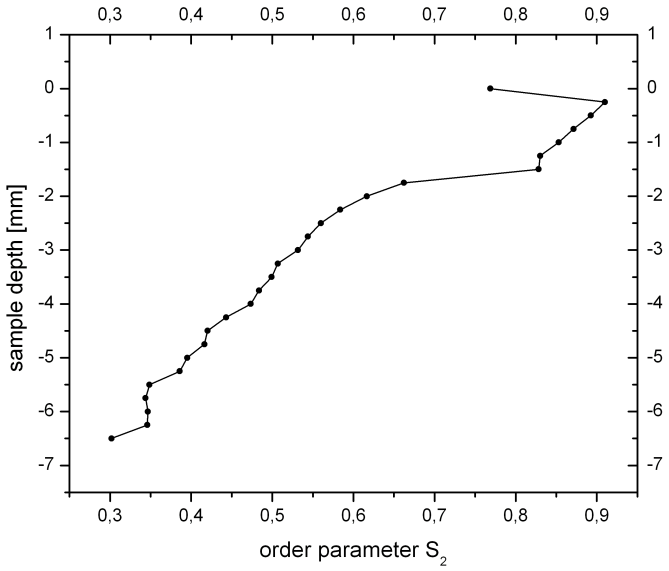

Figure 4.29: The uniaxial nematic order parameter S_2 plotted for the scattering data recorded from Mark tube sample 4.13 as a function of sample depth.

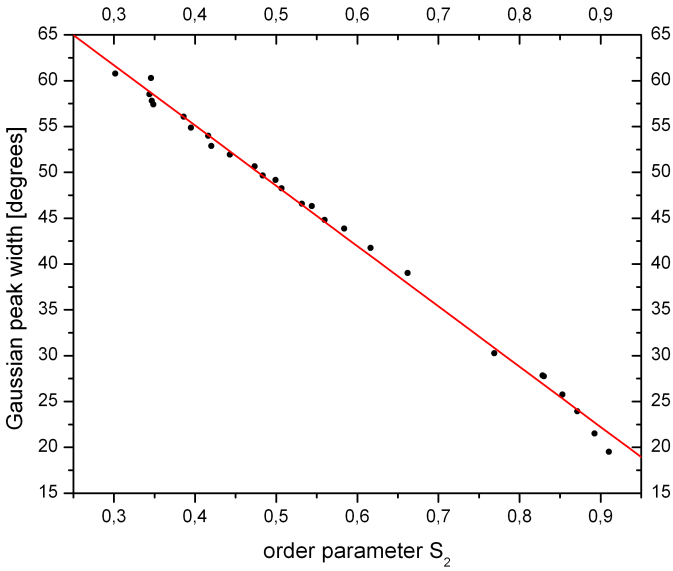

Figure 4.30: Plot of the Gaussian widths of Figure 4.28 versus the order parameter shown in Figure 4.29, for the scattering recorded from sample 4.13. The red line shows a linear fit to the data points.

Based on the discussion of section 2.4, one further point can be made from the scattering data recorded from sample 4.13, with regards to particle stacking polydispersities. It was explained in that section how the q-based peak width attributable to the sample could be approximated by the relation $\Omega_L \approx 2\pi/N_{av}d + \Delta dq/d$, yielding an estimate for the average number of stacks contributing to the 2wl Bragg scattering. Unfortunately, no good calibration samples were available at the PAL synchrotron and hence an estimate with regards to the instrumental width was not obtained. However, based on the scaled intensity plot of Figure 4.31 over the q-range of the 2wl Bragg ring, it seems that some changes in Bragg peak width may have occurred in response to the changing sample depth at which the profiles were obtained. Based on this preliminary observation, linear-background subtracted Bragg profiles were fitted with so-called Pseudo-Voigt functions[3] in order to more precisely evaluate the changes in the Bragg peak width. The fits obtained at depths of respectively -0.25 mm and -6.50 mm are shown in Figure 4.32. Neglecting both the contributions from the unknown instrumental width and from the strain $\Delta dq/d$, the obtained FWHM-values of these two fits correspond with particle thicknesses $N_{av}d$ of respectively 18.3 nm and 22.4 nm, and corresponding average stacking numbers of 12 and 15 unit layers. This is a small difference that only weakly supports the hypothesis that the higher sample regions contain fewer-stack particles. Because of the non-negligible uncertainties introduced by overlooking both the instrumental width and the strain, these results are at best qualitative and at worst invalid. It is therefore recommended that point-detector based studies especially designed for investigations into the possible stacking polydispersity in gravitationally settled and partially evaporated samples be undertaken. It is interesting to study the size selection of such fluorohectorite samples because it has already been shown that the order adopted in the topmost phase of gravitationally settled and partially evaporated samples is considerably higher than that usually observed in the standing nematic obtained by gravitational phase separation alone. When it is also recalled that the peaks observed in the small angle scattering from this highly orientationally ordered phase could correspond with inter-particle separations, this phase presents itself as a prime candidate for future studies aimed at observing phase transitions to smectite or columnar states in Na-fluorohectorite dispersions.
Figure 4.33 shows the integrated intensities profiles recorded from the partly

[3]Pseudo-Voigt functions are convolutions of Gaussian and Lorentzian distributions that are commonly used for evaluating peaks widths in scattering data; the Gaussian width of the convolved distributions then reflects the instrumental width whereas the Lorentz width corresponds with the inherent width of the Bragg peak [19]. Due to the unknown instrumental width, in the current discussion the Pseudo-Voigt function's characteristics are not further treated. An application of Pseudo-Voigt based peak analyses on fluorohectorite dispersions can be found in [9].

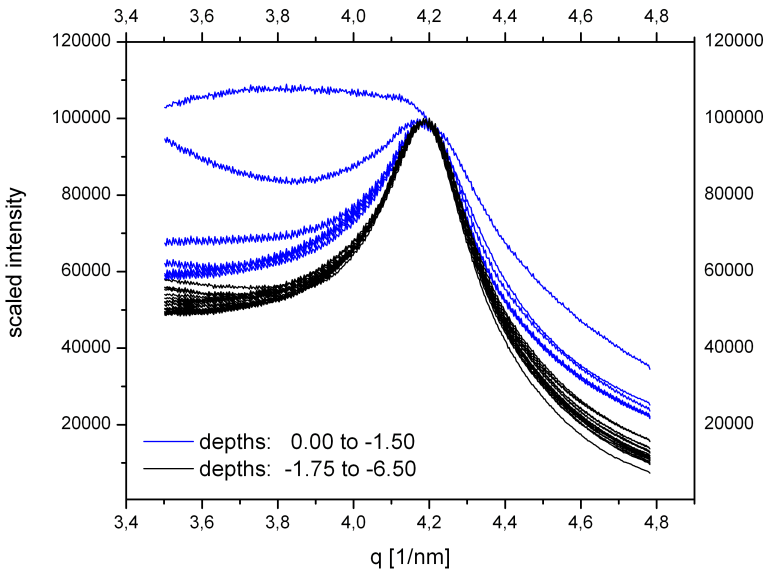

Figure 4.31: Plot of scaled intensities from sample 4.13 as functions of q; the scaling was accomplished by requiring that all Bragg peak maxima should occur at an intensity 100000.

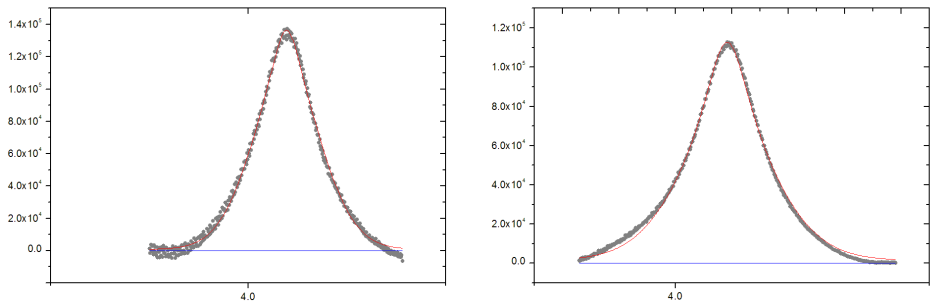

Figure 4.32: Pseudo-Voigt fits to the 2wl (001) Bragg peak in the intensity profiles recorded from sample 4.13 at depths of -0.25 mm (left) and -6.50 mm (right). The FWHM-values of the full peak profiles were found to be 0.344 nm^{-1} and 0.280 nm^{-1}, respectively.

evaporated sample 3.7 as functions of the scattering vector length q. Similar profiles are seen at depths between -1.00 mm and -4.00 mm, and between -6.00 mm and -19.0 mm. A sudden drop in intensity, similar to that observed in sample 4.13, is seen to occur between sample depths of -5.00 mm and -6.00 mm. Observed for both evaporated samples, it seems possible that this intensity drop reflects a transition between the nematic phase that grew from the dispersion-air interface downwards, as was illustrated in Figure 4.16, and the phase originally developed by sedimenting tactoids. That the depth of the transition is larger in the current sample relative to sample 4.13, can be explained in light of the more advanced evaporation seen in sample 4.13, causing all phases to appear compressed relative to those seen in sample 3.7. Furthermore, sample 4.13 was drawn from a 2w/w% dispersion whereas 3.7 originated from a 3w/w% dispersion, which might also contribute to the smaller phase volumes seen in the former. From Figure

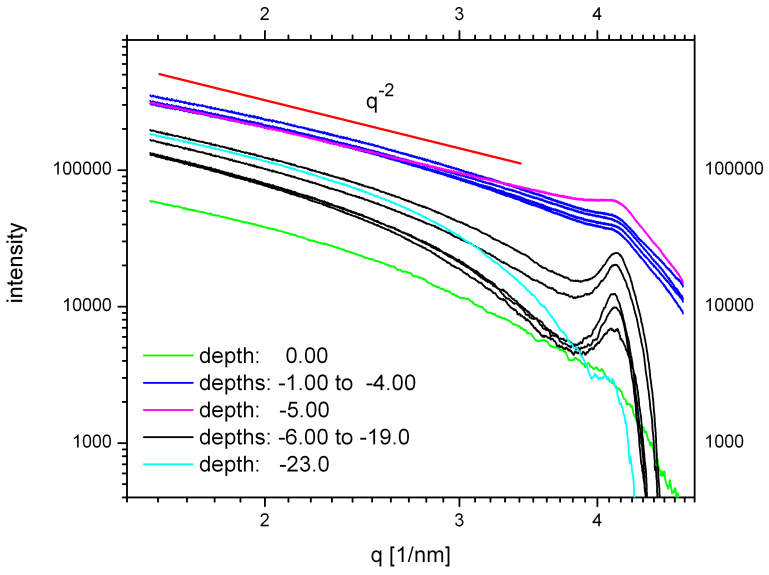

Figure 4.33: Intensity profiles recorded from sample 3.7 at the indicated depths. The profiles taken at depths of -5.00 mm and -23 mm deviate from the otherwise relatively smooth trends observed in the other profiles. In the range of profiles recorded between depths of -6.00 mm and -19.0 mm, the lowest intensity profiles correspond with the smallest depths - the opposite is true for the profiles recorded between -1.00 mm and -4.00 mm.

4.33 it is seen that the -5.00 mm profile shows an increased Bragg scattering relative to data recorded closer to the dispersion-air interface. The

2wl (001) Bragg scattering peak remains notable down to a sample depth of at least -19.0 mm, with the exception of the 0.00 mm position, where no Bragg ring is observed. It is seen that the intensity profile obtained at -23.0 mm has a significantly reduced (001) Bragg intensity relative to the profiles recorded above it. Unfortunately, it was found that trying to calculate the order parameter of the scattering data from sample 3.7 likely would introduce artificial features, due to a marked ϕ intensity modulation in the 2wl Bragg ring not compatible with Maier-Saupe fitting – showing for instance more than two peaks in the azimuthal profiles. Often, it appeared that shadowing effects from the 2 mm capillary featured in and reduced the observed intensity in the vertical direction.

Figures 4.34 and 4.35 shows raw data obtained from vertical scans mapping the scattering from sample 4.13, so that the scan effectively shows the orientational distribution of Na-fluorohectorite particles across the short capillary axis. Previous studies have reported considerable homeotropic wall anchoring of Na-fluorohectorite particles to polar glass walls [10]. In the scans across sample 4.13's short capillary axis however (wall to wall), no changes in particle orientations are seen to occur at the -2.00 mm depth, whereas in contrast, remarkable changes are seen in the data recorded close to the dispersion-air interface, where the scattering goes from a completely horizontal to an almost completely vertical azimuthal orientation, and back again. This seems to indicate that the notable changes in the scattering profiles close to the dispersion-air interface, are attributable to the dispersion meniscus and not to wall anchoring. If it were attributable to wall anchoring effects, the changes observed close to the interface should have been seen also at the -2.00 mm depth. The apparent lack of wall anchoring can be explained if the anchored regions extended to distances much smaller than the scan's resolution. However, in these scans the beam defining slit was only 30×50 μm. Another explanation might simply be that the particles in the colored phase have for some reason not adopted a homeotropic configuration near the capillary walls. If the first explanation is assumed correct, the presence of only a very narrow homeotropic layer might be explained in light of the results presented in the previous sections, which were found to indicate that the phase which the present scan was taken from could contain on average smaller particle stacks than lower sample regions. The distributing effects of wall alignment in a phase containing relatively smaller particles might be thought weaker, so that the region over which distorted particle orientations are correlated becomes smaller. However, the high order parameters observed close to the dispersion-air interface argues against this explanation, since the higher the order parameter is, the stronger the force required to distort the phase. It could be possible that the orienting effects of the dispersion-air interface are so strong relative to the wall anchoring, that the effects of the former, from a free energy minimization point of view, overrides wall anchoring. However, this possible explanation

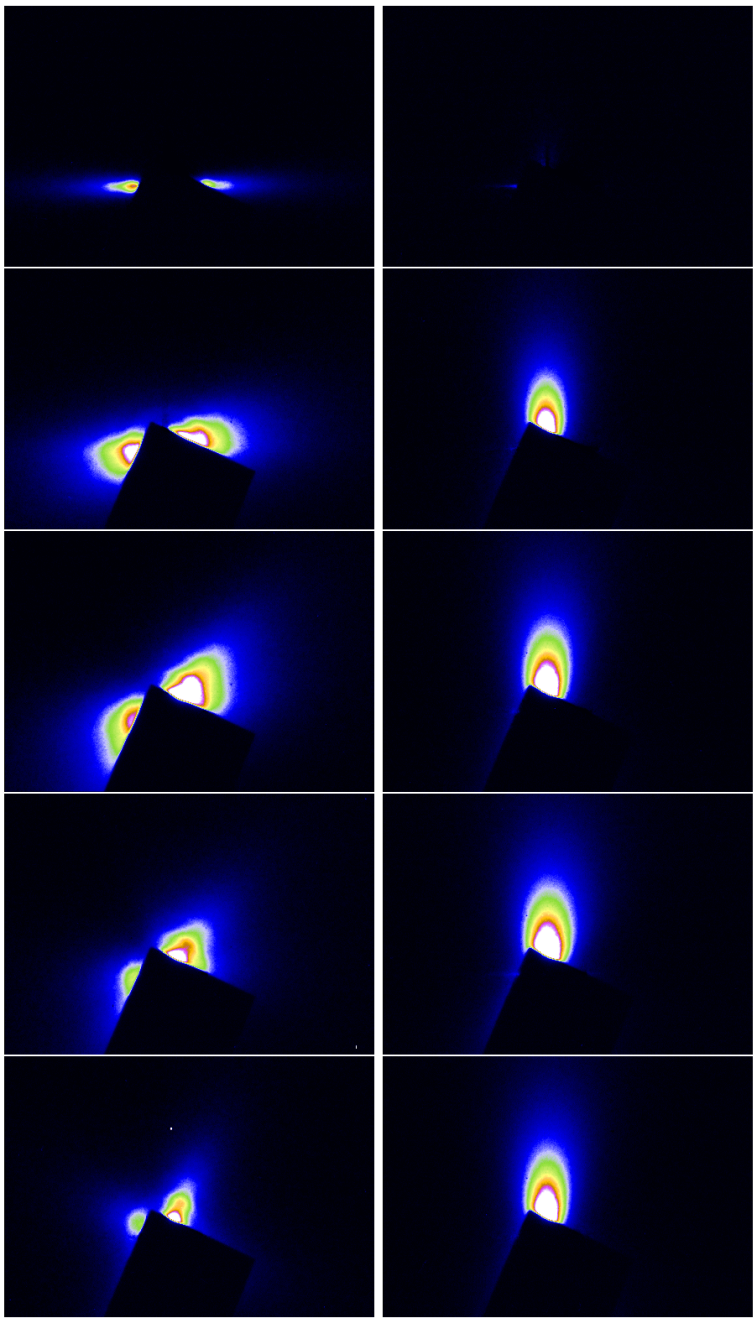

Figure 4.34: Raw scattering images recorded from a horizontal scan across sample 4.13 at step intervals of 0.10 mm. The left column shows images recorded close to the dispersion-air interface at a depth of 0.00 mm. The right column shows images recorded at a depth of −2.00 mm, whose horizontal locations in the capillary correspond with those in the left column.

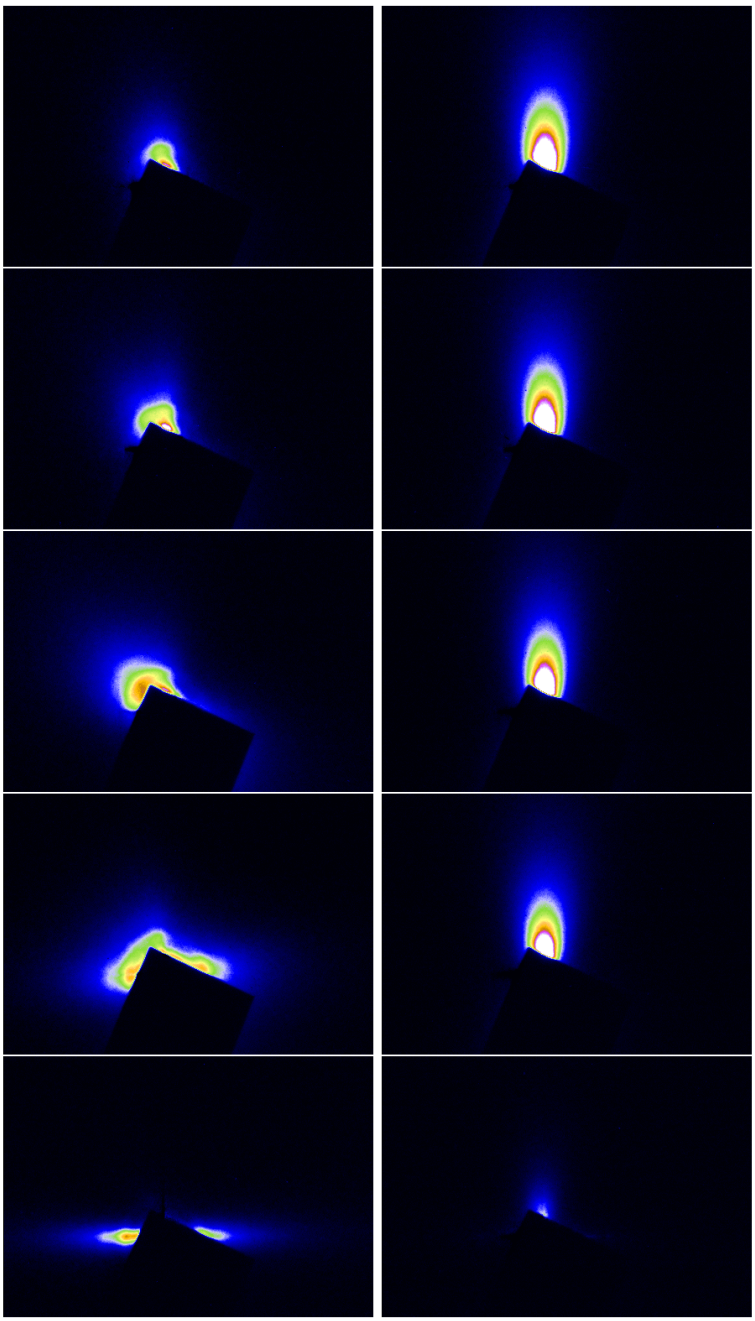

Figure 4.35: Raw scattering images recorded from a horizontal scan across sample 4.13 at step intervals of 0.10 mm. The left column shows images recorded close to the dispersion-air interface at a depth of 0.00 mm. The right column shows images recorded at a depth of −2.00 mm, whose horizontal locations in the capillary correspond with those in the left column.

for the lack of wall anchoring seen at the -2.00 mm depth is countered by the apparent curvature of the phase at the interface – this curvature apparently does not distribute down to -2.00 mm. It is therefore not understood why the there are such marked changes between the horizontally recorded scattering profiles at the two different depths.

4.4 The Fréedericksz transition for Na-fluorohectorite

The current section will address the effect of magnetic fields on Na-fluorohectorite dispersions. Figure 4.36 shows optical images of sample m.1 taken between 90° crossed polarizers after the sample had been turned 90° around it's long capillary axis in a magnetic field of 0.97 T. Prior to turning, the sample had been standing in this field for several days. Because of the general tendency for the sample to darken with time, it is likely that the dark stripes, especially visible in the first images, represent the stable configuration for fluorohectorite particles in the field. From section 2.3.2 it is known that this configuration is achieved when the nematic director $\vec{n}$ is perpendicular to the field, so that the clay platelets are either lying face down or standing with their faces oriented parallel with the field (they can also be tilted over – this configuration is however incompatible with the observed birefringence extinction). As seen from the discussion of section 2.3.3, these configurations correspond with the requirement for the propagating light to either experience only the extraordinary or the ordinary index of refraction of the medium, so that no birefringence is observed. It should be noted that from the optical images of Figure 4.36 alone, it is not possible to determine whether the black stripes all originate from face down particles, from standing particles, or from a mixture of both, either within a single stripe or between different stripes. There seems to be a tendency for less defined black regions to grow from within the middle of the larger stripes, that appear orange in the first images of Figure 4.36. It could be that these black regions, which develop much more slowly than the defined stripes, represent one stable configuration while the defined stripes represent the other.

Figure 4.37 shows two images of Fréedericksz transition stripes in sample m.1. The experiment was as much as possible identical to the one whose results are depicted in Figure 4.36, but was conducted at a later time. The leftmost image of Figure 4.37 shows a pattern that is relatively similar to those shown in Figure 4.36, particularly with respects to the colors of the transmitted light, which is prominently orange and turquoise. In the rightmost image of Figure 4.37 the sample was turned approximately 45° around it's long capillary axis before re-photographed. It is seen that the horizontal black stripes are still present. This indicates that the particles comprising the striped regions likely are lying face down, since a 45° rotation of a uniform standing nematic would turn it off the extinction position.

Figure 4.36: Optical microscopy images between 90° crossed polarizers of a periodic pattern that has appeared in the 1 mm Mark tube sample m.1 after it was turned 90° around it's long capillary axis in a magnetic field of 0.97 T. The field lies in the image plane. Prior to turning, the sample had been standing in a field perpendicular to the image plane for several days. The field was present also while the images were recorded. All images were recorded with the same exposure time.

Figure 4.37: Microscope images of magnetically induced Fréedericksz transition stripes in sample m.1. The experimental setup was as much as possible identical to that described in Figure 4.36. In the rightmost image, the sample has been turned 45° around it's long capillary axis.

Figure 4.38 shows a set of intensity profiles obtained by integrating the scattering data from sample m.1 shown in figures 4.39, 4.40 and 4.41 over the azimuthal angle ϕ. The data was obtained at the PAL synchrotron. The reference depth of 0.00 mm is also in this series taken as the position of the first scan recorded – however, for the non-evaporated m.1 sample this reference depth does not correspond with the dispersion-air interface. The intensity profiles plotted in Figure 4.38, corresponding with the raw scattering data of figures 4.39, 4.40 and 4.41, are all taken from the second standing nematic phase of sample m.1. The sample had been standing in a magnetic field of approximately 1 T for a few days before the scans were recorded. In the hour and a half before the first scattering image was taken, the sample was turned 90° around it's long capillary axis while still in the field. When striped patterns were visible in the second standing nematic when viewed between crossed polarizers (naked eye observations), the sample was removed from the magnetic field and the scan series started immediately. The incident direction of the x-ray beam with respects to the sample was parallel to the original direction of the magnetic field prior to turning. It is important to note that, because each scan at a given sample depth is composed of 55 scattering images and 5 darks recorded over a timespan of about 23 min, it is possible that time dynamics play a role in this data series, both between images taken at different depths, as well as within a single image. This is due to the increased dynamics initially induced by the magnetic field.

From Figure 4.38 it is seen that, like the previously discussed samples, also m.1 shows small-angle intensity profiles which approximately scale with q^{-2} – however, the power law for a linear fit to the intensities is slightly below this value (it was found to be close to 1.7). A very notable feature of these scattering profiles, is the complete absence of the expected 2wl (001) Bragg ring. No Bragg ring was observed in any of the scans taken from the second nematic phase of sample m.1. It is possible that this feature could be an effect of the magnetic field, which might be thought to have aligned the particles in a fashion not compatible with the requirements for observations of Bragg interlayer scattering at the detector plane. The shape of the small-angle scattering from sample m.1 however, does not present any evidence that supports this hypothesis. In fact, the q^{-2}-shaped small-angle scattering along with it's marked azimuthal anisotropy, rather indicates that a significant amount of the dispersed platelets are oriented with their directors parallel with the scattering vector $\vec{q}$, in a configuration that is compatible with the requirement for observing interlayer Bragg scattering at the detector. It could be thought that a low particle density in the second nematic phase explains the lack of observable 2wl (001) scattering. That the small-angle profiles have intensities and azimuthal distributions comparable to those observed in the profiles recorded from sample 4.13 and 3.7, where interlayer Bragg scattering was visible above the small-angle background,

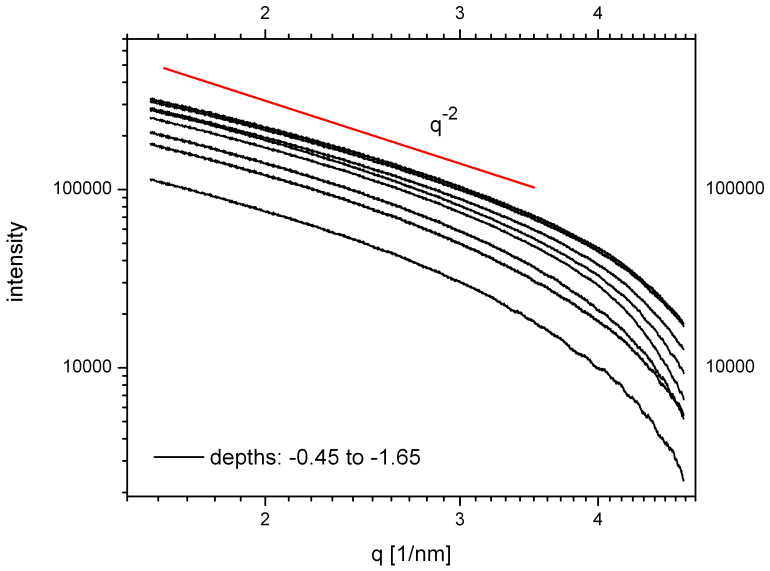

Figure 4.38: Scattered intensity profiles recorded from sample m.1.

argues against this explanation. However, as already discussed in earlier sections, another explanation for the lack of 2wl (001) Bragg scattering, might be that the particles in the investigated phase were not present as significantly stacked lamellar structures. It is in this context interesting to note that sample m.1, prepared by Ringdal for his master thesis [59], was at the time these scans were recorded more than one year old. On such time-scales, even relatively small particles present in the initial fluorohectorite dispersion likely would have had time to settle. It is also worth to point out that sample m.1 proved much more responsive to magnetic fields than other investigated samples, which is why it features so prominently in the current section. Attempts at observing the Fréedericksz transition in the second standing nematic phase of newer samples were unfruitful. The fact that previous attempts at aligning the first standing nematic in magnetic fields also have failed [59], might indicate that particle size is an important parameter in this context. However, it is also known that the first standing nematic has a higher viscosity (is less fluid-like [59]) than the second nematic, which would explain why it is harder to align the former by application of external fields.

It is now time to pick up the thread which was left off at the end of section 2.3.2, discussing the possible morphologies of Na-fluorohectorite platelets in the Fréedericksz transition process, described both in that section and in the

current discussion. The raw scattering images of Figure 4.40 shows that, at a relatively large range of depths, the small angle scattering is peaked at azimuthal angles between 40° and 50°, corresponding with platelets tilted at angles of 50° and 40° with respects to the long capillary axis – a configuration that does not correspond with the stable alignment relative to the reorienting field. This platelet orientation does however corresponds with the intermediate state between the standing configuration, stable and probable in the initial field, and the face down configuration, that would be stable in the reorienting field (and in the initial field as well). It is possible that the scattering images shown in Figure 4.40 correspond with a frozen-in snapshot of a certain platelet configuration adopted in the reconfiguration process – that this configuration is relatively time-stable could be explained due to the important fact that the reorienting field was removed before the sample was exposed to the x-ray beam and the scattering data recorded. Once the field is removed, this tilted over orientation is of course no longer inherently unstable, unless it is disfavored by either the capillary walls or the surrounding director field. If the latter forces do not work to alter the tilted configuration as it was at the time the reorienting field was removed, or if these forces are relatively weak, then it is very possible that the scattering images of Figure 4.40 do indeed show a frozen-in structure obtained midways in the reorienting process. It is worth noting that, to an observer regarding m.1 in a crossed-polarizer setup with the light path oriented parallel with the x-ray beam, the proposed tilted-over orientation of the Na-fluorohectorite platelets would present a birefringent and non-extinct sample region. The scattering images of Figure 4.40 do therefore not present any evidence with regards to particle orientations in the dark Fréedericksz transition regions observed optically.

The scattering images shown in figures 4.39 and 4.41, at depths respectively above or below the previous discussed data, are somewhat harder to interpret, as several particle orientations seem to contribute to a single scattering image. Because of the two-dimensional character of the scattering data, it is not possible to determine whether these many-featured scattering profiles result from sample regions that adopt multiple orientations in the horizontal plane or in the vertical plane, or in both directions simultaneously. In the last images of Figure 4.41, it is seen that again one direction prevails; the scattering here peaks at an azimuthal angle of between 110° and 120°, and can be explained by the same frozen-in reorientation between standing and face down configurations that was used to illustrate the possible physical origin of the scattering data shown in Figure 4.40. In the theoretical discussion of the Fréedericksz transition of section 2.3.2, it was found that a reorientation from standing to face down platelet orientations would be preferable over the reorientation pathway involving platelet rotations around the direction of the long capillary axis. This hypothesis is supported by the scattering data shown in Figures 4.40 and 4.41.

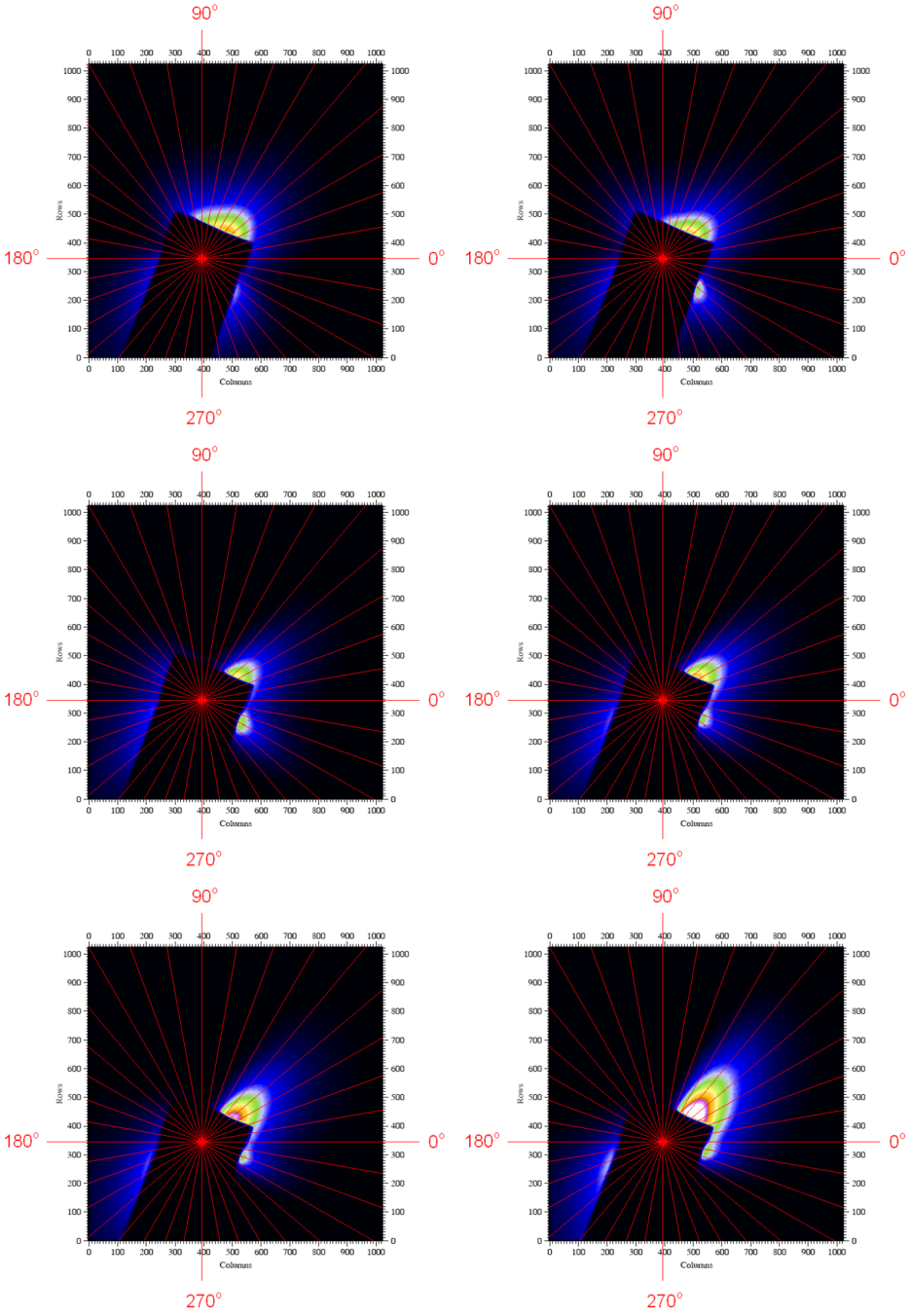

Figure 4.39: Raw scattering images recorded from sample m.1. The scans were taken at depths between 0.00 mm (upper left image) and −0.75 mm (lower right image). Each displayed image was compiled from 55 individual frames and 5 darks, taken over a timespan of approximately 23 min.

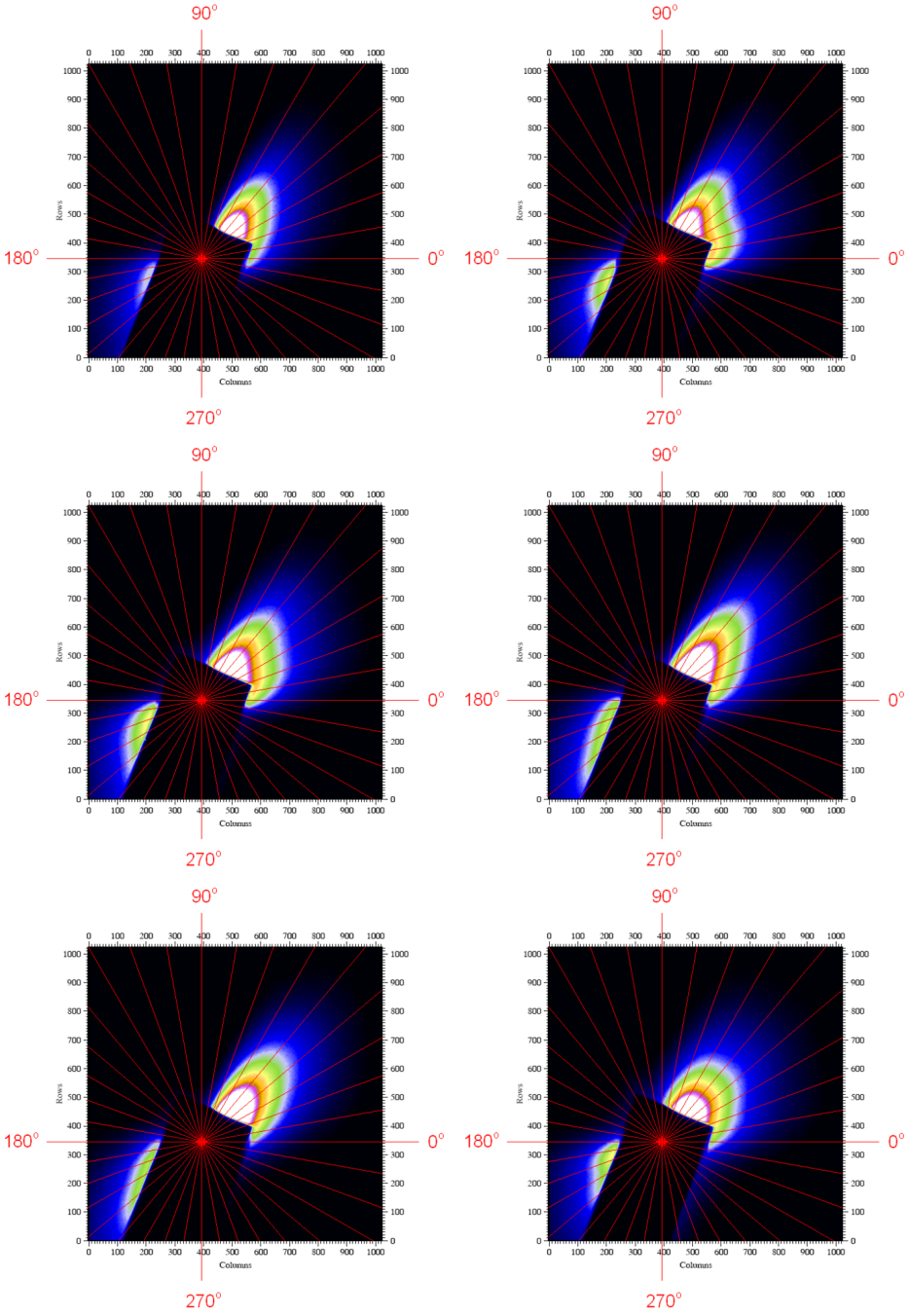

Figure 4.40: Raw scattering images recorded from sample m.1. The scans were taken at depths between −0.90 mm (upper left image) and −1.65 mm (lower right image). Each displayed image was compiled from 55 individual frames and 5 darks, taken over a timespan of approximately 23 min.

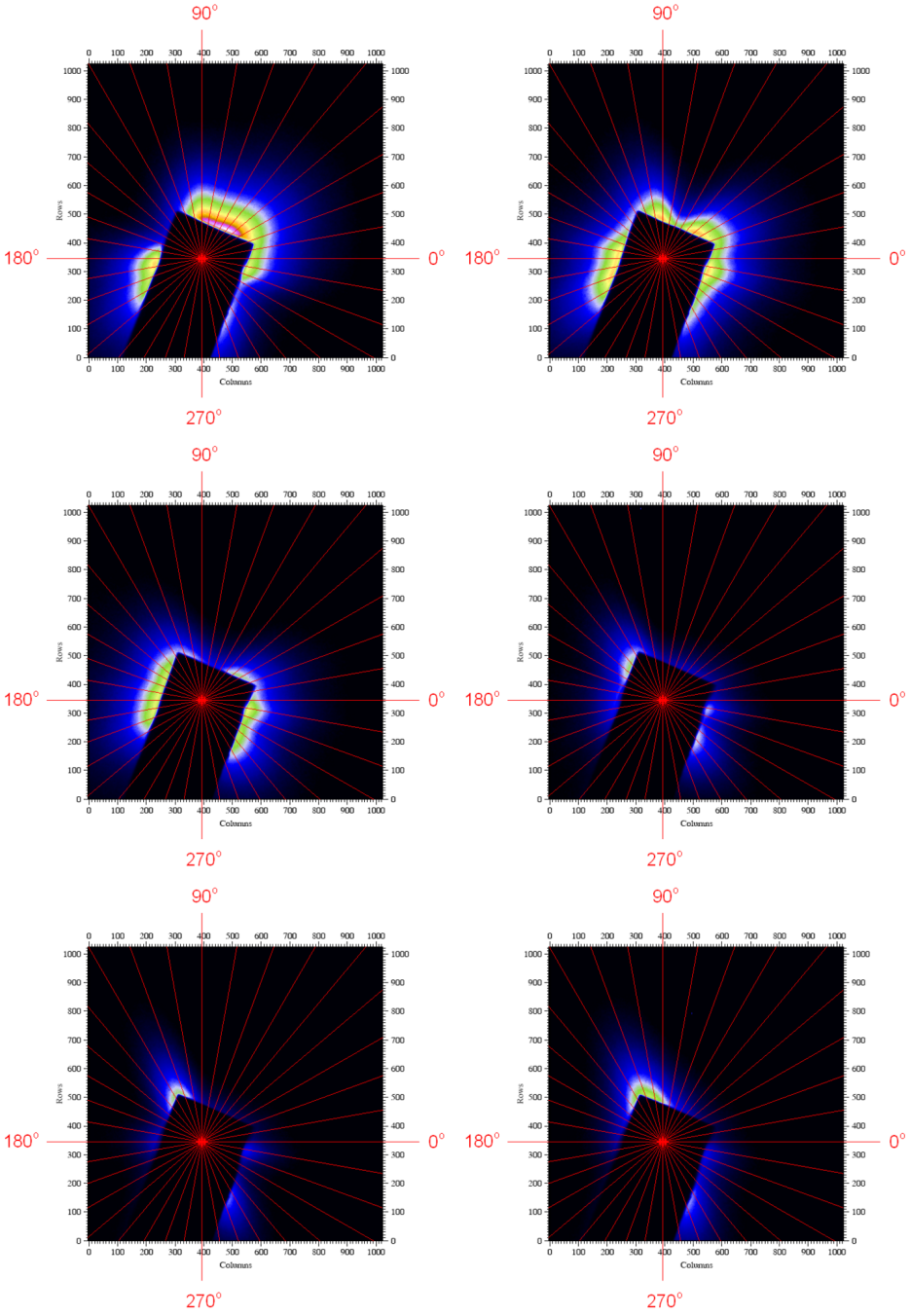

Figure 4.41: Raw scattering images recorded from sample m.1. The scans were taken at depths between −1.80 mm (upper left image) and −2.55 mm (lower right image). Each displayed image was compiled from 55 individual frames and 5 darks, taken over a timespan of approximately 23 min.

Chapter 5

Conclusions and suggestions for future studies

The current chapter will attempt to sum up the results and discussions of the previous chapter, and offer some hints with regards to topics where further investigations likely could shed more light on the features observed in the fluorohectorite dispersions investigated. In the previous chapter, several, but never conclusive, results were found to indicate that there is a possibility of gravity and Brownian motion sorting particles into different sample strata that are characterized not only by distributions in particle diameters but also in the number of unit layers contained in each lamellar platelet. The fact that the sedimentational velocities of colloidal platelets were already in the theory chapter determined as being proportional to the radius and diameter factor Rd [81, 53], provides a theoretical background for why it is expected that platelets polydisperse in both their radii and diameters should be sorted by gravity into vertical strata, where the larger Rd particles form the bottom parts of the dispersions. The lack of Bragg scattering observed in the intensity profiles recorded in the second standing nematic phase of the Fréedericksz transition sample m.1, as well as the observed peaks in the small-angle scattering from evaporated samples, points to the possibility of the existence of larger polydispersities in the number of stacked unit layers for Na-fluorohectorite then what has been reported previously. It is also worth pointing out that, in relation to the discussed attempts at phase stabilization of capillary samples drawn from an already partially settled Na-fluorohectorite dispersion, it was found that both birefringence colors, corresponding values of Δn, and observed textures all indicate that particle sizes are determining for the type of phases observed. This is also noted in usual gravitationally settled capillary samples, where consistently two birefringent phases that are visually different are seen to develop atop each other. The first phase, referred to as the normal or first standing nematic, grows by sedimenting tactoids; the second precipitates out of solution later

on. It is with respects to the discussions presented with regards to the terminal velocities of colloidal particles in the gravitational field, likely that size parameters determine which particles form sedimenting tactoids and which form the second nematic phase. In the theory chapter discussions on the DLVO-potential, it was found that smaller-stacked particles are more overall repulsive than larger stacked structures, at a given electrolyte concentration. Larger-stack particles might thus undergo tactoid-forming nucleation-and-growth processes at a given salt concentration, whereas a portion of the potentially smaller-stacked particles initially would remain dispersed due to the effects of Brownian motion and slow sedimentational velocities, and later on, would be mutually repulsive. Marked discrepancies are however found between the inter-platelet separations observed from the small-angle peaks in the scattering profiles of the evaporated samples, and the DLVO-based arguments. The derived DLVO-potentials are however very uncertain with regards to their validity, both because of the estimates made to unknown parameters such as the Hamaker constant for fluorohectorite platelets, and due to the discussed possibility that the DLVO-interactions only are truly valid for dilute systems. Scattering studies aimed at determining the stacking polydispersity of Na-fluorohectorite dispersions over a large range of depths could be undertaken with the intention of shedding some light on the validity of the hypothesis that the featuring platelets are polydisperse not only in the particle diameter but also in the number of stacked unit layers, and that they are sorted by gravity accordingly. Another investigation method can be envisioned based on a combination of optical and x-ray based studies. As discussed, the birefringence $\Delta n \propto \Delta\epsilon$ as well as the total diamagnetic susceptibility anisotropy $\Delta\chi_{tot}$ of fluorohectorite dispersions are proportional to S_2 under the assumption that the extent of the nematic regions probed contain a spatially invariant distribution in particle anisotropies. A plot of the calculated optical birefringence Δn versus values of the order parameter S_2 obtained for the same sample over a range of corresponding depths at a given time, should then present a linear relationship if the distribution in particle anisotropies is indeed the same for all the sample regions probed. If the relationship on the other hand, is found not to be linear, then this indicates that there is a spatial dependence to the distribution of the platelets' anisotropies. This technique would probe the combined effects of both the radial and stacking size parameters. From a both theoretical and experimental perspective, it would also be interesting to try glean some insight into the physical reason for why there is a polydispersity in particle stack size in the first place; that there is, has already been determined [12].

The magnetic investigations conducted on sample m.1 presented some interesting scattering profiles. Attempts were made at explaining the more uniformly tilted azimuthal profiles as being frozen-in snapshots of a certain point along the reorientation pathway from an initially stable standing configuration to a face down configuration, that would be stable in the reorient-

ing field. In the theory chapter, it was determined that such a platelet rotation would correspond to a splay-and-bend distortion of the nematic director, favorable relative to the pathway featuring splay-and-twist distortions due to platelet rotations around the long capillary axis, under the assumption that the general relation $K_{22} \geq K_{11} > K_{33}$ [80, 67] for the Frank elastic constants of disc-like nematogens holds true also for fluorohectorite dispersions. Any definite connections between the optical birefringence photographs of the Fréedericksz transition and the presented scattering data were not identified. In future studies, it would be favorable to have an optical birefringence setup available for sample photography immediately before the scattering data are recorded. X-ray scattering studies on the Fréedericksz transition in Na-fluorohectorite dispersions should also preferably be conducted at a synchrotron beamline delivering intensities high enough to allow for the entire second nematic phase to be investigated within a time frame of no more than two hours.

In addition to Na-fluorohectorite, aqueous dispersion of Li-, Fe- and Ni-fluorohectorite were investigated qualitatively in the current project; the differing behaviors observed with respects to everything from sedimentational features, gelling, volume swelling and phase separation demonstrate the complexity of these systems and the likely determining effect the type of intercalated cation has on the overall dispersion behavior. In order to confirm or disprove the striking dissimilarities observed between respectively the monovalently and di- and trivalently intercalated fluorohectorites investigated, studies should be conducted on at least two different clay powder batches for each given clay. It has previously been demonstrated how features such as different methods for powder crushing can markedly change the sedimentational behavior of aqueous Na-fluorohectorite dispersions [59]; it is therefore possible and likely that specific powder preparation procedures might have contributed to the observed features of all the investigated dispersions of the current project.

As a final conclusion, there are two main themes of the current project that really merit further investigations. The first one is the observed Fréedericksz transition, that now has been determined to likely consist of a splay-and-bend distortion. Further investigations with more suitable sample holders might ultimately yield quantitative data with regards to wall anchoring strengths and the Frank moduli. The second main theme is the presence of true uniaxial nematic order obtained by slowly evaporating samples simultaneously setteling by the force of gravity. The high values of the order parameter as well as the presence of peaks in the small-angle profiles from these samples, marks them as prime candidates for further investigations on the liquid crystalline behaviour of Na-fluorohectorite dispersions, perhaps also beyond the nematic.

Appendix A

Basic principles of electromagnetism

The current appendix deals with the basics of electromagnetism from a classical, Maxwellian viewpoint with the purpose of providing a common background for the various parts of the current text which deal with electromagnetic phenomena. Most notably, these parts include sections 2.3.2, 2.3.3 and 2.4. Section 2.3.2 introduced electromagnetic phenomena through the aligning effects which electric or magnetic fields have on particles with anisotropic electromagnetic properties. Furthermore, in section 2.3.3, the effect of such anisotropies on light propagation were investigated. Section 2.4 on the other hand, introduced the concepts of x-ray scattering from the point of view of quantum mechanics. A rudimentary background for the quantum mechanical treatment of that section can be found in Appendix B. Presently, the starting point of the current appendix will be Maxwell's equations, written on differential form as follows [26]:

$$\nabla \times \vec{E} = \frac{-\delta \vec{B}}{\delta t} \tag{A.1}$$

$$\nabla \cdot \vec{E} = \frac{\rho}{\bar{\epsilon}} \tag{A.2}$$

$$\nabla \times \vec{B} = \bar{\mu}\vec{J} + \bar{\mu}\bar{\epsilon}\frac{\delta \vec{E}}{\delta t} \tag{A.3}$$

$$\nabla \cdot \vec{B} = 0 \tag{A.4}$$

These four equations form the basis of classical electromagnetism. The involved parameters are defined along with their units in Table A.1. Some disagreement evidently still exist in the scientific community with regards to which parameter should be used to define the magnetic field. In the present discussion, the following general relations will define the roles of the electric

field $\vec{E}$, the magnetic field $\vec{B}$, and the auxiliary fields $\vec{D}$ and $\vec{H}$:

$$\vec{D} = \epsilon_0 \vec{E} + \vec{P} \tag{A.5}$$

$$\vec{H} = \frac{1}{\mu_0}\vec{B} - \vec{M} \tag{A.6}$$

For linear media the polarization $\vec{P} = \epsilon_0 \chi_e \vec{E}$ and the magnetization $M = \chi_m \vec{H}$, so that these equations can be written [26]:

$$\vec{D} = \bar{\epsilon}\vec{E} \tag{A.7}$$

$$\vec{H} = \frac{1}{\bar{\mu}}\vec{B} \tag{A.8}$$

In general, the electrical permittivity $\bar{\epsilon} = \epsilon_0 \left(1 + \bar{\chi}_{\vec{E}}\right)$ as well as the magnetic permeability $\bar{\mu} = \mu_0 \left(1 + \bar{\chi}_{\vec{B}}\right)$ are not constants, but tensor functions of the space coordinates and possibly also of time and of the frequency of the fields. In vacuum or in isotropic, non-dispersive media however, the permittivity and permeability are indeed constants so that in these special cases $\vec{D} \parallel \vec{E}$ and a $\vec{H} \parallel \vec{B}$. For linear dielectric and diamagnetic materials the permittivity and permeability tensors can be written as follows, where a coordinate system is chosen so that the director $\vec{n}$ points along the cartesian z [36]:

$$\bar{\epsilon} = \begin{pmatrix} \epsilon_\perp & 0 & 0 \\ 0 & \epsilon_\perp & 0 \\ 0 & 0 & \epsilon_\parallel \end{pmatrix} \tag{A.9}$$

$$\bar{\mu} = \begin{pmatrix} \mu_\perp & 0 & 0 \\ 0 & \mu_\perp & 0 \\ 0 & 0 & \mu_\parallel \end{pmatrix} \tag{A.10}$$

Commonly, the anisotropies in the permittivity and permeability are expressed through $\Delta\epsilon = \epsilon_\parallel - \epsilon_\perp$ and $\Delta\mu = \mu_\parallel - \mu_\perp$.

A.1 Electromagnetic waves

The existence of electromagnetic waves can be deduced directly from Maxwell's relations by decoupling these first-order, partial differential equations. In vacuum this will yield the following two second-order equations for the electric and magnetic fields, respectively [26]:

$$\nabla^2 \vec{E} = \mu_0 \epsilon_0 \frac{\partial^2 \vec{E}}{\partial t^2} \tag{A.11}$$

$$\nabla^2 \vec{B} = \mu_0 \epsilon_0 \frac{\partial^2 \vec{B}}{\partial t^2} \tag{A.12}$$

Table A.1: Overview of the central parameters of electromagnetism and their SI or SI derived units [52].

parameter	symbol	units
electric charge	e	C= sA
electric current	J	A
electric field	$\vec{E}$	V/m= mkg/s^{3}A
electric displacement	$\vec{D}$	C/m^2= sA/m^2
capacitance	-	F= C/V= s^{4}A^2/m^{2}kg
permittivity	ϵ	F/m= s^{4}A^2/mkg
magnetic flux	-	Wb= sV= m^{2}kg/s^{2}A
magnetic field	$\vec{B}$	T= Wb/m^2= kg/s^{2}A
auxiliary field	$\vec{H}$	A/m
inductance	-	H= Wb/A= m^{2}kg/s^{2}A^2
permeability	μ	H/m= mkg/s^{2}A^2

Their form are identical to the three-dimensional wave equation, and supports for instance the propagation of plane waves characterized by the following expressions [26]:

$$\vec{E}\left(\vec{r},t\right) = E_0 \exp\left[i\vec{k}\cdot\vec{r} - i\omega t\right]\vec{o} \tag{A.13}$$

$$\begin{aligned}\vec{B}\left(\vec{r},t\right) &= B_0 \exp\left[i\vec{k}\cdot\vec{r} - i\omega t\right]\vec{k}\times\vec{o} \\ &= \frac{1}{c}\vec{k}\times\vec{E}\end{aligned} \tag{A.14}$$

Here $c = 1/\sqrt{\mu_0\epsilon_0}$ is the speed of light and $\vec{o}$ the direction of polarization of the electric field. The transition to the last line is based on the fact that the amplitude $B_0 = E_0/c$ [26]. These relations are valid for propagation in vacuum. When electromagnetic waves travel through matter, the presence of electric charges and currents affect the propagating fields. In the familiar case of linear, isotropic media of spatially constant ϵ and μ, the only modification to the previous appears as a change in the phase velocity υ of the waves, now equal not to $\sqrt{\mu_0\epsilon_0}$ but to $\sqrt{\mu\epsilon}$, so that the quantity known as the index of refraction of the material is defined as $n = \sqrt{\mu\epsilon/\mu_0\epsilon_0} = c/\upsilon$. The case of anisotropic media was discussed in section 2.3.3.

Appendix B

Quantum mechanical x-ray interactions

The current section will address the interaction of x-rays with matter from a quantum mechanical perspective. It is in this context convenient to express the electromagnetic radiation field through the vector potential $\vec{A}$, which is quantized, and a scalar potential ϕ. The conventional electric and magnetic fields and the vector and scalar potentials are related via the following:

$$\vec{E} = -\nabla\phi - \frac{\partial\vec{A}}{\partial t} \tag{B.1}$$

$$\vec{B} = \nabla \times \vec{A} \tag{B.2}$$

Within the Coulomb gauge for a pure radiation field, the scalar potential $\phi = 0$. The quantized vector potential is then expressed as a function of the creation and annihilation operators $a^\dagger$ and a:

$$\vec{A}(\vec{r},t) = \sum_{\vec{k},o} \vec{o}_{\vec{k},o} \sqrt{\frac{\hbar}{2\epsilon_0 V \omega_{\vec{k}}}} \left(a_{\vec{k},o} \exp\left[i\vec{k}\cdot\vec{r}\right] + a^\dagger_{\vec{k},o} \exp\left[-i\vec{k}\cdot\vec{r}\right] \right) \tag{B.3}$$

The radiation field is represented as a vector $\left| n_{\vec{k}_1,o_1}, n_{\vec{k}_2,o_2}, ... \right\rangle$ where $n_{\vec{k},o}$ denotes the number of photons in a mode of wavevector $\vec{k}$ and polarization o. The creation and annihilation operators serve to change the occupancy of a mode by one photon:

$$a^\dagger \left| n_{\vec{k},o} \right\rangle = \sqrt{n_{\vec{k},o}+1} \exp\left[i\omega_{\vec{k}}t\right] \left| n_{\vec{k},o}+1 \right\rangle \tag{B.4}$$

$$a \left| n_{\vec{k},o} \right\rangle = \sqrt{n_{\vec{k},o}} \exp\left[-i\omega_{\vec{k}}t\right] \left| n_{\vec{k},o}-1 \right\rangle \tag{B.5}$$

In analogy to the classical picture, photons interact with charged bodies. The Hamiltonian for a non-relativistic, free particle of mass m and charge q

is:

$$\widehat{H}_0 = \frac{\widehat{\vec{p}}^2}{2m} \tag{B.6}$$

In the presence of a radiation field, represented through the vector potential $\vec{A}$, the free particle Hamiltonian will be modified to account for the coupling between the field and particle:

$$\widehat{H} = \frac{\left(\widehat{\vec{p}} - q\vec{A}\left(\vec{r},t\right)\right)^2}{2m} \tag{B.7}$$

The contribution from the field can be isolated by subtracting the free particle Hamiltonian $\widehat{H}_0$ from $\widehat{H}$:

$$\begin{aligned}
\widehat{H}' &= \widehat{H} - \widehat{H}_0 \\
&= \frac{\left(\widehat{\vec{p}} - q\vec{A}\left(\vec{r},t\right)\right)^2}{2m} - \frac{\widehat{\vec{p}}^2}{2m} \\
&= -\frac{q\widehat{\vec{p}}\cdot\vec{A}}{2m} - \frac{q\vec{A}\cdot\widehat{\vec{p}}}{2m} + \frac{\widehat{\vec{p}}^2}{2m} + \frac{q^2\vec{A}^2}{2m} - \frac{\widehat{\vec{p}}^2}{2m} \\
&= -\frac{q\vec{A}\cdot\widehat{\vec{p}}}{m} + \frac{q^2\vec{A}^2}{2m} \\
&= \widehat{H}'_1 + \widehat{H}'_2
\end{aligned} \tag{B.8}$$

The separation of the perturbation $\widehat{H}'$ into $\widehat{H}'_1$ and $\widehat{H}'_2$ effectively separates the contribution from the radiation field to the Hamiltonian into components that are respectively linear or quadratic in $\vec{A}$.

The Schröedinger equation for the combined system of the charged particle and radiation field is solved via time-dependent perturbation theory. The probability for the system to undergo a transition from an initial state $|i\rangle$ to a final state $|f\rangle$, is expressed via the relation known as Fermi's golden rule:

$$W_{i\to f} = \frac{2\pi}{\hbar}\left|M_{if}\right|^2 \rho\left(E_f\right) \tag{B.9}$$

Here $\rho\left(E_f\right)$ is the density of states at the energy of the final state $|f\rangle$. The matrix element M_{if} is the expectation value of the time-dependent perturbation $\widehat{H}'$ to the time-independent free particle Hamiltonian, and can be written as:

$$M_{if} = \langle f|\,\widehat{H}'\,|i\rangle \tag{B.10}$$

B.1 Scattering of x-rays on free electrons

The current section deals with the scattering of a photon on a free electron initially at rest. It is required that the photon energies involved are much

smaller than the rest mass energy of the electron, $\hbar kc \ll m_e c^2$ where $\hbar kc$ is the photon energy, so that the system can be treated non-relativisticly. The electron states before and after the scattering event can be expressed as [32]:

$$|\psi_i\rangle = \frac{1}{\sqrt{V}} \tag{B.11}$$

$$|\psi_f\rangle = \frac{1}{\sqrt{V}} \exp\left[i\vec{k}_e \cdot \vec{r}\right] \tag{B.12}$$

The initial and final states of the combined system can be written as the product of the initial and final electron and photon states [32]:

$$|i\rangle = |\psi_i\rangle \left|..., n_{\vec{k},o}, ..., n_{\vec{k}',o'}, ...\right\rangle \tag{B.13}$$

$$|f\rangle = |\psi_f\rangle \left|..., n_{\vec{k},o} - 1, ..., n_{\vec{k}',o'} + 1, ...\right\rangle \tag{B.14}$$

For simplicity, this will be written:

$$|i\rangle = |\psi_i\rangle \left|n_{\vec{k},o}, n_{\vec{k}',o'}\right\rangle \tag{B.15}$$

$$|f\rangle = |\psi_f\rangle \left|n_{\vec{k},o} - 1, n_{\vec{k}',o'} + 1\right\rangle \tag{B.16}$$

In the final state the number of photons of wavevector $\vec{k}$ and polarization o has decreased by one whereas the number of photons of wavevector $\vec{k}'$ and polarization o' has increased by one. Because the scattering process involves both the annihilation of the incoming photon and the creation of the outgoing photon, the term of the perturbation $\widehat{H}'$ of Equation B.8 quadratic in $\vec{A}$ is used to calculate the matrix element of Equation B.10:

$$M_{if} = \langle f| \frac{e^2 \vec{A}^2}{2m_e} |i\rangle \tag{B.17}$$

For clarity, it might be convenient to write out the expression for the square of the vector potential:

$$\begin{aligned} \vec{A}^2 = & \sum_{\vec{k}^i, o^i} \vec{o}_{\vec{k}^i, o^i} \sqrt{\frac{\hbar}{2\epsilon_0 V \omega_{\vec{k}^i}}} \left(a_{\vec{k}^i, o^i} \exp\left[i\vec{k}^i \cdot \vec{r}\right] + a^\dagger_{\vec{k}^i, o^i} \exp\left[-i\vec{k}^i \cdot \vec{r}\right]\right) \\ \cdot & \sum_{\vec{k}^{ii}, o^{ii}} \vec{o}_{\vec{k}^i, o^{ii}} \sqrt{\frac{\hbar}{2\epsilon_0 V \omega_{\vec{k}^{ii}}}} \left(a_{\vec{k}^{ii}, o^{ii}} \exp\left[i\vec{k}^{ii} \cdot \vec{r}\right] + a^\dagger_{\vec{k}^{ii}, o^{ii}} \exp\left[-i\vec{k}^{ii} \cdot \vec{r}\right]\right) \end{aligned} \tag{B.18}$$

The first factor of $\vec{A}^2$ will serve to annihilate one photon in the $\vec{k}, o$ mode when $\vec{k}^i, o^i = \vec{k}, o$ and will create one photon in the $\vec{k}', o'$ mode when $\vec{k}^i, o^i =$

$\vec{k}', o'$. Similarly, the second factor will annihilate one photon in the $\vec{k}, o$ mode when $\vec{k}^{ii}, o^{ii} = \vec{k}, o$ and will create one photon in the $\vec{k}', o'$ mode when $\vec{k}^{ii}, o^{ii} = \vec{k}', o'$. The matrix element thus writes out as:

$$\begin{aligned} M_{if} &= 2\frac{e^2\hbar}{4m_e\epsilon_0 V}\frac{1}{\sqrt{\omega_{\vec{k}}\omega_{\vec{k}'}}}\sqrt{n_{\vec{k},o}\left(n_{\vec{k}',o'}+1\right)}\exp\left[i\left(\omega_{\vec{k}'}-\omega_{\vec{k}}\right)t\right] \\ &\cdot \quad \langle\psi_f|\exp\left[i\left(\vec{k}-\vec{k}'\right)\cdot\vec{r}\right]|\psi_i\rangle\left(\vec{o}_{\vec{k},o}\cdot\vec{o}_{\vec{k}',o'}\right) \end{aligned} \tag{B.19}$$

Here the factor involving the expectation value of $\exp\left[i\left(\vec{k}-\vec{k}'\right)\cdot\vec{r}\right]$ between the initial and final electron states represents the requirement for momentum conservation, written as a Krönecker delta $\delta_{\vec{k}-\vec{k}',\vec{k}_e}$:

$$\langle\psi_f|\exp\left[i\left(\vec{k}-\vec{k}'\right)\cdot\vec{r}\right]|\psi_i\rangle = \delta_{\vec{k}-\vec{k}',\vec{k}_e} \tag{B.20}$$

The absolute square of the matrix element thus can be written as:

$$|M_{if}|^2 = 4\left(\frac{e^2\hbar}{4m_e\epsilon_0 V}\right)^2\frac{1}{\omega_{\vec{k}}\omega_{\vec{k}'}}\left(n_{\vec{k},o}\left(n_{\vec{k}',o'}+1\right)\right)\left(\vec{o}_{\vec{k},o}\cdot\vec{o}_{\vec{k}',o'}\right)^2\delta_{\vec{k}-\vec{k}',\vec{k}_e} \tag{B.21}$$

Because the matrix element now is determined, the transition probability $W_{i\to f}$ of Equation B.9 can be calculated. The density of states for the current problem can according to [32] be expressed as a delta-function $\delta\left(E_e+\hbar\omega_{\vec{k}'}-\hbar\omega_{\vec{k}}\right)$, so that the transition probability is:

$$W_{i\to f} = \frac{2\pi}{\hbar}|M_{if}|^2\,\delta\left(E_e+\hbar\omega_{\vec{k}'}-\hbar\omega_{\vec{k}}\right) \tag{B.22}$$

Now, the only properties of this expression that pertain to the electron are the Krönecker delta of Equation B.20, and the delta-function just introduced. They represent respectively the requirements for momentum and energy conservation. The two factors together might be simplified:

$$\begin{aligned} \delta\left(E_e+\hbar\omega_{\vec{k}'}-\hbar\omega_{\vec{k}}\right)\delta_{\vec{k}-\vec{k}',\vec{k}_e} &= \delta\left(\hbar\left(\vec{k}-\vec{k}'\right)^2/2m_e+\hbar ck'-\hbar ck\right) \\ &\approx \delta\left(k'-k\right)/\hbar c \end{aligned} \tag{B.23}$$

Here the $\hbar kc \ll m_e c^2$ requirement has been invoked. It is seen that within this non-relativistic approximation the scattering is elastic. Thus the transition probability now reads:

$$W_{i\to f} = 4\frac{2\pi}{\hbar^2 c^3}\left(\frac{e^2\hbar}{4m_e\epsilon_0 V}\right)^2\frac{1}{kk'}\left(n_{\vec{k},o}\left(n_{\vec{k}',o'}+1\right)\right)\left(\vec{o}_{\vec{k},o}\cdot\vec{o}_{\vec{k}',o'}\right)^2\delta\left(k'-k\right) \tag{B.24}$$

The prefactor can be written more compactly by introducing the Thomson scattering length $r_0 = e^2/4\pi\epsilon_0 m_e c^2$, representing the distance for which the Coulomb energy between two electrons equals the electron rest mass energy, so that the expression for the transition probability becomes:

$$W_{i\to f} = \frac{8\pi^3 c}{V^2} r_0^2 \frac{1}{kk'} \left(n_{\vec{k},o}\left(n_{\vec{k}',o'}+1\right)\right)\left(\vec{o}_{\vec{k},o}\cdot\vec{o}_{\vec{k}',o'}\right)^2 \delta\left(k'-k\right) \tag{B.25}$$

From this expression the scattering cross section for photons incident on an electron initially at rest can be calculated by introducing the density of final photon states $Vd^3k'/\left(2\pi\right)^3$ and integrating over k'. Because the factor $d^3k' = k'^2 dk' \sin(\theta) d\theta d\phi = k'^2 dk' d\Omega$, this will effectively yield the probability for the interaction of the electron with the radiation field to annihilate an initial photon $\vec{k}, o$ while creating a scattered photon, of any k', detectable within the solid angle element $d\Omega$. From Equation B.25 this probability writes out as:

$$\begin{aligned}\int W_{i\to f}\frac{Vd^3k'}{\left(2\pi\right)^3} &= \frac{c}{V} r_0^2 \left(n_{\vec{k},o}\left(n_{\vec{k}',o'}+1\right)\right)\left(\vec{o}_{\vec{k},o}\cdot\vec{o}_{\vec{k}',o'}\right)^2 \\ &\cdot \int \frac{1}{kk'}\delta\left(k'-k\right)k'^2 dk' d\Omega \\ &= \frac{c}{V} r_0^2 \left(n_{\vec{k},o}\left(n_{\vec{k}',o'}+1\right)\right)\left(\vec{o}_{\vec{k},o}\cdot\vec{o}_{\vec{k}',o'}\right)^2 d\Omega \end{aligned} \tag{B.26}$$

Now, the differential scattering cross section should reflect the probability for the interaction of the electron with one single photon to produce a scattered photon emitted into $d\Omega$. The expression of Equation B.26 therefore must be divided by the factor $n_{\vec{k},o}c/V$, i.e. the incident photon flux, in order to yield the following expression for $\delta\sigma$:

$$d\sigma = \frac{V}{n_{\vec{k},o}c}\int W_{i\to f}\frac{Vd^3k'}{\left(2\pi\right)^3} = r_0^2\left(n_{\vec{k}',o'}+1\right)\left(\vec{o}_{\vec{k},o}\cdot\vec{o}_{\vec{k}',o'}\right)^2 d\Omega \tag{B.27}$$

According to [32], the parameter $n_{\vec{k}',o'}$ is commonly set to zero, thereby neglecting the effects of photons already present in the $\vec{k}', o'$ mode. The differential scattering cross section is then found by dividing both sides of Equation B.27 by the solid angle element $d\Omega$. The resulting quantity is known as the differential Thomson scattering cross section:

$$\frac{d\sigma}{d\Omega} = r_0^2\left(\vec{o}_{\vec{k},o}\cdot\vec{o}_{\vec{k}',o'}\right)^2 \tag{B.28}$$

Now the scalar product between the polarizations of the initial and final photons must be determined. The two independent polarizations possible for the initial photon can be taken either parallel with or perpendicular to

the plane containing $\vec{k}$ and $\vec{k}'$, i.e. as either $\vec{o}_{\parallel}$ or $\vec{o}_{\perp}$. The same choice, i.e. of $\vec{o}'_{\parallel}$ or $\vec{o}'_{\perp}$, can be made for the two independent polarizations of the scattered photon, but with the in-plane polarization $\vec{o}'_{\parallel}$ making an angle θ with the in-plane polarization of the initial photon. The scalar product $\vec{o}_{\parallel} \cdot \vec{o}'_{\parallel}$ of the in-plane initial polarization with the in-plane final polarization is equal to $\cos\theta$, whereas the two scalar products $\vec{o}_{\parallel} \cdot \vec{o}'_{\perp}$ and $\vec{o}_{\perp} \cdot \vec{o}'_{\parallel}$ both equal zero. However, the scalar product $\vec{o}_{\perp} \cdot \vec{o}'_{\perp}$ of the initial and final perpendicular polarizations is equal to one. Thus, for an incoming photon that with certainty was polarized in the scattering plane, the differential scattering cross section is $d\sigma/d\Omega_{\parallel}$, whereas for an initial photon polarized perpendicular to the plane, the differential scattering cross section is $d\sigma/d\Omega_{\perp}$:

$$\frac{d\sigma}{d\Omega}_{\parallel} = r_0^2 \cos^2\theta \tag{B.29}$$

$$\frac{d\sigma}{d\Omega}_{\perp} = r_0^2 \tag{B.30}$$

Now, for an unpolarized source the two polarizations of the initial photon are equally likely. The unpolarized differential cross section is therefore the weighted sum of the two polarized contributions:

$$\frac{d\sigma}{d\Omega} = \frac{1}{2} r_0^2 \left(1 + \cos^2\theta\right) \tag{B.31}$$

Finally, the unpolarized total Thomson cross section is found by multiplying Equation B.31 by the solid angle element $d\Omega$ and integrating:

$$\begin{aligned} \sigma &= \int \frac{d\sigma}{d\Omega} d\Omega \\ &= \frac{1}{2} r_0^2 \int_0^{2\pi} d\phi \int_0^{\pi} \left(1 + \cos^2\theta\right) \sin\theta d\theta \\ &= \frac{1}{2} r_0^2 2\pi \frac{8}{3} \\ &= \frac{8\pi}{3} r_0^2 \end{aligned} \tag{B.32}$$

With the numerical value of $r_0 = 2.818$ fm inserted, the Thomson cross section for photons scattering off an electron initially at rest is $\sigma = 665$ mb.

Appendix C

Yorick image extraction and format conversion with Image Magick

The current appendix concerns Yorick and later on Image Magick. Yorick is a C-based, freely distributed analysis software developed at MIT which is used for image processing by the GIST staff and students at the PAL synchrotron. However, the binary file formats used to store scattering images are Yorick specific, and thus data are not immediately accessible to users unfamiliar with the Yorick language. The current appendix is mainly intended as a reference for other NTNU students or researchers, who in the future might wish to tackle GIST based Yorick procedures and thus obtain their scattering data.

To start Yorick, open a Unix/Linux shell and write:

```
rlwrap yorick
```

Rlwrap is the so-called readline feature command line wrapper in Unix/Linux, which for instance allows arrow-based history scrolling, a feature not included in Yorick. Now, to compile a single scattering image from a series of recorded .imm files, a file called gathermacro.i must be executed. This file is a simple, GIST developed program which sums up data .imm files and subtracts darks. This and other Yorick files should be available from either the COMPLEX group of from GIST. To run gathermacro.i, write:

```
include, "gathermacro.i"
```

It is necessary to edit gathermacro.i in a text editor like Emacs, to tell the program how many images and darks it should compile into one image. Now, gathermacro.i on its own includes two other files, namely collectimm.i and streamfunction.i, which are also GIST developed. It is the collectimm.i file that controls image processing. In order for collectimm.i to function

properly, yorick must be wrapped in the folder the .imm files are located in. If the .imm files are called for instance image_00001.imm, image_00002.imm, etc, it is essential that the folder they are stored in is called image. This is due to the manner in which collectimm.i deals with filenames.

After gathermacro.i has run it's course, it will save the resulting compiled and background subtracted scattering image as a .dif binary file. To open a .dif file file.dif in Yorick, write:

b=openb("file.dif"); get_vars(b);

To read the data from this file into a Yorick array variable, write:

data_raw=b.Fint; data=int(data_raw);

The data can now be either further processed in Yorick, or written to a more convenient format accessible by other software, like for instance fit2d. First make sure that there are no negative pixel points in the data array:

neg_data=where(data¡0.0); data(neg_data)=0.0;

Now the data array can be converted to a very convenient file format, commonly known as pnm, although this is really a group of formats. Yorick knows this, so make use of the pnm_write() function:

picture=pnm_write(data,"picturefile",bits=16,noscale=1);

Now, the data is stored in a pnm file called picturefile. So far, so good. This pnm file can easily be further treated with the use of another freeware called Image Magick. Say format conversion to .tif is desirable. This is easily accomplished. In a Unix/Linux shell, simply write:

convert picturefile picturefile.tif

Now this .tif file can for instance, be imported into fit2d and analyzed.

There are many more areas in which Image Magick is immensely useful. The optical image series of this project for instance, with their at times hundreds of consecutive captured frames, needed to be individually cropped and resized for film making as well as for inclusion in this report. Image Magick is a free software distribution for both Unix and Windows platforms, run from the command line, that is tailored for batch image processing. As an example, the following code will produce a series of 400 pixels wide and 800 pixels high images cropped so that their upper left corners coincide with the pixel point (10,300) of all the original .jpg image files in the current file folder:

mogrify -crop 400x800+10+300 *.jpg

Another useful example demonstrates how individual .bmp image files can be adjoined to form a single .png image called combined:

```
montage -adjoin -geometry 200x200+0+0 -tile 3x2 *.bmp
combined.png
```

Here the -geometry option sets the size of each contributing .bmp image to 200x200 pixels, and the frame around each image to zero pixels, effectively pasting the images edge to edge. The -tile options specifies that combined.png should be three images wide and two images high. If there are more than $3 \cdot 2 = 6$ .bmp images, several sequentially numbered combined images will be created automatically. The use of Image Magick in handling graphical files is highly recommended.

Bibliography

[1] T. Nakken Aalerud. Synchrotron x-ray scattering studies of water intercalation in synthetic nickel-fluorohectorite. Master's thesis, Norwegian University of Science and Technology, 2001.

[2] J. Als-Nielsen and D. McMorrow. *Elements of modern x-ray physics*. Jon Wiley and Sons, 2001.

[3] F. Bergaya, B.K.G. Theng, and G. Lagaly, editors. *Handbook of clay science*. Developments in clay science 1. Elsevier, 2006.

[4] G.I. Blake, T. Mullin, and S.J. Tavener. The freedericksz transition as a bifurcation problem. *Dynamics and Stability of Systems*, 14(3):299–331, 1999.

[5] R.A. Bone, J.T. Landrum, and A. Cains. Optical denisty spectra of the macular pigment in vivo and in vitro. *Vision Res.*, 32(1):105–110, 1992.

[6] I.N. Bronstein, K.A. Semendjajew, G. Musiol, and H. Mühlig. *Taschenbuch der Mathematik*. Verlag Harri Deutsch, 2005.

[7] P.J. Collings. *Liquid Crystals - Nature's Delicate Phase of Matter*. Princeton University Press, 2002.

[8] J.C. Crocker and D.G. Grier. When like charges attract: the effects of geometrical confinement on long-range colloidal interactions. *Phys. Rev. Lett.*, 77:1897–1900, 1996.

[9] G.J. da Silva, J.O. Fossum, E. DiMasi, K.J. Måløy, and S.B. Lutnæs. Synchrotron x-ray scattering studies of water intercalation in a layered synthetic silicate. *Phys. Rev. E*, 66:011303, 2002.

[10] E.N. de Azevedo, M. Engelsberg, J.O. Fossum, and R.E. de Souza. Anisotropic water diffusion in nematic self-assemblies of clay nanoplatelets suspended in water. *Langmuir*, 23:5100–5105, 2007.

[11] B.V. Derjaguin and L. Landau. *Acta Physicochim.*, 14:633–662, 1941.

[12] E. diMasi, J.O. Fossum, T. Gog, and C. Venkataraman. Orientational order in gravity dispersed clay colloids: A synchrotron x-ray scattering study of Na fluorohectorite suspensions. *Phys. Rev. E*, 64:061704, 2001.

[13] W.A. Ducker and R.M. Pashley. Forces between mica surfaces in the presence of rod-shapes divalent counterions. *Langmuir*, 8:109–112, 1992.

[14] A.S. Dukhin, S.S. Dukhin, and P.J. Goetz. Gravity as a factor of aggregative stability and coagulation. *Advances in Colloid and Interface Science*, 134-135:35–71, 2007.

[15] R. Eppenga and D. Frenkel. Monte carlo study of the isotropic and nematic phases of infinitely thin hard platelets. *Mol. Phys.*, 52(6):1303–1334, 1984.

[16] D.d.M. Fonseca. *Phase separation and orientational ordering of synthetic Na-fluorohectorite clay particles in saline aqueous suspensions.* PhD thesis, Norwegian University of Science and Technology, 2008.

[17] D.M. Fonseca, Y. Méheust, J.O. Fossum, K.D. Knudsen, K.J. Måløy, and K.P.S. Parmar. Phase behaviour of platelet-shaped nanosilicate colloids in saline solutions - a small-angle x-ray scattering study. *J. Appl. Cryst.*, 40:292–296, 2007.

[18] D.M. Fonseca, Y. Méheust, J.O. Fossum, K.D. Knudsen, and K.P.S. Parmar. The phase diagram of polydisperse na-fluorohectorite-water suspensions: a synchrotron saxs study. Article not yet submitted.

[19] J.O. Fossum. Lecture notes for ntnu subject: Light-, neutron and x-ray scattering. From class thought in the Fall semester of 2007.

[20] J.O. Fossum, E. Gudding, D.d.M. Fonseca, Y. Meheust, E. DiMasi, T. Gog, and C. Venkataraman. Observations of orientational ordering in aqueous suspensions of a nano-layered silicate. *Energy*, 30:873–883, 2005.

[21] F.C. Frank. I. liquid crystals. on the theory of liquid crystals. *Discuss. Faraday Soc.*, 25:19–28, 1958.

[22] B.J. Frisken and P. Palffy-Muhoray. Freedericksz transitions in nematic liquid crystals: the effects of an in-plane electric field. *Phys. Rev. A*, 40(10):6099–6102, 1989.

[23] J.C.P. Gabriel and P. Davidson. Mineral liquid crystals from self-assembly of anisotropic nanosystems. *Top. Curr. Chem.*, 226:119–172, 2003.

[24] J.C.P. Gabriel, C. Sanchez, and P. Davidson. Observation of nematic liquid-crystal textures in aqueous gels of smectite clays. *J. Phys. Chem.*, 100:11139–11143, 1996.

[25] I. Gallily and A.-H. Cohen. On the stochastic nature of the motion of nonspherical aerosol particles. 1. The aerodynamic radius concept. *Jounral of Colloid and Interface Science*, 56(3), 1976.

[26] D.J. Griffiths. *Introduction to Electrodynamics*. Prentice Hall International, 1999.

[27] A. Guinier and G. Fournet. *Small-angle scattering of x-rays*. Structure of matter series. Wiley, 1955.

[28] N. Güven. *Hydrous Phyllosilicates (exclusive of micas)*. Mineralogical Society of America, 1998.

[29] M.M. Hanczyc, S.M. Fujikawa, and J.W. Szostak. Experimental models of primitive cellular compartments: Encapsulation, growth, and division. *Science*, 302:618–621, 2003.

[30] H. Hemmen. Experimental studies of nanostructured clay gels. Master's thesis, Norwegian University of Science and Technology, 2008.

[31] H. Hemmen, N.I. Ringdal, E.N. de Azevedo, E.L. Hansen, J.O. Fossum, M. Engelsberg, Y. Mehéust, and K.D. Knudsen. Experimental studies of the isotropic-nematic interface in suspensions of na-fluorohectorite synthetic clay. Submitted to Langmuir.

[32] P.C. Hemmer. *Kvantemekanikk*. Tapir Akademisk forlag, 2000.

[33] J. Israelachvili. *Intermolecular and surface forces*. Academic Press, 1992.

[34] J.N. Israelachvili and R.M. Pashley. Molecular layering of water at surfaces and origin of repulsive hydration forces. *Nature*, 306:249–250, 1983.

[35] R. Kjellander, S. Marcelja, R.M. Pashley, and J.P. Quirk. *J. Phys. Chem.*, 92:6489–6492, 1988.

[36] M. Kleman and O.D. Lavrentovich. *Soft matter physics - and introduction*. Partically ordered systems. Springer, 2003.

[37] K.D. Knudsen, J.O. Fossum, G. Helgesen, and V. Bergaplass. Pore characteristics and water absorption in a synthetic smectite clay. *J. Appl. Cryst.*, 36:587–591, 2003.

[38] I. Langmuir. The role of attractive and repulsive forces in the formation of tactoids, thixotropic gels, protein crystals and coacervates. *Journal of Chemical Physics*, 6:873–896, 1938.

[39] B.J. Lemaire, P. Panine, J.C.P. Gabriel, and P. Davidson. The measurement by SAXS of the nematic order parameter of laponite gels. *Europhys. Lett.*, 59(1):55–61, 2002.

[40] J. Lilley. *Nuclear Physics Principles and Applications*. The Manchester Physics Series. John Wiley and Sons, 2001.

[41] W. Maier and A. Saupe. *Naturforsch. A*, 13:564–566, 1958.

[42] W. Maier and A. Saupe. *Naturforsch. A*, 14:882–889, 1959.

[43] J. Marra. *J. Phys. Chem.*, 90:2145–2150, 1986.

[44] C.E. Marshall. Studies in the degree of dispersion of the clays. I. Notes on the technique and accuracy of mechanical analysis using the centrifuge. *Journal of the Society of Chemical Industry*, 50:440–450, 1931.

[45] M.B. McBride. A critique of diffuse double layer models applied to colloid and surface chemistry. *Clays and Clay Minerals*, 45(4):598–608, 1997.

[46] M.B. McBride and P. Baveye. Diffuse double-layer models, long-range forces, and ordering in clay colloids. *Soil Sci. Soc. Am. J.*, 66:1207–1217, 2002.

[47] A. Meunier. *Clays*. Springer, 2005.

[48] Y. Méheust, K.D. Knudsen, and J.O. Fossum. Inferring orientation distributions in anisotropic powders of nano-layered crystallites from a single two-dimensional waxs image. *J. Appl. Cryst.*, 39:661–670, 2006.

[49] L.J. Michot, I. Bihannic, S. Maddi, C. Baravian, P. Levitz, and P. Davidson. Sol/gel and isotropic/nematic transitions in aqueous suspensions of natural nontronite clay. Influence of particle anisotropic. 1. Features of the I/N transition. *Langmuir*, 24:3127–3139, 2008.

[50] N/A. Illustration of splay, twist and bend distortions from the liquid crystals and photonics group at the University of Gent. http://trappist.elis.ugent.be/ELISgroups/lcd/lc/lc2.html.

[51] N/A. Michel lévy color chart polarized light conoscopic determination. http://www.zeiss.de/C1256D18002CC306/0/F2BA0A81B5929487C1256D59003351AA/$file/46-0014_e.pdf/.

[52] N/A. The NIST reference on constants, units and uncertainty. http://physics.nist.gov/cuu/Constants/index.html.

[53] A.V. Nguyen and H.J. Schulze, editors. *Colloidal science of flotation*, volume 18 of *Surfactant science series*. Marcel Dekker Inc., 2004.

[54] I.E. Odom. Smectite clay minerals: properties and uses. *Philosophical transactions of the Royal Society of London A*, 311:391–409, 1984.

[55] L. Onsager. The effects of shape on the interaction of colloidal particles. *Ann. N.Y. Acad. Sci.*, 51:627–659, 1949.

[56] C.W. Oseen. The theory of liquid crystals. *Trans. Faraday Soc.*, 140:883–899, 1933.

[57] P. Oswald and P. Pieranski. *Nematic and cholesteric liquid crystals - concepts and physical properties illustrated by experiments*. The liquid crystals book series. CRC Press, Taylor and Francis Group, 2005.

[58] V.A. Parsegian. *Van der Waals forces: A handbook for biologists, chemists, engineers, and physicists*. Cambridge University Press, 2006.

[59] N.I. Ringdal. Experimental studies of self-oranized liquid crystalline phases from clay nanoplatelets in water: Birefringence and structure. Master's thesis, Norwegian University of Science and Technology, 2008.

[60] F. Salles, O. Bildstein, J.M. Douillard, M. Jullien, and H. Van Damme. Determination of the driving force for the hydration of the swelling clays from computation of the hydration energy of the interlayer cations and the clay layer. *J. Phys. Chem. C*, 111:13170–13176, 2007.

[61] E.J. Samuelsen. *Materials Physics - structure, diffraction, imaging and spectroscopy*. NTNU-Trykk, 2006.

[62] T. Scharf. *Polarized light in liquid crystals and polymers*. John Wiley and Sons, 2007.

[63] N.T. Skipper, P.A. Lock, J.O. Titiloye, J. Swenson, Z.A. Mirza, W.S. Howells, and F. Fernadez-Alonso. The structure and dynamics of 2-dimensional fluids in swelling clays. *Chemical geology*, 230:182–196, 2006.

[64] P.G. Slade and W.P. Gates. The swelling of HDTMA smectites as influenced by their preparation and layer charges. *Applied clay science*, 25:92–101, 2004.

[65] M. Smalley. *Clay swelling and Colloid Stability*. Taylor and Francis Group, 2006.

[66] I. Sogami and N. Ise. On the electrostatic interaction in macroionic solutions. *J. Chem. Phys.*, 81:6320–6332, 1984.

[67] K. Sokalski and T.W. Ruijgrok. Elastic constants for liquid crystals of disc-like molecules. *Physica A*, 113:126–132, 1982.

[68] H. Stark. Physics of inhomogeneous nematic liquid crystals: Colloidal dispersions and multiple scattering of light.

[69] G. Strobl. *Condensed matter physics - crystals, liquids, liquid crystals, and polymers*. Springer, 2004.

[70] T. Svedberg and J.B. Nichols. Determination of size and distribution of size of particle by centrifugal methods. *J. Am. Chem. Soc.*, 45(12):2910–2917, 1923.

[71] D. van der Beek, P.B. Radstake, A.V. Petukhov, and H.N.W. Lekkerkerker. Fast formation of opal-like columnar colloidal crystals. *Langmuir*, 23(23):11343–11346, 2007.

[72] D. van der Beek, H. Reich, P. van der Schoot, M. Dijkstra, T. Schilling, R. Vink, M. Schmidt, R. van Roij, and H. Lekkerkerker. Isotropic-nematic interface and wetting in suspensions of colloidal platelets. *Phys. Rev. Lett.*, 97:087801–1–087801–4, 2006.

[73] D. van der Beek, T. Schilling, and H.N.W. Lekkerkerker. Gravity induced liquid crystal phase transitions of colloidal platelets. *J. Chem. Phys.*, 121:5423–5426, 2004.

[74] F.M. van der Kooij and H.N.W. Lekkerkerker. Formation of nematic liquid crystals in suspensions of hard colloidal platelets. *J. Phys. Chem. B*, 102:7829–7832, 1998.

[75] F.M. van der Kooij and H.N.W. Lekkerkerker. Liquid-crystal phase transitions in suspensions of plate-like particles. *Philosophical Transactions: Mathematical, physical and engineering sciences*, 359:985–995, 2001.

[76] J.A.C. Veerman and D. Frenkel. Phase behaviour of disklike hard-core mesogens. *Phys. Rev. A*, 45(8):5632–5648, 1992.

[77] B. Velde. *Introduction to clay minerals - chemistry, origins, uses and environmental significance*. Chapman and Hall, 1992.

[78] B. Velde, editor. *Origin and Mineralogy of clays*. Clays and the environment. Springer, 1995.

[79] E.J.W. Verwey and J.T.G. Overbeek. *Theory of stability of lyophobic colloids*. Elsevier, 1948.

[80] T.W. Warmerdam, D. Frenkel, and R.J.I Zijlstra. Measurements of the ratio of the frank constants for splay and bend in nematics consisiting of disc-like molecules 2,3,6,7,10,11-hexakis(p-alkoxybenzoyloxy)triphenylenes. *Liquid Crystals*, 3(3):369–380, 1988.

[81] W.R. Whalley and C.E. Mullins. Oriented and random sedimentation of plate-like clay particles in high centrifugal fields. *Journal of Soil Science*, 43:531–540, 1992.

[82] H. Wiedemann. *Synchrotron Radiation*. Springer, 2003.

[83] H. Zocher. The effect of a magnetic field on the nematic state. *Trans. Faraday Soc.*, 29:945–957, 1933.